ISSN 1880-8468

Technical Report of
International Development Engineering
国際開発工学報告

TRIDE-2010-03 February 16, 2010

Abstracts of Master Theses
Presented in February 2010

Department of International Development Engineering,
Graduate School of Science and Engineering,
Tokyo Institute of Technology
http://www.ide.titech.ac.jp/TR

Preface

Master theses of Department of International Development Engineering, Tokyo Institute of Technology were presented successfully on August 3, 2009 and February 16, 2010. This technical report consists of the abstracts of those theses.

Technical Report of International Development Engineering
TRIDE-2010-03

Table of Contents

CORROSION BEHAVIOUR OF STAINLESS STEEL IN CONCRETE EXPOSED TO CARBONATION

Student Number: 07M51418 Name: George William C. HONG Supervisor: Nobuaki OTSUKI

The study investigated the corrosion behaviour of stainless steel in concrete exposed to carbonation. Three types of steels, SUS304 (18% Cr), SUS410L (12% Cr) and ordinary carbon steel SD295A, were cast in several OPC-concrete scenarios. The following were observed: **(1)** Both stainless steels were unaffected by carbonation in concrete with proper cover even with high water/cement ratio (0.7w/c) and high temperature exposure (40ºC). **(2)** Galvanic effect was observed and enhanced by carbonation though was not a great corrosion threat for steels; while early ingress of carbonation (due to thin cover) served as corrosion threat for the economical SUS410L stainless steel. **(3)** Carbonation enhanced the corrosive effects of chloride on SUS410L and SD295A ordinary steel; while both stainless steels remained passive at pH 8 solution. Overall, carbonation was not a great threat for stainless steels; however, some factors enhanced its effects. The new economical stainless steels (ex. SUS410L) with lowered chromium content merit caution when used in carbonated environments, especially in thin cover scenarios.

1 Introduction

1.1 Stainless Steels

Stainless steels have been used as concrete reinforcement for structures that need to withstand the harshest environments; therein, serving as a solution to the engineering problem of corrosion. The high cost of stainless steels, however, has driven industry and academe to further develop lower costing steels to better its economic viability and promote innovative applications. These cheaper stainless steels produced have lowered chromium and nickel contents which make them more susceptible to corrosion **[1]**.

1.2 Carbonation in Concrete

While corrosion studies on stainless steels have focused on the harsher environments, the weaker causes of corrosion, such as carbonation, have yet to be extensively explored. Carbonation in concrete relies on the mechanism of lowering the pH of concrete and therein destroying the protective passivating film formed on steels **[2]**. Stainless steels, at a glimpse, may seem to be unaffected by a weak carbonation effect. However, with the new innovative steels with lowered chromium and nickel content, greater consideration must be made for the safe and appropriate usage in carbonated environments.

1.3 Research Objectives

The research goal was to gain better understanding of the corrosion behaviour of stainless steel in concrete exposed to carbonation and ultimately contribute to the pursuit of better designs and wider applications for stainless steel as a sustainable material for society. The specific objectives were: **(1)** To investigate the general corrosion behaviour of stainless steel in concrete exposed to carbonation; considering (a) water/cement ratio, (b) carbonation exposure, (c) temperature variations and (d) types of steel. **(2)** To investigate the macrocell and microcell corrosion induced by (a) galvanic effect, (b) crack defect and (c) thin cover. **(3)** To investigate the effects of (a) chloride in concrete and (b) pH variation in solutions on the corrosion behaviour of stainless steel. The research may provide information for material selection and investigative works of structures, and support the efforts in producing better performing steels that accommodate economy and serviceability for society.

Table 1: Steel Specifications

Steel 13mm Ø	Cr (%)	Fe (%)	Ni (%)	C (%)	Si (%)	Mn (%)	P (%)	S (%)	Yield N/mm^2
SUS 304	18.34	71.06	8.13	0.05	0.37	1.50	0.31	0.24	295
SUS 410L	12.57	86.34	0.20	.005	0.32	0.32	0.22	0.03	295
SD 295A	-	98.27	-	0.18	0.12	0.65	0.32	0.46	295

2 Experimental Procedures

2.1 Materials

Three types of steels were investigated: (1) SUS304 Stainless steel (18% Cr); (2) SUS410L Stainless Steel (12% Cr); (3) SD295A Ordinary Carbon Steel. The undivided steel bars were corrugated type, 13mm diameter and 8cm long. For divided steel bars, 1cm length bars were used. The steels' chemical compositions are shown in Table 1. OPC cement was used with natural river sand and coarse aggregates (13mm maximum size) to make concrete specimens.

2.2 Investigation Scenarios

The specimens were designed to address each objective of the study. The steel specimens were casted in OPC concrete and were exposed to 20ºC with 5% - 10% CO_2 at 60-70% RH for carbonated exposures and to 20ºC at 50-80% RH with negligible CO_2 levels for non-carbonated exposures. The specimens' details are shown in Table 2.

2.3 Corrosion Monitoring

The general or microcell corrosion of steels were assessed using three electrochemical techniques; Corrosion Potentials, Corrosion Current through Polarization Resistance, and Passivity Grades through Anodic Polarization. Macrocell corrosion was monitored using the divided steel bars concept developed by Otsuki and Miyazato et al. (2001) **[3]**. Visual confirmation was also performed while phenolphthalein test was used to monitor carbonation depth.

Corrosion Potentials: The corrosion potentials indicate the probability of corrosion of steel. This was measured using the corrosion monitoring instrument CT-7, manufactured by Riken Denshi Co., Ltd., using an Ag/AgCl reference electrode ($E_{Ag/AgCl} = E_{SCE} + 0.006V$) **[4]**. Potentials ranging more than -250 mV are considered to have 90% probability of no corrosion. Potentials between -250 mV to -400 mV are said to have some probable degree of corrosion, though quite uncertain. Potentials less than -400 mV are considered to have 90% probability of active corrosion for Ag/AgCl reference electrode for the study (ASTM C876-6).

Corrosion Current: The polarization resistance of steels was measured using the corrosion monitoring instrument CT-7, manufactured by Riken Denshi Co., Ltd., using an Ag/AgCl reference electrode **[4]**. A voltage of 50 mV with amplitude ranging from 0.05 Hz to 5000 Hz was applied. Equation 1 shows the function of corrosion current. For the study, a constant of K = 0.0209 V was assumed for both carbon steel and stainless steels.

$$I_{micro} = \frac{K}{R_p \times S} \qquad \textbf{Equation 1}$$

where: I_{micro} : microcell corrosion current density (A/cm^2),

K : Stearn-Geary constant = 0.0209 (V),

R_p : polarization resistance (Ω), S : surface area of component (cm^2).

Anodic Polarization and Passivity Grades: For the study, the passivity grading method derived from the anodic curves as described by Otsuki et al. (1992) **[5]** was applied. This was done using a potentiostat (HZ-3000 by Hokuto Denko) which shifts the steel potential from its natural value to breakdown potential or a value of -1V with a scan rate of 1mV/s. A reference electrode of Ag/AgCl and counter electrode of stainless steel was used. The passivity grading system considers the anodic currents' range at the 0.2V to 0.6V potential, where grade 5 passivity indicates good passivity protection and grade 0 passivity indicates no passivity.

Macrocell Corrosion Current: The divided steel bars concept developed by Otsuki and Miyazato et al. (2001) was used to assess the macrocell corrosion of the steel bars **[3]**. The corrosion currents flowing in and out of the bars were measured using zero-resistance ammeters; the set-up is shown in Figure 3.

Carbonation Depth: The carbonation monitoring was performed using phenolphthalein solution test; 1g phenolphthalein in 90ml ethyl alcohol and 10ml H_20 solution. This test indicated the area where pH of concrete had values above pH 9 **[6]**.

Table 2: Specimen Specifications and Exposure

Specimen	Specifications	Exposure (Carbonated and Non-Carbonated)
W/C ratio & Temp	(0.3, 0.5, 0.7 w/c); (15mm cover)	(20ºC for 260 days) (30 & 40ºC for 5 hours after 260 days in 20ºC)
Galvanic	(0.5 & 0.7 w/c); (15mm cover)	20ºC for 260 days
Crack Defect	(1mm crack); (0.5 w/c); (15mm cover)	(20ºC for 100 days) (40ºC for 5 hours after 100 days in 20ºC)
Thin Cover and Chloride	(0.7 w/c mortar); (3mm cover) (0,3,6 kg/m^3 Cl^-)	20ºC for 60 days
pH solutions	(Bare steel) (pH 3: H_2SO_4); (pH 6: Na_2SO_4); (pH 8 & 12: $CaOH_2$)	20ºC for 14 days

3 Results and Discussions

3.1 General Corrosion

Water/Cement Ratio Effect: The steels were casted in three water cement ratios, 0.3, 0.5, and 0.7 w/c, and exposed in carbonation for 260 days. Only the 0.7 w/c specimen carbonation depths reached the steel bars with an average of 27mm carbonation depth. Results showed that higher water cement ratio allowed faster carbonation ingress, therein promoting corrosion.

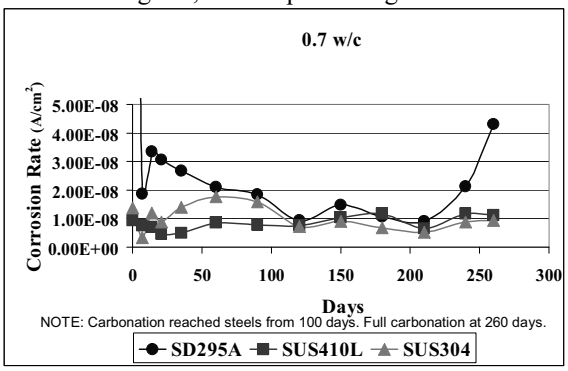

Figure 1: Corrosion Currents of Carbonated Specimens

Carbonation Effect: The effect of carbonation was observed for the SD295A steel bars with a drop in potential and increase in corrosion currents as seen in Figure 1. Both stainless steels were unaffected by carbonation and remained at high potentials and low corrosion currents. With proper concrete cover, both stainless steels were resistant to carbonation.

Temperature Effect: The 0.7 w/c specimens were exposed to higher temperatures (30ºC and 40ºC) for 5 hours at each temperature and monitored accordingly. The potentials are shown in Figure 2 for varying temperatures. The higher temperature caused a

potential drop for all the steels. However, only SD295A turned to active corroding state, while both stainless steels remained at high potentials. The corrosion currents results also showed an increase in SD295A corrosion currents ($4.5x10^{-8}$ A/cm^2) while both stainless steels remained low in currents (about $1x10^{-8}$ A/cm^2). Temperature increase was seen to enhance the effects of carbonation, although stainless steels remained passive.

Steel Types: Although both stainless steels remained passive in carbonation exposure, SUS304 was observed to have higher potentials and lower corrosion currents compared to SUS410L. Both stainless steels were superior in corrosion resistance compared to SD295A carbon steel.

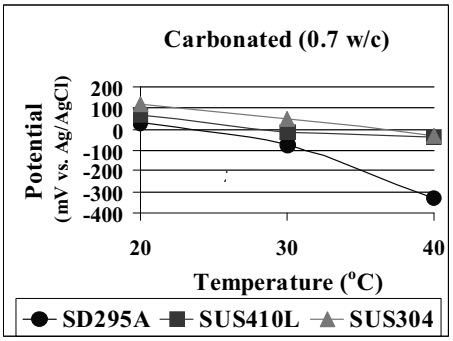

Figure 2: Corrosion Potentials of Carbonated Specimens in Varying Temperatures

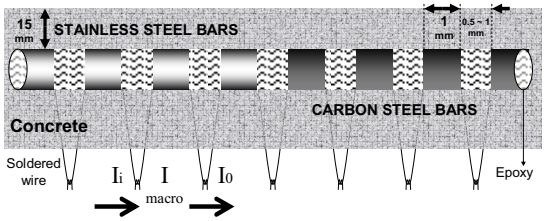

Figure 3: Macrocell Galvanic Corrosion Divided Steel Bars Set-up

3.2 Macrocell Corrosion

Galvanic Effect: The galvanic effect of steels occurs when dissimilar metals with different potentials are connected. In this case, the stainless steel bars were connected to the carbon steel bars using the divided steel bar concept shown in Figure 3. Upon carbonation, the ordinary carbon steel connected to the stainless steels turned anodic while the stainless steels turned cathodic, as shown in Figure 4. This showed that galvanic effect occurred and was enhanced by carbonation. However, the macrocell currents (low values of ~x10^{-9}A/cm^2) were smaller than the microcell currents (high values of ~x10^{-9} to ~x10^{-8}A/cm^2) for the same steel bars. This indicated that the galvanic effect was not a great corrosion threat for the steels.

Cracks Effect: The cracked region allowed faster carbonation ingress compared to the uncracked regions. The cracked regions showed higher macrocell corrosion than microcell corrosion. The SD295A turned into active corrosion state and increased in currents while the stainless steels remained passive, although increased slightly in currents, as shown in Figure 5. Passivity grades of stainless steels remained high while visual confirmation showed no signs of corrosion for both stainless steels.

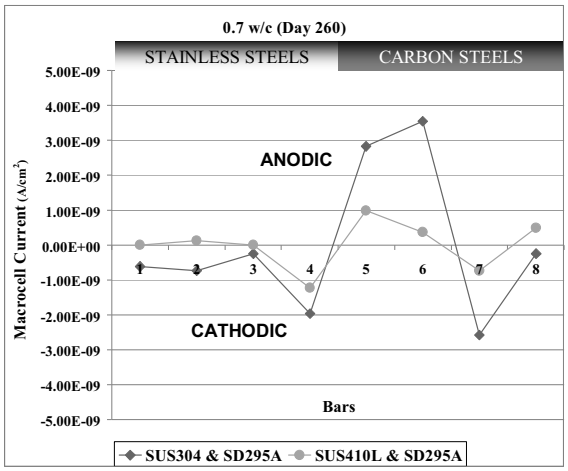

Figure 4: Macrocell Corrosion Currents for Galvanic Effect (Carbonated)

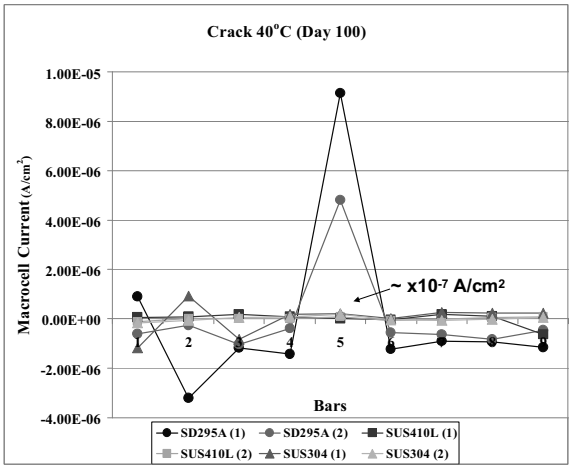

(uncracked regions = ~x10^{-9} to ~x10^{-8} A/cm^2)

Figure 5: Macrocell Corrosion Currents for Crack (Carbonated)

Thin Cover Effect: Mortar concrete was used for the thin cover (3mm) specimens with undivided steel bars. The thin cover allowed early ingress of carbonation, reaching a 12mm carbonation depth in 60 days exposure period. The results showed a drop in potential for SD295A and SUS410L (-250 to -300 mV range) showing considerable probability of corrosion. Corrosion currents increased for both steels, although SUS410L ($2x10^{-8}$ A/cm^2) remained relatively lower than SD295A ($1x10^{-7}$ A/cm^2). The passivity grading of SUS410L dropped to 2 while SD295A dropped to 1 as shown in Figure 6. Visual confirmation showed that general corrosion occurred for SD295A and a pitting corrosion tendency was seen for SUS410L. A study done by Imperial College Of Science, Technology And Medicine (2002, February 14) indicated that stainless steels corrode through pitting due to random low-chromium regions in the metal **[7]**. Carbonation may have exploited this phenomenon and affected SUS410L in thin cover scenario.

3.3 Chloride and pH Solutions

Chloride Effect: Chloride (NaCl) of 0, 3, 6 kg/m^3 of mortar was mixed in concrete (thin cover 3mm) using undivided steel bars. Carbonation was seen to enhance the effects of chloride additions such that only the carbonated specimens showed signs of corrosion in the steels. SUS410L was affected by chloride and carbonation, where potentials dropped to active regions, corrosion currents increased and passivity grade lowered at 3 and 6 kg/m^3 Cl^-. SUS304 remained passive in all chloride and carbonation scenarios.

pH Effect: Bare steels were submerged in pH solutions for 14 days. Different pH level solutions were achieved by mixing H_2O with H_2SO_4 for pH 3, Na_2SO_4 for pH 6, and $CaOH_2$ for pH 8 and 12. It was observed that both stainless steels remained passive at pH 8, typical pH value of carbonated concrete. SUS410L showed corrosion at pH 3, while SUS304 remained low in corrosion for all pH values. SD295A corroded at pH 8 and below.

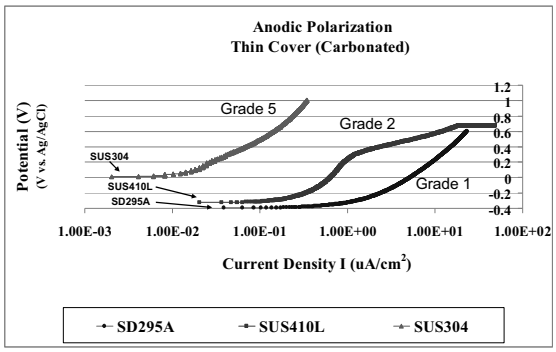

Figure 6: Anodic Curves for Thin Cover Specimens

3.4 Conclusions and Recommendations

The following conclusions were derived from the study to address the objectives: **(1)** Carbonation was not a great threat for both SUS410L and SUS304 stainless steels in properly covered concrete; even with high water/cement ratio (0.7w/c) and increased temperature (40ºC) exposure. **(2)** Galvanic effect did not pose a great threat to the steels in contact even as stainless steels were promoted as cathode and carbon steel as anode for carbonated scenarios. The cracks defect in concrete exposed to carbonation induced greater macrocell corrosion for the steels, however, stainless steels remained relatively low in corrosion compared to SD295A and had no visible corrosion tendency. Thin cover (3mm) scenario with carbonation lowered the corrosion resistance of SUS410L where pitting corrosion tendencies were visually observed. Carbonation was then considered to be a threat for SUS410L in thin cover scenarios. **(3)** Chloride effect was significantly enhanced by carbonation, causing corrosion for SUS410L and SD295A (3kg/m^3 Cl^- with 3mm cover). It was also observed in pH solutions that stainless steels remained passive at pH 8, typical pH of carbonated concrete.

Overall, carbonation was not a great threat for stainless steels; however, some environmental factors enhanced its effects. The new economical stainless steels (ex. SUS410L 12% Cr) with lowered chromium content merit caution when used in carbonated environments, especially with thin cover scenarios.

The following are recommendations for the usage of stainless steels: **(1)** For carbonated scenarios with proper concrete cover, the economical stainless steel SUS410L has sufficient corrosion resistance; even with high water/cement ratio (0.7w/c) and high temperature (40ºC) exposure. **(2)** The economical Stainless Steel SUS410L was much better than SD295A for cracked and thin cover concrete scenarios exposed to carbonation. However, SUS410L was found not to be completely immune to thin cover under carbonation. Hence, usage in these scenarios needs proper consideration. The more expensive stainless steel SUS304 is more reliable for thin cover scenarios under carbonation. **(3)** Use of Stainless Steel SUS410L in scenarios with chloride and concrete carbonation needs proper consideration; SUS304 is more reliable for simultaneous chloride and carbonation scenarios.

References

[1] U. Nurnberger and W. Beul (1999), Corrosion of Stainless Steel Reinforcement in Cracked Concrete, OTTO-Graf-Journal, V.10 (1999), 23-37.

[2] C.F. Chang, J.W. Chen (2004), The Experimental Investigation of Concrete Carbonation Depth, Cement and Concrete Research, 36 (2006), 1760 – 1767.

[3] S. Miyazato, N. Otsuki, and H. Kumura (2001), *Estimation Method of Macrocell Corrosion Rate of Rebar in Existing Concrete Structures Using Non-Destructive Tests,* East Asia-Pacific Conference (EASEC 8), 2, pp.531-541.

[4] M. Bacay (2006), Influence of Construction Defects on the Corrosion Behaviour of Steel in Concrete Exposed to Carbonation and Chloride Attack, (Doctoral dissertation, IDE, Tokyo Institute of Technology, 2006), Japan.

[5] N. Otsuki, S. Nagataki, and K. Nakashita (1992), Evaluation of $AgNO_3$ Solution Spray Method for Measurement of Chloride Penetration into Hardened Cementitious Matrix Materials, ACI material Journal, 89 (1992), 587-592.

[6] A. Bentur, S. Diamond & N.S. Berke (1997), Steel Corrosion in Concrete: Fundamentals and Civil Engineering Practice, p. 7-19, UK, E & FN Spon.

[7] Imperial College Of Science, Technology And Medicine (2002, February 14), Stainless Steel Corrosion Mystery Solved By UK Researchers, ScienceDaily, Retrieved July 21, 2009, from http://www.sciencedaily.com/releases/2002/02/020214080414.htm

DEVELOPMENT OF A VISIBLE LIGHT RESPONSIVE COMPOSITE PHOTOCATALYST FOR PCE TREATMENT

Student Number: 08M18016　Name: Go ISHIDA　Super visor: Hirofumi HINODE

新規可視光応答型複合触媒を用いた有機塩素化合物の分解

石田 豪

現在テトラクロロエチレン（PCE）などの有機塩素化合物による地下水汚染が発生しているが、このような化学物質は産業活動を継続発展させるために必要不可欠な物質である。そのため、これらの化学物質の高度処理システムの開発が急務である。本研究では有機塩素化合物として広く使用されている PCE を選び、その簡易かつ省エネルギーな除去方法として、太陽光が利用できる可視光応答型触媒である多層カーボンナノチューブと二酸化チタンの複合触媒（TiO_2-MWNT）を開発し、PCE 光分解実験によって評価を行った。実験の結果、TiO_2-MWNT 触媒にシナジー効果が現れ、可視光照射下でも TiO_2-MWNT 複合触媒により PCE を光分解することができた。

1. Introduction

Chlorinated organic compounds such as trichloroethylene (TCE) and tetrachloroethylene (PCE) have been widely used as industrial solvents for degreasing metals and dry cleaning. However, they are commonly found to contaminate water, soil and air due to their low biodegradability, toxicity and high persistence in the environment. In water environment, contamination usually occurs in groundwater. The treatment of groundwater contaminated with PCE will be very costly and requires long treatment time due to large amount of groundwater that must be treated. Although some effective PCE treatment methods have been established for industrial purposes, there is still no practical method for groundwater treatment. Some methods such as adsorption using activated carbon or bioremediation have been researched recently. In adsorption using activated carbon, secondary treatment is needed for the used active carbon. In bioremediation, the treatment period needed is long. There is also treatment by photodegradation using photocatalyst. This method requires relatively short treatment period and no secondary treatment. However, Only UV responsive photocatalyst is used.

Titanium dioxide (TiO_2) was widely used as photocatalyst to degrade contaminants. However, it doesn't respond to visible light. Therefore, visible light responsive composite photocatalysts have been developed. TiO_2 supported on carbon nanotube showed promising results in adsorptive ability and photoactivity under visible light irradiation [1]. Using this photocatalyst, low energy cost, short treatment period and simple treatment process could be achieved. Furthermore, many other composite photocatalysts under visible light irradiation such as Fe:Nb-TiO_2 were also developed [2].

In this study, the photodegradation of PCE

under visible light irradiation using composite photocatalyst of TiO_2 and multi-walled carbon nanotube (MWNT) was investigated. The composite catalyst was named TiO_2-MWNT. Figure 1 shows the schematic figure for the contaminated groundwater treatment system. First, the groundwater which is polluted by PCE is drawn by the pump to reaction tank. And then, PCE in the groundwater is degraded by the photocatalysts under visible light irradiation. Finally, clean groundwater is returned to underground.

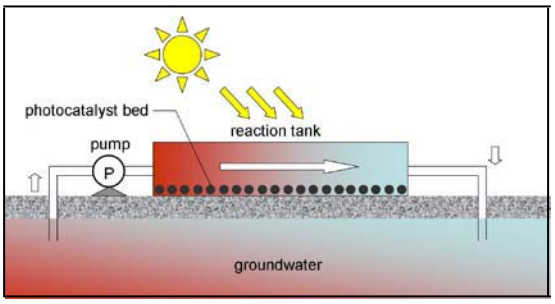

Figure 1 New concept for treatment of PCE in groundwater by photocatalyst

2. Experimental

2.1 Cut of MWNT

As prepared MWNT contained many impurities such as catalysts used in synthesis, it was firstly washed in concentrated HCl under magnetic agitation for 5 hours and filtered to eliminate these catalysts. After that, cutting procedure of MWNT was carried out to enlarge the specific surface area and increase the amount of adsorption. The cutting procedure was as follows: 250 mg pretreated MWNT was suspended in 300 ml of concentrated H_2SO_4 under magnetic agitation for 30 min at room temperature and then 180 ml of concentrated HNO_3 was added. After that, the mixture was heated at 60℃ for 6 h. The MWNT was collected on a glass fiber filter and washed with deionized water until the pH value reached neutral [3]. The cut MWNT was characterized by TEM and BET.

2.2 Preparation of TiO_2-MWNT catalyst

TiO_2-MWNT was synthesized by sol-gel method. The precursor, titanium tetraisopropoxide (TTIP) or tetra-n-butoxy titanium (TNBT) was hydrolyzed to form TiO_2 and deposited on MWNT with the aid of supersonic treatment [4]. The preparation was carried out as follows: 0.1 mg of MWNT was put into 20 ml of ethanol under supersonic treatment for 0.5 hour and then 3.60 ml of TTIP or 3.99 ml of TNBT was added followed by supersonic treatment for 0.5 hour. After that, 80 ml of deionized water was added under supersonic treatment for 0.5 hour. Obtained grey sol-gel liquid was aged at room temperature for 10 hours and then dried at 100℃ for 10 hours. The obtained solid was calcinated under N_2 atmosphere at 400℃ for 1 hour. Synthesized catalyst was named X-TiO_2-MWNT, where X corresponds to the weight percentage of MWNT in TiO_2-MWNT composite catalyst. In this study, X is fixed at 10. The catalysts were characterized by SEM, TEM, TG, and XRD.

2.3 Photodegradation experiments

The evaluation of TiO_2-MWNT photocatalytic activity for degradation of PCE was conducted under UV-vis irradiation. The experiments were carried out in a glass photochemical reactor. The reactor was equipped with a UV and visible light lamp (100 W, 300 nm ~ 600 nm) located axially and held in a quartz immersion, and a UV-cut film which allows only visible light (400 nm ~ 600 nm) to pass. The UV photodegradation experiments

were carried out without the UV-cut film and the visible light photodegradation experiments were carried out by applying the UV-cut film on the lamp. The experiments were done in a closed system. Before irradiation, the PCE solution with photocatalyst was stirred in a dark condition for 1 hour to establish an adsorption-desorption equilibrium.

3. Results and discussion

3.1 Characterization

The TEM images of MWNT and cut MWNT are shown in Figure 2.

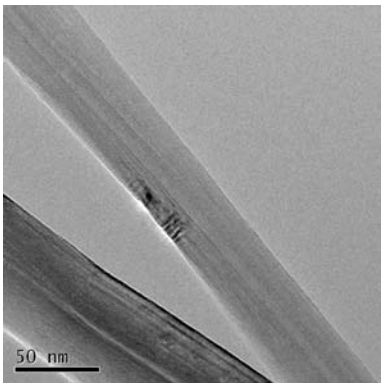

(a) MWNT

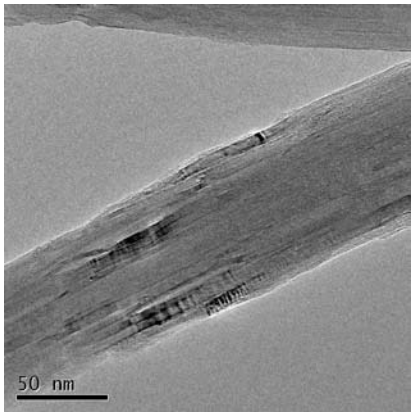

(b) cut MWNT

Figure 2 TEM images

Compared to the one before cutting, the cut MWNT surface became rougher. The BET surface area of MWNT and cut MWNT were 23.6m^2/g and 40.1m^2/g, respectively, which means that the cut MWNT's surface area increased 1.7 times.

The XRD results of TiO_2-MWNT are shown in Figure 3. Only anatase structured titania was found from the XRD patterns of TiO_2 and TiO_2-MWNT. Anatase structure is known to contribute to the photoactivity.

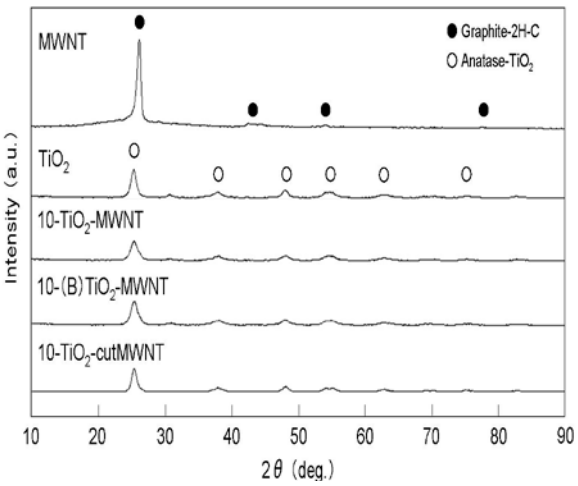

Figure 3 XRD results

3.2 Photodegradation of PCE

Figure 4 shows the PCE degradation by photocatalysts under UV-vis irradiation. 10-(B)TiO_2-MWNT was prepared using TNBT as TiO_2 precursor. High conversions of PCE were observed for 10-TiO_2-cutMWNT, 10-TiO_2-MWNT, 10-(B)TiO_2-MWNT, and TiO_2.

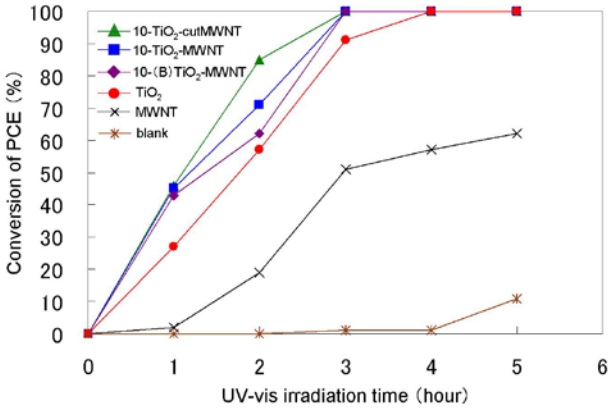

Figure 4 PCE degradation under UV-vis irradiation

Figure 5 shows the PCE degradation by photocatalysts under visible light irradiation. TiO_2-MWNT catalyst showed higher photocatalytic activity than TiO_2. The improved photocatalytic activity of TiO_2-MWNT catalyst might due to the synergetic effect between TiO_2 and MWNT [5].

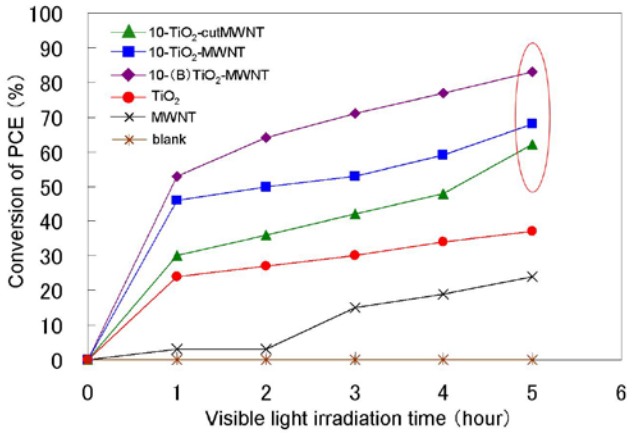

Figure 5 PCE degradation under visible light irradiation

3.3 photodegradation mechanism

The PCE photodegradation mechanism (Figure 6) could be explained as follows: considering the semiconductive properties of carbon nanotubes, MWNT may absorb the irradiation and transfer the photo-induced electron (e^-) into the conduction band of the TiO_2 particles. Simultaneously, a positive charged hole (h^+) might be formed by electron migrating from TiO_2 valence band to MWNT. With this understanding, the role played by MWNT can be illustrated by injecting electrons into TiO_2 conduction band under visible light irradiation and triggering the formation of very reactive radicals superoxide radical ion $O_2^{\cdot -}$ and hydroxyl radical $HO^{\cdot}$, which are responsible for the degradation of the organic compound [5].

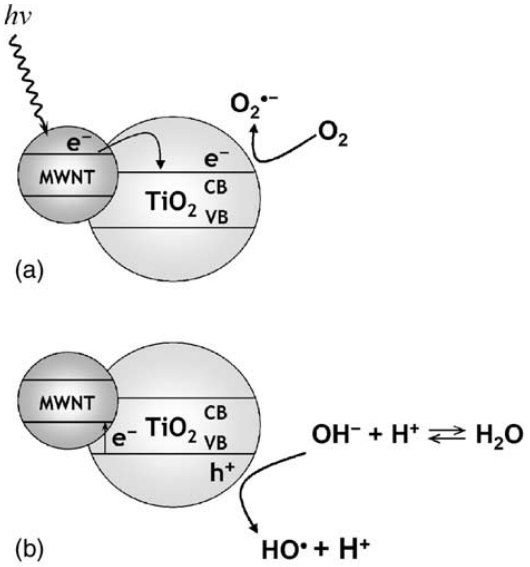

Figure 6 Photodegradation mechanism [5]

4. Conclusion

TiO_2-MWNT composite photocatalyst was prepared by a modified sol-gel method. The new catalyst was effective under visible light irradiation for PCE treatment by the synergetic effect between TiO_2 and MWNT.

Reference

[1] Tomonori, OGATA, the dissertation for Master Degree of Engineering, 2005

[2] Carl Renan Estrellan, Chris salim & Hirofumi Hinode, "Photocatalytic activity of sol-gel derived TiO_2 co-doped with iron and niobium", Reaction Kinetics and Catalysis Letters (2009) 98: 187-192

[3] J. Li, Y. Zhang / Applied Surface Science 252 (2006) 2944–2948

[4] Zhiwei, Wu, the dissertation for Master Degree of Engineering, 2008

[5] W.Wang et al./ Journal of Molecular Catalysis A: Chemical 235 (2005) 194–199

Influence of temperature on sulfate resistance of cementitious material including blast furnace slag, anhydrous gypsum and lime stone powder

Student Number: 08M18022 Name: Takahisa UCHIDA Supervisor: Nobuaki OTSUKI

高炉スラグ微粉末，石灰石微粉末及び無水石膏を混和したセメント系材料の耐硫酸塩性に及ぼす温度の影響

内田雄久

普通コンクリートが硫酸塩の作用により膨張破壊することが報告されており，石膏(Gyp)や石灰石微粉末(LSP)，高炉スラグ微粉末(BFS)を普通ポルトランドセメント(OPC)に混和させることで硫酸塩劣化を抑制する検討がなされている。しかしながら、硫酸塩土壌が数多く存在する中東地域は温度が高いことから浸漬温度を変化させた研究が求められている．そこで本研究は Gyp，LSP を混和し BFS の混和率を変化させたセメント系材料の耐硫酸塩性に及ぼす温度の影響を 23℃および 40℃にて検討を行い，40℃環境下で耐硫酸塩性を向上させることを目的とした．耐硫酸塩性の評価はペーストの膨張による長さ変化試験にて行い，水和生成物と関連付けて考察した．また，モルタルに適用し圧縮強度および外観変化へ及ぼす影響も検討した．

1. Introduction

One of the causes of concrete deterioration is expansion failure due to sulfate attack. Such deterioration was reported in Middle East Asia and East Saudi Arabia[1)] and in the recent years, in Japan. From these reports, sulfate deterioration is reckoned to be the main cause of concrete damage here and abroad.

There are two mainly reasons that sulfate deterioration occurs. One is caused by crystal growth pressure when monosulfate or calcium aluminate hydrates react with sulfate to form ettringite[6)]. Another is caused by crystal growth pressure when calcium hydrate (CH) reacts with sulfate ion to form gypsum. Previous researches have been made to improve the concrete resistance against sulfate. These studies involved addition of admixtures such as blast furnace slag (BFS), anhydrite gypsum (Gyp) and lime stone powder (LSP) to ordinary Portland cement (OPC)[2)]. The cases that have been considered were: (1) OPC + BFS + Gyp, (2) OPC + BFS + LSP, and (3) OPC + BFS + Gyp + LSP. Improvement in sulfate resistance was also reported in a previous study in Otsuki laboratory, involving addition of BFS50%, Gyp5% and LSP10% to OPC[3)].

However, these studies were only conducted at normal temperature (around 20°C). Further studies are needed to consider sulfate attack present at higher temperatures. This is in order to simulate the condition in Middle East Asian countries where there exists high amount of sulfate in soil, and where temperature is as high as 40°C.

Therefore, this research is conducted to study the sulfate resistance of mortars containing BFS, Gyp and LSP, when exposed to temperature of 40°C. Influence of temperature on sulfate resistance was evaluated by measuring the length alternation and examining the appearance after exposure to sulfate solution. Relationship between sulfate resistance and aluminate hydration products were also analyzed. Compressive strength data were also measured before and after being submerged to sulfate solution.

2. Experimental procedure

2.1 Materials used

The materials used in this study were ordinary portland cement (OPC), BFS (basicity: 1.89), anhydrate gypsum and LSP.

Table.1 shows chemical composition of these materials. Fine aggregate used in this study was land sand from Chiba Prefecture (Density 2.62 g/cm^3, water absorption 1.58%)

Table.1 Chemical composition

	ig-loss	SiO_2	Al_2O_3	Fe_2O_3	CaO	MgO	SO_3	Na_2O	Specific surface area(cm^2/g)
OPC	1.07	20.37	5.57	3.38	63.17	2.04	2.48	0.42	3300
BFS	0.49	33.6	14.26	0.41	43.13	6.05	-	0.24	4550
a-Gyp	0.85	1.0	0.3	0.1	40.5	0.1	56.8	-	3990
LSP	43.2	0.33	0.10	0.05	55.8	0.19	-	0.01	7610

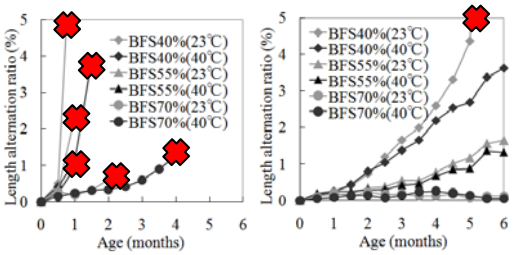

(a) Only BFS (b) BFS+Gyp5%

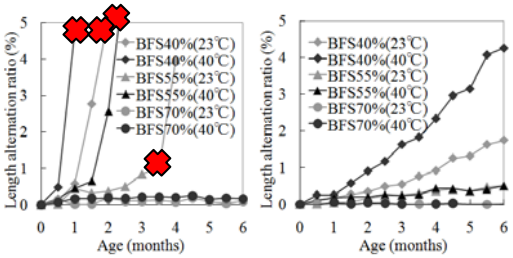

(c) BFS+LSP10% (d) BFS+Gyp5%+LSP10%

Fig.1 Length examination

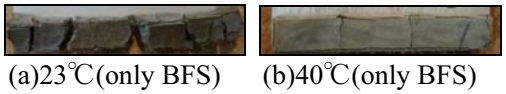

(a)23℃(only BFS) (b)40℃(only BFS)

(c)23℃(BFS+Gyp5%) (d)40℃(BFS+Gyp5%)

(e)23℃(BFS+LSP10%) (f)40℃(BFS+LSP10%)

(g)23℃(B+G5%+L10%) (h)40℃(B+G5%+L10%)

Fig.2 Appearance of cement paste specimens after sulfate solution

2.2 Method of Manufacturing the Specimens

The water binder ratio used was 0.5. Mortars with sand-binder ratio of 2.75 and dimension of 4×4×16cm were made for compressive strength tests based on JIS R 5201. Paste specimens were made for X-ray diffraction exposure test. Mixing of paste specimens for the X-ray diffraction test was conducted by hand for three minutes and was casted into 1×1×8cm molds.

2.3 Setting of Curing

In this study, curing method used was water curing. Specimens were cured in the mold for 24 hours. After, specimens were then cured in water for 7days. After water curing, the specimens were submerged in 5% Na_2SO_4 and were separately exposed to two temperature conditions, 23°C and 40°C.

The specimens for X-ray diffraction were submerged in acetone and placed inside the vacuum dessicator for 24 hours to dry on predefined age.

2.4 Method of Experiment

Sulfate resistance was evaluated based on length alternation tests. According to ASTM standards, if length alternation is less than 0.1%, specimens are said to be safe from sulfate attack. For this study, the researchers interpret it as specimens having high sulfate resistant.

For X-ray diffraction test, X-ray peak heights of aluminate hydration products in the paste specimens were measured at specific age intervals within the duration of exposure to 5% Na_2SO_4. The results for this tests showed that the aluminate hydration products that specifically influenced sulfate deterioration were ettringite, monosulfate, hemicarbonate and monocarbonate.

The X-ray peak height value is measured by subtracting the height of background X-ray from the X-ray peak height. The reference material used for the internal reference method was α-Al_2O_3 which was added as 10% of the sample.

Appearance of hardened paste specimens were photographed and examined at specific age intervals within the exposure duration to Na_2SO_4 with the use of digital camera.

Compressive strength were measured based on JIS R 5201.

3 .Results and Discussion

3.1 Length alternation

Fig.1 shows the experiment result of the length alternation test while Fig.2 shows the appearance of specimens after exposure to sulfate solution. For the case of mixing only BFS, all specimens were deteriorated. For the case of mixing BFS, and either Gyp5% or LSP10%, for both 40% and 55% BFS, length alternations were large and the specimens were deteriorated. At BFS70%, however, length alternations were small but were more than 0.1%, so the specimens were interpreted to have low resistance to concrete.

For case of mixing BFS, Gyp5% and LSP10%, for both BFS40% and 55%, length alternations were also large. On the other hand, at BFS70% length alternations were less than 0.1%. Moreover, specimens exposed to either 23°C or 40°C exhibited almost the same length alternations and did not develop cracks. Therefore, the result showed that the mixture BFS70% with Gyp 5% and LSP 10% has good sulfate resistance even at 40°C.

3.2 Amount of calcium hydrate

Fig.5 shows the amount of CH. The amount of CH at BFS70% was lower than at BFS40% before being submerged even if Gyp and LSP were mixed.After being submerged, the amount of CH decreased at 23°C and 40°C. It was confirmed that

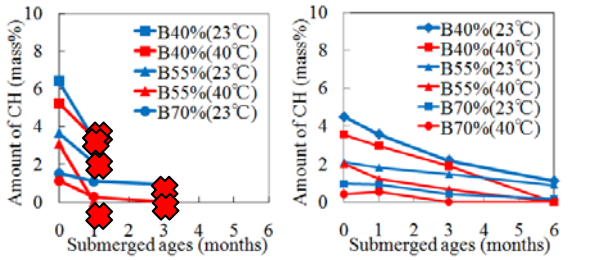

(a)BFS40% (b) BFS+Gyp5%+LSP10%

Fig.3 Amount of CH

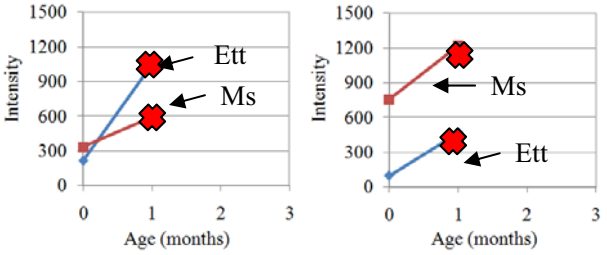

(a)23℃(BFS40%) (b)40℃(BFS40%)

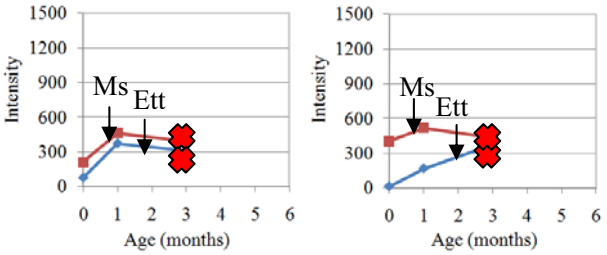

(a)23℃(BFS40%) (b)40℃(BFS40%)

Fig.4 X-ray peak height of the alminate hydroproducts (only BFS)

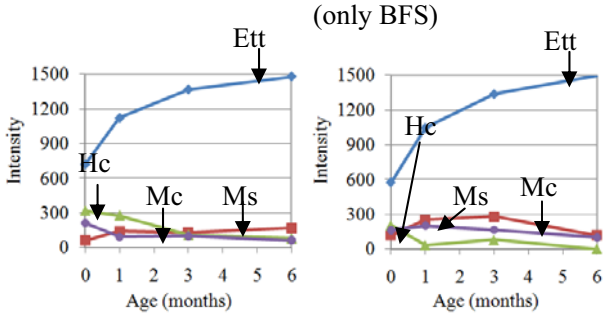

(a)23℃(BFS40%) (b)40℃(BFS40%)

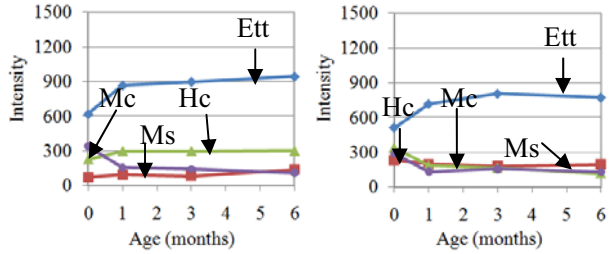

(a)23℃(BFS70%) (b)40℃(BFS70%)

Fig.5 X-ray peak height of the alminate hydroproducts (BFS+Gyp5%+LSP10%)
(ettringite (Ett), monosulfate(Ms), hemicarbonate (Hc) and monocarbonate(Mc))

is expansion potential hydrate.

3.3 X-ray peak height of the aluminate hydration products

Fig.3 shows the X-ray peak height of the aluminate hydration products. For the case of mixing only BFS40%, ettringite was not detected and monosulfate was detected before exposure to sulfate solution (0 months). After exposure, the peak height of ettringite increased, while monosulfate remained the same, for both 23°C and 40°C. Therefore, it is considered that this mixture (BFS40%) has expansion potential.

For the case of mixing BFS70%, aluminate hydration products were of the same trend as that of BFS40%. In other words, ettigite is not detected.

For the case of mixing BFS40%, Gyp5% and LSP10%, ettringite was mainly produced. Hemicarbonate and monocarbonate were detected before exposure (0 months), however, only small amount of monosulfate were present. Compared to mixing only BFS, for this case, ettringite peak height was higher before exposure.

After exposure, the peak height of ettringite increased and the amounts of it were almost the same for both 23°C and 40°C. Monocarbonate peaks were almost the same before and after being exposure, for both 23°C and 40°C. The peak height of hemicarbonate slightly decreased after 3months; but after that, the peak remained unchanged.

For the case of mixing BFS70%, Gyp5% and LSP10%, aluminate hydration products have the same trend as that of BFS40%, Gyp5% and LSP10%. That is to say, ettringite were mainly produced, and monocarbonate were roughly of the same amount for both cases.

3.4 Discussion

For the case of mixing BFS70%, Gyp 5% and LSP 10%, these specimens' length alternations were less than 0.1% and did not develop cracks.

It is considered that sulfate resistance improved because, with increasing BFS replacement ratio, the amount of CH, which is an expansive substance, decreased.

Moreover, for the same case, mainly ettringite were produced and monocarbonate were present before exposure to sulfate solution. Ettringite was stable in sulfate solution.

Producing ettringite and monosulfate were depended upon the sulfate ion concentration in the hardened body[4]. Monosulfate could be produced when sulfate concentration was low. If LSP was mixed, monocarbonate could be produced instead of monosulfate. So it was considered that production of monocarbonate was important because it was stable in sulfate solution

(a)23℃(only BFS) (b)40℃(only BFS)

Fig.6 Appearance of mortal specimens after sulfate after 6months submerged sulfate solution

(c)23℃(B+G5%+L10%) (d)40℃(B+G5%+L10%)

Fig.7 Appearance of mortal specimens after sulfate after 6months submerged sulfate solution

and it could be improved sulfate resistance.

Therefore, it was considered that this mixture could improve sulfate resistance since ettringite and monocarbonate were more stable in the sulfate solution than monosulfate.

4. Application to mortar

Fig.6 and Fig.7 show the appearance of mortar specimens after being submerged in sulfate solution.

For the case of mixing only BFS, specimens were deteriorated at both 23°C and 40°C. On the other hand, for the case of mixing BFS, Gyp5% and LSP10%, specimens did not deteriorate at both 23°C and 40°C

Fig.8 and Fig.9 show relationship between compressive strength and age of submergence.

At 23°C and 40°C, for the case of mixing only BFS40%, compressive strength decreased for the latter age because specimens were already deteriorated. For the case of mixing BFS70%, compressive strengths still increased with age.

For the case of mixing BFS+Gyp5%+LSP10%, specimens' compressive strengths increased regardless of BFS replacement ratio.

However, only 6 months of exposure was conducted for in study, so additional research is needed.

5. Conclusions

This study considered improvement of resistance of sulfate attack of BFS cement by using anhydrite gypsum and lime stone powder as admixtures, when exposed to two different temperatures. The following were concluded:

1) In case of mixing BFS70%, Gyp 5% and LSP 10%, length alternation were less than 0.1% at 23°C and 40°C. These specimens did not develop cracks.

2) It is considered that sulfate resistance improved with increasing the BFS replacement ratio because the amount of CH, which is an expansive

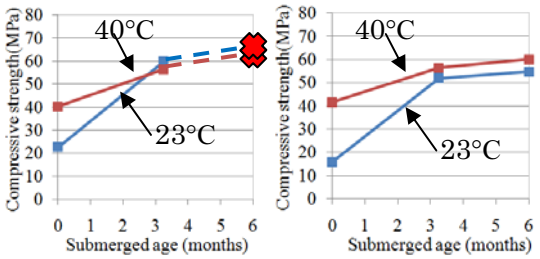

(a):BFS40% (b):BFS70%

Fig.8 Relationship between compressive strength and submerged ages (only BFS)

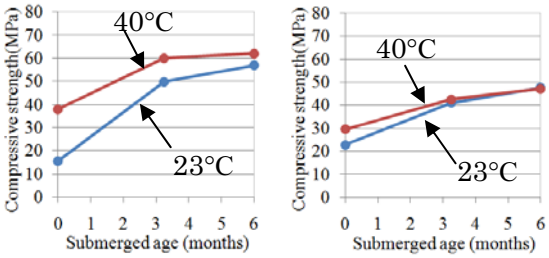

(a):BFS40% (b):BFS70%

Fig.9 Relationship between compressive strength and submerged ages (Gyp5%, LSP10%)

substance, could decrease.

3) In case of mixing BFS, Gyp5% and LSP10%, ettringite were mainly produced, with only a few monocarbonate, before exposure to sulfate. It is considered that this mixture could improve sulfate resistance because hydration products are stable in sulfate solution.

4) When the mixture cases were applied for mortars, for the case of mixing BFS70%, Gyp5% and LSP10%, the specimens did not deteriorate at 23°C and 40°C. Compressive strength was measured to be 45MPa. As a result, this study concludes that to improve sulfate resistance at 40°C, it is needed to add Gyp5% and LSP10% as admixture to cement with BFS replacement ratio of 70%.

【References】

1) Rasheeduzzafar et al., J. ACI, Proc.,Vol.81,No.1, pp.13-20 (1984).

2) Hiroki Yamashita et al., "Futsuu Portland Cement no tai-ryuusanen-sei ni oyobosu-kongou-zai no kouka", Concrete kougaku nenji Ronbun syuu, Vol.29, No.1, pp.213-218(2007).

3) Yun sub Lee et al., "Influence on replacement of anhydrite gypsum and lime stone powder at blast furnace slag cement on sulfate attack", Journal of material science, publishing (2010)

4) Masaki Daimon, "Cement no kagaku – Portland cement no seizou to kouka –"Uchida Rokakuho, pp.50-51 (1989).

Effects of usage conditions on the energy efficiency of boost switching regulator

Student Number: 08M18045　Name: Keisuke OTOME　Supervisor: Kunio TAKAHASHI

昇圧スイッチングレギュレータのエネルギ効率に及ぼす使用条件の影響

乙咩　敬亮

そのままでは電源に利用できない程，開放電圧もしくは短絡電流が小さい電力（些末電力）を利用できれば，身の回りにある様々なエネルギが電力源となり，低環境負荷社会の実現に貢献できる．そのような些末電力は一般に変動が激しい．本研究では，昇圧スイッチングレギュレータで些末電力を昇圧する場合を想定し，昇圧回路のインダクタ，スイッチング周波数，デューティ比，2 次側のインピーダンス，及び些末電力の電流・電圧特性がエネルギ効率に及ぼす影響について理論的及び実験的検討を行った．

1　Introduction

One of the solutions for energy issues, which are set up by the continuous use of fossil fuels is to introduce renewable energy that is clean and abundant. Table 1 shows an estimate of global renewable energy resources at the surface of the earth, and that is estimated more than 100 times amount of energy that we are using now [1]. Usually, we use generator to use renewable energy for instance a solar cell, a thermocouple and piezo element. Although there exist plenty of renewable energy source around us, its generated power is usually quite less than that of common energy plants. The many energy sources around us have so lower voltage and output of renewable energy sources are fluctuated wildly that they have not been used so well, because it is inconvenient to store [2]. And electric energy generated by the sources called tiny electric energy is much less to activate devices, so it needs boost to storage and use that with high efficiency. Boost switching regulator which inductor used is the most efficient booster using now [3][4]. It is generally designed for steady output supply, so effects of usage conditions on efficiency of boost switching regulator are not clear. Thereat the purpose of this paper is to investigate effects of usage conditions on efficiency of boost switching regulator theoretically and experimentally.

Table 1 Estimate of global renewable energy resources at the surface of the earth [1]

Resources	Estimated as recoverable [TW]
Solar radiation	1000
Wind	10
Wave	0.5
Tides	0.1

2　Circuit model

Fig. 1 shows the circuit model of a boost switching regulator including a power supply, P.S. and a load impedance, Z. The boost switching regulator consists of a inductor (inductance, L), a switch, internal resistances of the circuit (at switch 1 on, r_1, at switch 2 on, r_2), a capacitor (capacitance, C) and a internal resistance of the capacitor, r_C. It boosts to Output voltage, v_{out} form input voltage, v_{in} by switching the switch between 1 and 2 continuously, where the on-duration of switch 1 on is T_1 and the on-duration of switch 2 on is T_2, a switching period is T which is sum of T_1 and T_2, and switching duty ratio is D which is proportion of T_1 to T.

Usually, a switch has lag effect of switching behavior and a semiconductor diode's current-voltage characteristic gives its behavior. In order to set up general analytical solution, we regard those effects as a linearly-vary resistance and included internal resistance of the switching regulator in this circuit model.

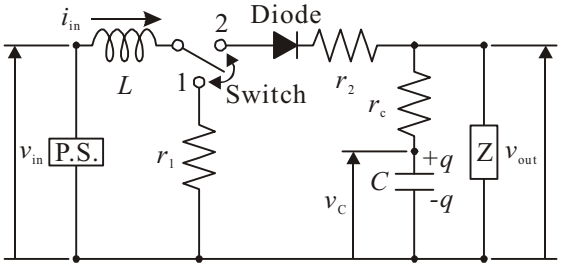

Fig. 1 Circuit diagram of the boost switching regulator on this study

Generators for tiny electric energy have various current-voltage characteristics, for example a solar cell have exponential curve and its open voltage, short-circuit current and curve form changes as light intensity is changed. In this paper, to calculate and experiment, current-voltage characteristic of P.S. is approximated by linear characteristic

$$\frac{v_{in}}{V_s}+\frac{i_{in}}{I_s}=0 \qquad (V_s>0,\ I_s>0) \quad (1)$$

where V_s is open voltage, I_s is short-circuit current of the power supply and i_{in} is input current of the switching

regulator. Because most of characteristics can be written by changing the value of V_s and I_s in Eq. 1 and this is a convenient characteristic to calculate and experiment.

Boost energy efficiency η_{boost} is defined as

$$\eta_{boost} = \frac{E_{out1} + E_{out2}}{E_{in1} + E_{in2}} \quad (2)$$

where E_{in1} is input energy when switch 1 on, E_{in2} is input energy when switch 2 on, E_{out1} is output energy when switch 1 on and E_{out2} is output energy when switch 2 on at the number of switching time n (positive integer) limits infinity. Those are calculated value of integral of multiply current by voltage, can be written by

$$E_{in1} = \int_0^{T_1} \{(V_s - r_s i_{in}) i_{in}\} dt \,, E_{in2} = \int_0^{T_2} \{(V_s - r_s i_{in}) i_{in}\} dt \,,$$

$$E_{out1} = \int_0^{T_1} \frac{v_{out}^2}{Z} dt \,, E_{out2} = \int_0^{T_2} \frac{v_{out}^2}{Z} dt \quad (3)$$

where internal resistance of the power supply $r_s = V_s / i_s$. So i_{in} and v_{out} are required to calculate η_{boost}. The initial value of input current is $i_{in}(0) = 0$ and the initial value of the electric charge of the capacitor q is 0. i_{in} and v_{out} can be expressed by

$$i_{in} = I_1 e^{-\frac{r_1 + r_s}{L} t_1} + \frac{V_s}{r_1 + r_s} \quad (4)$$

$$v_{out} = \frac{ZQ_1}{C(Z + r_C)} e^{-\frac{1}{C(Z + r_C)} t_1} \quad (5)$$

when $(n-1)T \le t \le nT - T_2$,

$$i_{in} = \frac{C_1}{CZ} \{1 + C(Z + r_C)\lambda_1\} e^{\lambda_1 t_2} + \frac{C_2}{CZ} \{1 + C(Z + r_C)\lambda_2\} e^{\lambda_2 t_2} \quad (6)$$

$$v_{out} = \frac{C_1}{C}(1 + C r_C \lambda_1) e^{\lambda_1 t_2} + \frac{C_2}{C}(1 + C r_C \lambda_2) e^{\lambda_2 t_2} + \frac{q_s}{C} \quad (7)$$

when $nT - T_2 \le t \le nT$

where $t_1 = t + T_2 - nT$, $t_2 = t - (n-1)T$, I_1, Q_1, C_1, C_2, λ_1, λ_2 and q_s are constant. So substituting Eq. 3, 4, 5, 6 and 7 expressions into Eq. 2, η_{boost} can be calculated.

Fig. 2 shows an example of time variation of i_{in} and v_{out} where the amplitude of i_{in} and v_{out} are constant. i_{in} runs up during switch 1 is on and the input energy is stored at L, and i_{in} runs down during switch 2 is on, so V_s is boosted v_{out} by induced electromotive force.

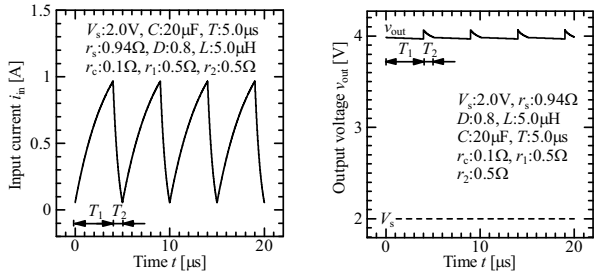

(a) Time variation of i_{in} (b) Time variation of v_{out}

Fig. 2 Time variation of i_{in} and V_{out} where L :5.0μH, C :20.0μF, r_C :0.1Ω, V_s :2.0V, r_s :0.94Ω, Z :50.0Ω, r_1 :0.5Ω, r_2 :0.5Ω, T :5.0μs, D :0.8, n =10001 to 10004

3 Effects of condition on the energy efficiency

3.1 Effect of inductance

Fig. 3 (a)-(c) show examples of the effect of L on η_{boost}. C has no effect on η_{boost}, and not only L but also D and T effect η_{boost}, especially the value of D is heavy dependence on η_{boost}. In Fig. 3 (b), η_{boost} when L =15.5μH and D =0.2 (L_1, η_{boost} =0.77) is 2.75 times more than that when L =15.5μH and D =0.8 (L_2, η_{boost} =0.28). Fig. 3 (d) shows time variation of i_{in} at L_3 (L =1μH), L_4 (L =14μH) and L_5 (L =100μH) in Fig. 3 (c). i_{in} (switch 1 on) is converges faster when L is small, consumed lots of energy at the internal resistance switching regulator. On the other hand, when L is large, the energy stored at L is not enough on duration of switch 1. Therefore, η_{boost} is maximum at L_2.

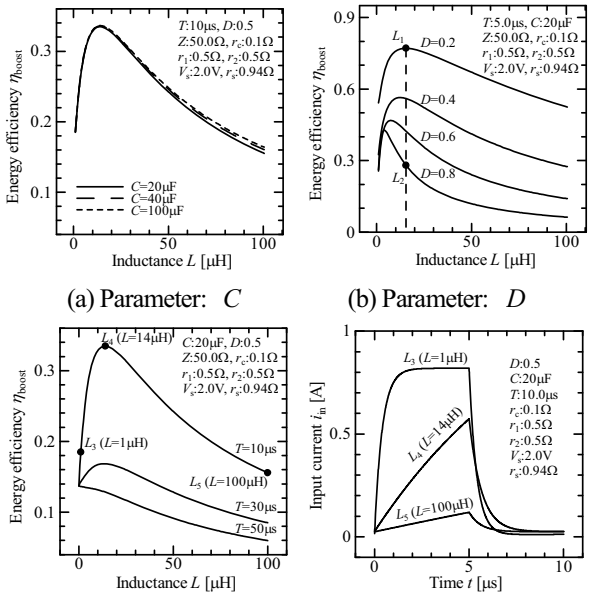

(a) Parameter: C (b) Parameter: D

(c) Parameter: T (d) Time variation of i_{in}

Fig. 3 Effect of L on η_{boost} and time variation of i_{in}

3.2 Effect of switching period

Fig. 4 shows examples of the effect of T on η_{boost}. No effect of C on η_{boost} can be observed in Fig.4 (a). Not only T but also D effect η_{boost}. η_{boost} has maximum value. When T is small, η_{boost} is high. Because i_{in} tends to converge, which means loss of input current become larger when larger T. This effects can be seen in Fig. 4 (b) where η_{boost} tends to lower when D is large.

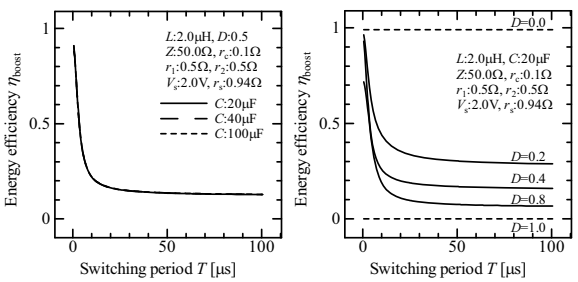

(a) Parameter: C (b) Parameter: D

Fig. 4 Effect of T on η_{boost}

3.3 Effect of switching duty ratio

Fig. 5 (a)-(c) show examples of the effect of D on η_{boost}. Fig. 5 (d) shows time variation of v_{out} at D_1 (D=0.2), D_2 (D=0.5) and D_3 (D=0.8) in Fig. 5 (c). No effect of C on η_{boost} can be observed in Fig.5 (a). The best condition depends on whether it is required high energy efficiency or it needs high output voltage. It is high η_{boost} when D is smaller but it supply lower output voltage when smaller D because energy cannot be stored at L. The difference in η_{boost} at D_2 and D_3 is 0.05, but the difference in average of v_{out} at D_2 and D_3 is 0.4V. So D_3 is better condition than D_2 using as a booster.

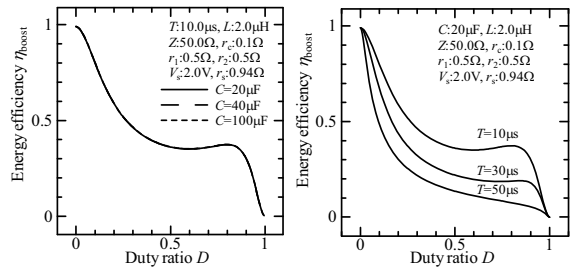

(a) Parameter: C (b) Parameter: T

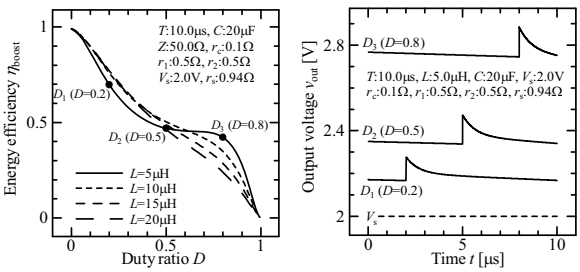

(c) Parameter: L (d) Time variation of v_{out}

Fig. 5 Effect of D on η_{boost} and time variation of v_{out}

3.4 Effect of load impedance

Fig. 6 (a) shows an example of the effect of Z on η_{boost}. η_{boost} has maximum value at Z_2 (Z=50.0Ω). Fig. 6 (b) shows time variation of i_{in} at Z_1 (Z=2.0Ω), Z_2 and Z_3 (Z=500.0Ω) in Fig. 6 (a). Minimum value of i_{in} tends to decrease and energy consumption in the switching regulator becomes smaller as Z is increased. And it does not boost and most of the input energy of switching regulator is consumed in inside the switching regulator when Z has as same order as the internal resistance of the switching regulator. Larger Z tends to converge i_{in} on 0, so output energy decrease as Z is increased. So η_{boost} is maximum at Z_2.

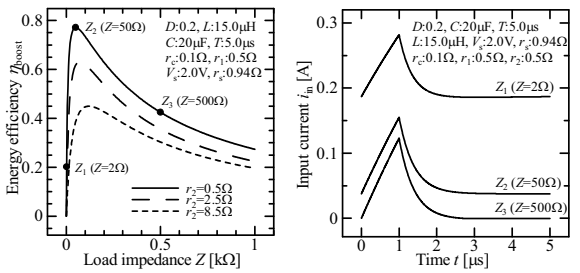

(a) Effect of Z on η_{boost} (b) Time variation of i_{in}

Fig. 6 Effect of Z on η_{boost} and time variation of i_{in}

3.5 Effect of current-voltage characteristic of power supply

Fig. 7 shows examples of the effects of current-voltage characteristic of the power supply. It suggests that V_{s} has no effect on η_{boost} and the power supply provides constant-voltage, where r_{s} =0, is the most efficient. η_{boost} decreases as r_{s} is decreased, because i_{in} tends to increase and the input energy of the switching regulator provided as current, so the input energy is mainly consumed inside the switching regulator when r_{s} become large.

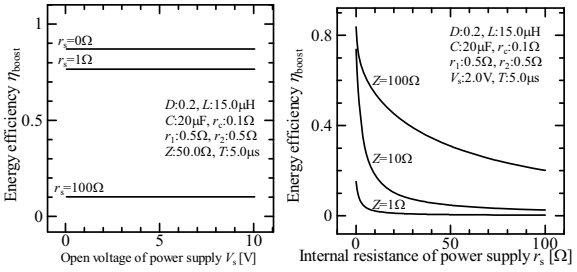

(a) Effect of V_{s} on η_{boost} (b) Effect of r_{s} on η_{boost}

Fig. 7 Effect of V_{s} and r_{s} on η_{boost}

3.6 Effect of internal resistance of switching regulator and the capacitor

Fig. 8 (a)-(c) shows examples of the effect of internal resistance of switching regulator and the capacitor. Larger r_2 and r_{C} decrease η_{boost}. But r_1 is smaller effect on η_{boost} than that of r_2. Because the energy through r_1 is always the loss of switching regulator and larger r_1 tends to decrease i_{in}. According to Eq. 3 and 4, if r_1 is larger than r_{s}, the input energy of the switching regulator also decreases and the loss and the input energy are in inverse proportion to r_1. So the ratio of the loss to the input energy does not change. Therefore r_1 is smaller effect on η_{boost}. But the energy consumed in r_2 and r_{C} are the loss, so larger r_2 and r_{C} make η_{boost} decrease.

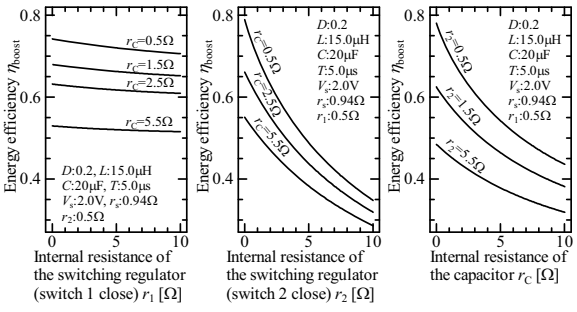

(a) Effect of r_1 (b) Effect of r_2 (c) Effect of r_{C}

Fig. 8 Effect of r_1, r_2 and r_{C} on η_{boost}

4 Experimental system and procedures

A boost switching regulator (SII, S-882Z20, S-8356K30), which can be applied to an input voltage ranged from 0.3V to 3.0V, is used as the booster and Fig. 9 shows its circuit diagram. Fig. 10 shows an experimental system, which consists of a power supply (Matsusada precision, PLE-18-5), a voltage amplifier (op-amp) for measuring the input current of the switching regulator at r_{s} (0.94Ω), and a load

impedance Z (50.0Ω, 93.5 Ω, 990.0Ω). The gain G of the voltage amplifier is obtained as G =10.14. η_{boost} is calculated according to Eq. 9 with the value of Z and v_{out}, v_{in} and the output voltage of the voltage amplifier $v_{\text{rs-2}}$ those are measured by an oscilloscope (Tektronix, TDS2012).

$$\eta_{\text{boost}} = \frac{\int_0^T \left(v_{\text{out}}{}^2 / Z\right) dt}{\int_0^T \left\{\left(v_{\text{in}} v_{\text{rs-2}}\right) / \left(r_{\text{s}} G\right)\right\} dt} \tag{9}$$

5 Results and discussion

Fig. 11 shows experimental results of T and D at each $v_{\text{in-RMS}}$, Fig. 12 (a) shows the effect of $v_{\text{in-RMS}}$ on η_{boost} and Fig. 12 (b) shows a comparison of experimental and theoretical η_{boost} which are calculated using T and D shown in Fig. 11 when Z =50.0Ω, where $v_{\text{in-RMS}}$ is root-mean-square value of v_{in} which is calculated by

$$v_{\text{in-RMS}} = \sqrt{\frac{1}{T}\int_0^T v_{\text{in}} dt}\ . \tag{10}$$

Experimental and theoretical η_{boost} are not fit. The switching regulator changes T to maintain η_{boost} by pulse-width modulation and pulse- frequency modulation switching control. It increases energy consumption of internal resistance of the switching regulator because it needs energy to run the switching control when T is small. It suggests that the switching regulator changes T to decrease switching time where Z =50.0Ω and 93.5 Ω. When Z =990.0Ω, the resistance of the switching regulator mainly depends on Z, so it does not effect on η_{boost}.

Comparisons of experimental and theoretical a switching period time variation of i_{in} and v_{out} are shown in Fig. 13. The value of L considered the range of error inductance (30%) and internal resistance are estimated from each parts spec in theoretical calculation. The theoretical i_{in} has higher maximum and converges faster than that of the measurement, The switching regulator used in this study has capacitor (40μF) at the input of the switching regulator C_{vin} shown in Fig. 9, which could regard the power supply as a constant-voltage power supply. Then r_{s} is small, the limit value of $i_{\text{in}} = r_{\text{s}} / \left(r_1 + r_{\text{s}}\right)$ in Eq. 4 is small. Therefore the maximum value of the theoretical i_{in} is higher than the measurement. Also it could be effect of nonlinear behaviors of inductor, semiconductor diode and lag of switch. The maximum point of experimental v_{out} and that of the theoretical one is at the different time. The measured root-mean-square value of v_{out} is 4.45V and the theoretical calculation is 3.32V. Nonlinear behaviors of inductor and rectification behavior of switching control effect more than that of theoretical calculation.

6 Conclusion

The most efficient usage condition of a switching regulator can be decided by inductor, switching duty ratio, switching period, load impedance and internal resistance. The switching regulator performs most efficient with a constant-voltage power supply. Switching regulator used in this study changes switching period to decrease switching time, and consequently to decrease loss of switching control.

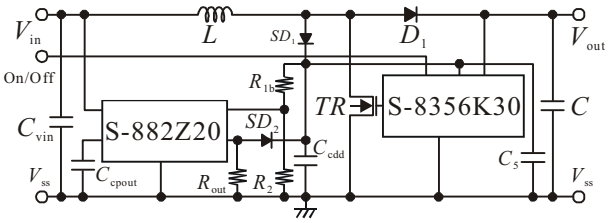

Fig. 9 Circuit diagram of boost switching regulator used

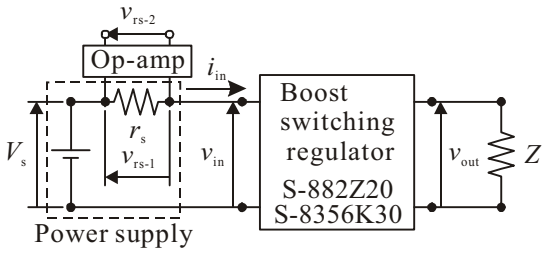

Fig. 10 Illustration of the experimental system used

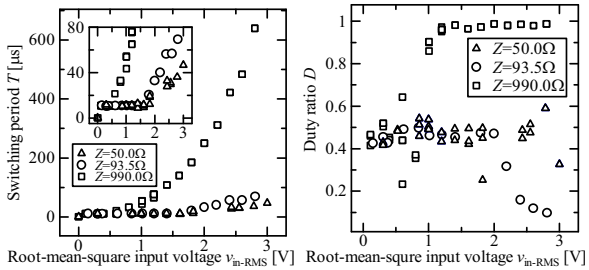

(a) $v_{\text{in-RMS}}$ change of T (b) $v_{\text{in-RMS}}$ change of D

Fig. 11 $v_{\text{in-RMS}}$ change of T and D

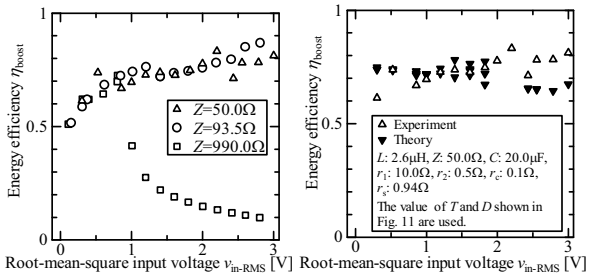

(a) Experiment results (b) Experiment and theory

Fig. 12 Effect of $v_{\text{in-RMS}}$ on η_{boost}

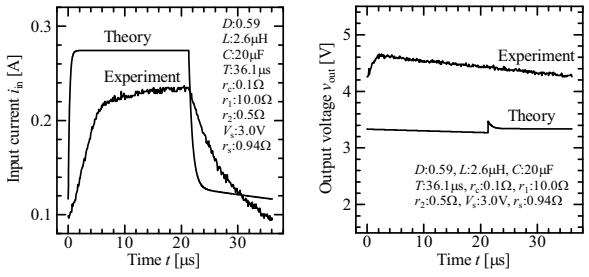

(a) Time variation of i_{in} (b) Time variation of v_{out}

Fig. 13 Experimental and theoretical time variation of i_{in} and V_{out} where L :2.6μH, C :20.0μF, r_{c} :0.1Ω, r_1 :10.0Ω, r_2 :0.5Ω, Z :50.0Ω, V_{s} :3.0V, r_{s} :0.94Ω, D :0.59, T :36.1μs

References

[1] B.Sørensen, Energy Policy 1991, 19 (4), 386-391.

[2]Y.Takefuji, Proc. of international symposium on nonlinear theory and its applications, 2008, 7-10.

[3] Transistor gijutsu, CQ 出版, 2007, 5, p.266

[4] Transistor gijutsu, CQ 出版, 2008, 6, p.151

Research of Cement Hydrate, Porosity and Chloride Penetration into Blast Furnace Cement Concrete Exposed to Marine Environment

Student Number: 08M18051 Name: Takashi KOZAKI Supervisor: Nobuaki OTSUKI

海洋曝露した高炉セメントコンクリートの水和生成物，空隙構造及び塩化物浸透性状に関する研究

小崎尭史

近年，海洋環境において高炉セメントコンクリート(以下 BFC)を利用することが求められている．しかしながら，BFC を実海洋環境で用いた場合の塩化物浸透性状を，水和生成物や空隙構造と関連付けて考察した研究は数少ない．また，コンクリート中への塩化物イオンの浸透は Fick の拡散則で説明され，表面塩化物イオン量，見かけの拡散係数の 2 つの指標が必要となるが，コンクリート表層部においては塩化物イオンの浸透を Fick の拡散則で説明できない事象が報告されている．従って本研究では，(1)実海洋環境に曝露した BFC 中の水和生成物，空隙構造に関して普通セメントコンクリートとの比較を行った．(2)またコンクリート表面から Fick の拡散則で説明できる位置までの距離を，乱れ領域深さと定義し，BFC の表面塩化物イオン量，見かけの拡散係数，乱れ領域深さに与える影響を(1)と関連付けて考察し，BFC 中の塩化物イオンの浸透に関しても考察した．

1. Introduction

Because of the growing need to reduce the amount of CO_2 emission, such as that in cement production, and reduce environmental waste by utilizing steel-making by products, the use of blast furnace cement concrete (BFC) has grown popular in recent years. BFC is also reported to improve the resistance to chloride penetration, making it suitable for marine environment. Therefore BFC is required to use in marine environment. However, there are few studies about chloride penetration into BFC in marine environment related with cement hydrate and pore structure.

Furthermore, chloride penetration into concrete can be explained by Fick's 2nd law. In order to predict chloride penetration, surface chloride content (C_0) and diffusion coefficient (D_{ap}) are needed, these two parameters can be obtained from chloride content distribution.

However, Fig.1 shows that there are cases chloride penetration can't be explained by Fick's 2nd law in concrete surface layer. In this study, this layer is called disrupted area. Thus, the depth of disrupted area (X_0) is needed to predict chloride penetration into concrete more accurately.

Therefore, the following are the objectives:

(1) To compare calcium hydroxide (CH), Friedel's salt (F's salt) content and pore structure of BFC with those of ordinary Portland cement concrete (OPC) when exposed to the marine environment.

(2) To compare C_0, D_{ap} and X_0 of BFC with those of OPC. Moreover, to examine how these parameters are influenced by CH, F's salt content and pore structure.

(3) To consider the prediction of chloride penetration into BFC using X_0.

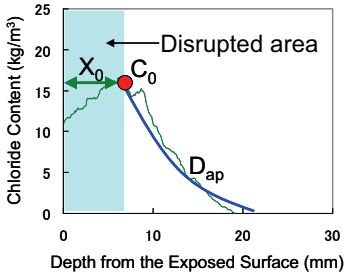

Fig.1 Disrupted area in BFC

Table.1 Mix proportion of BFC

W/C	Unit Weight (kg/m^3)				
(%)	W	C	S	G	Ad
55	164	294	788	1056	2.94

2. Experimental Procedure

2.1 Specimen

The specimens used in this study were BFC and OPC. Table.1 shows the mix proportion of the BFC. The substitution ratio of blast furnace slag to ordinary Portland cement is 50%. The specimens were exposed to the marine environment by placing them under an open-piled pier.

2.2 Method of Experiment

Chloride content was measured based on JIS A 1154, CH content by TG (Thermo Gravimetry) machine, and F's salt by XRD (X-ray diffraction) test. F's salt takes the form $C_3A \cdot CaCl_2 \cdot 10H_2O$. Chloride content in F's salt was then calculated by equation (I)[1]. Pore structure was measured by mercury intrusion porosimetry. Specific chloride content distribution was measured by EPMA (Electron Probe X-ray Microanalysis).

$$y = 0.513x + 0.0213 \quad \text{(I)}$$

y : F's salt / Al_2O_3 integral intensity ratio

x : F's salt content (mass%)

3. Result and Discussion

3.1 Calcium Hydroxide Content

Fig.2 shows CH content of BFC and OPC before exposure to marine environment. CH content of BFC is about 86% lower than that of OPC.

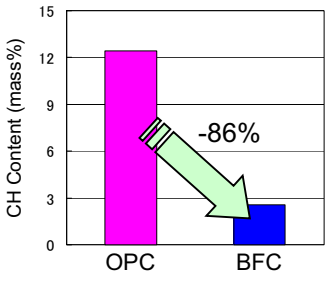

Fig.2 CH content

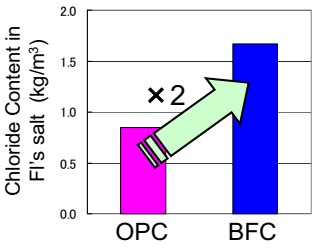

Fig.3 Chloride content in F's salt

3.2 Friedel's Salt Content

Fig.3 shows F's salt content of BFC and OPC after exposure to marine environment. F's salt content of BFC is about twice as much as that of OPC.

3.3 Pore Structure

It is said that pores above φ50nm influence to the diffusion of ion[2]. Fig.4 shows cumulative pore volume above φ50nm of BFC and OPC before exposure to marine environment. Cumulative pore volume above φ50nm of BFC is about 70% lower than that of OPC.

3.4 Surface Chloride Content

Fig.5 shows chloride content distribution of BFC and OPC. C_0 of BFC is larger than that of OPC.

3.5 Diffusion Coefficient

Fig.6 shows relation between total chloride content and D_{ap} of BFC and OPC. D_{ap} of BFC is smaller than that of OPC.

3.6 Depth of Disrupted Area

Fig.7 shows chloride content mapping of BFC and OPC by EPMA, with data taken from a previous study[3]. The data shows that X_0 of BFC is larger than that of OPC.

3.7 Influencing Factor on C_0 of BFC

Fig.8 shows chloride ion content and chloride content in F's salt of BFC and OPC. Chloride content in F's salt of BFC is larger than that of OPC. Therefore, it is concluded that the influencing factor on C_0 of BFC is the increase of F's salt content.

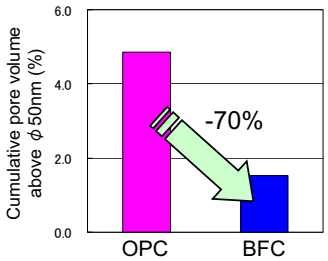

Fig.4 Cumulative pore volume above φ50nm

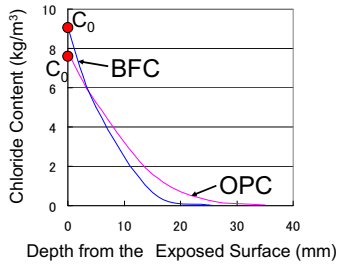

Fig.5 Chloride content distribution

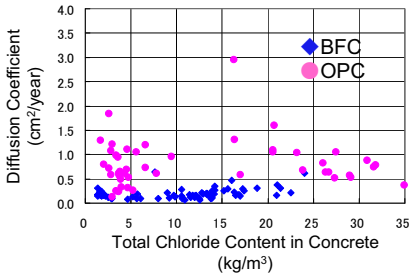

Fig.6 Relation between total chloride content in concrete and D_{ap}

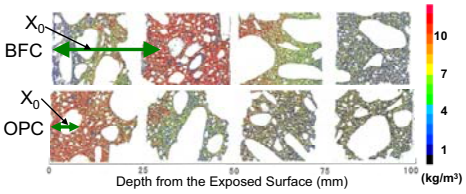

Fig.7 Chloride content mapping by EPMA

3.8 Influencing Factor on D_{ap} of BFC

Fig.9 shows the relation between cumulative pore volume above φ50nm and D_{ap}. It is added the data of BFC 20, BFC 70. The number shows the substitution ratio of blast furnace slag to ordinary Portland cement. Cumulative pore volume above φ50nm decreases with D_{ap} and cumulative pore volume above φ50nm of BFC is smaller than that of OPC. Therefore, it is concluded that the influencing factor on D_{ap} of BFC is the decrease of the cumulative pore volume above φ50nm.

3.9 Influencing Factor on X_0 of BFC

Fig.10 and 11 shows specific chloride content distributions and specific sulfate content distributions in BFC by EPMA. Fig.12 shows Ettringite and F's salt content (a) before sulfate ion penetration and (b) after sulfate ion penetration. In order to further understand the influencing factor on X_0, sulfate ion penetration and the change of cement hydrate is also studied.

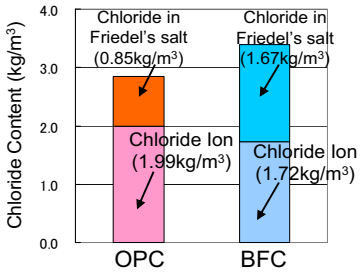

Fig.8 Ratio of chloride content in F's salt

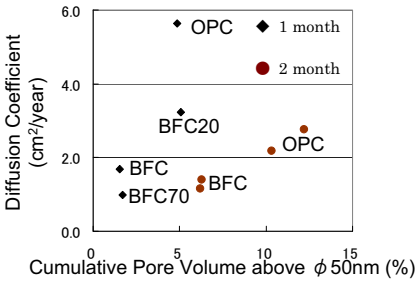

Fig.9 Relation between cumulative pore volume above φ50nm and D_{ap}

X_0 becomes larger, Ettringite content increases and F's salt content decreases with sulfate ion penetration. Cement hydrate reacts with chloride ion from sea water and generates F's salt. However F's salt also reacts with sulfate ion from sea water, and resolves. Thus, it is considered that by F's salt resolution, chloride ion dissolves and moves inside of the concrete. Then, disrupted area occurs in concrete surface layer. F's salt content of BFC is larger than that of OPC. Therefore, it is concluded that the influencing factor on X_0 of BFC is the increase of F's salt content.

3.10 Prediction of Chloride Penetration into BFC

Fig.13 shows the specific chloride content distribution by EPMA. Line 1) shows the true chloride content distribution by EPMA. On the other hand, Line 2) shows calculated chloride content distribution by plot data which doesn't use X_0 and line 3) shows calculated chloride content distribution by plot data which uses X_0. Table.2 shows D_{ap} of each line. Difference of D_{ap} and chloride content distribution compared with true distribution is smaller in case X_0 is used than in case X_0 is not used. Therefore, chloride penetration into BFC can be rationally predicted by using X_0.

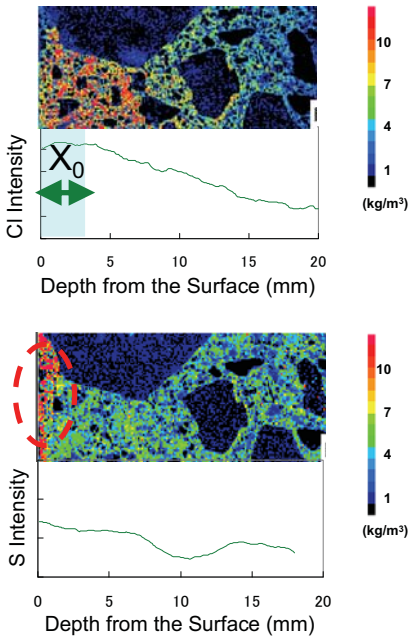

Fig.10 (a) Cl and S content distribution before sulfate ion penetration

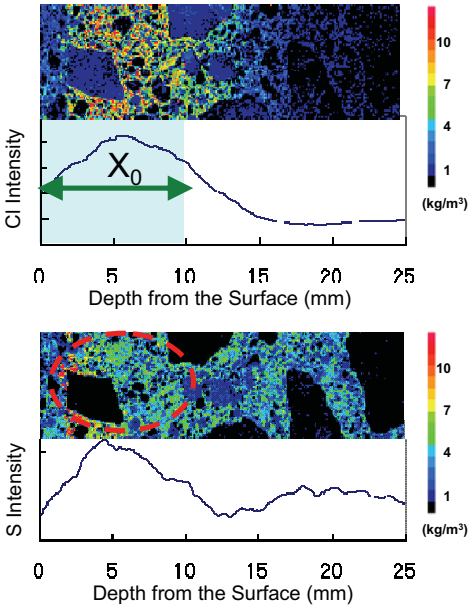

Fig.11 (b) Cl and S content distribution of after sulfate ion penetration

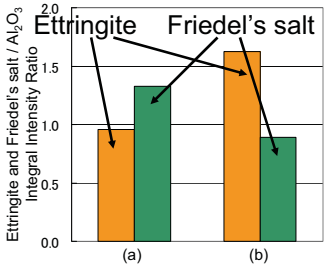

Fig.12 Change of Ettringite and F's salt content (a) before and (b) after sulfate ion penetration

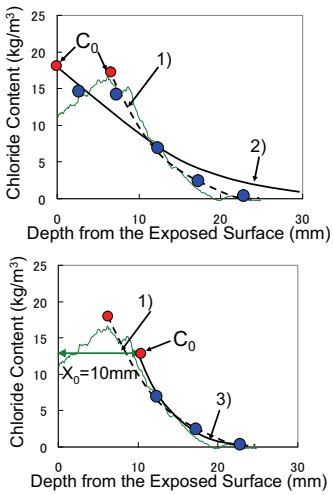

Fig. 13 Comparison of chloride content distribution using X_0 and not using X_0

Table.2 D_{ap} of line 1), 2), 3)

	1)	2)	3)
D_{ap} (cm²/year)	0.146	0.512	0.121

4. Conclusions

The following are the conclusions:

(1) CH content is smaller and F's salt content of BFC is larger than those of OPC. Cumulative pore volume above φ50nm of BFC is smaller than that of OPC.

(2) C_0 and X_0 of BFC is larger than that of OPC because of the increase of F's salt content. D_{ap} of BFC is smaller than that of OPC because of the decrease of cumulative pore volume above φ50nm.

(3) Chloride penetration into BFC can be rationally predicted by using X_0.

【References】

1) Tetsuya I et.al : Cl binding capacity of mortars made with various Portland cement and admixtures, Japan society of civil engineering thesis collection E Vol.63 No1, 14-26, 2007.1

2) H. Uchikawa et.al : 8th International conference on Alkali-aggregate reaction (Kyoto-Japan), Vol.1, pp.121-128, 1989

3) Hidenori H et.al : Properties of Concrete after 30 years' Exposure under Marine Submerged Condition, Japan society of material and science, Vol.54, No8, pp. 842-849, 2005

Experimental Analysis and Modeling of Dual-Polarized MIMO Channel

Student Number: 08M18068 Name: Yohei KONISHI Supervisor: Jun-ichi TAKADA

直交偏波 MIMO システムのための伝搬路特性に関する研究

小西 洋平

本研究においては, 4.5GHz 帯直交偏波 MIMO システムを対象としてマクロセル及びマイクロセル環境におけるフィールド実験をもとに, 偏波特性の解析・モデル化を行った. その結果, マイクロセル環境においてはビル壁による多重反射の影響により水平偏波の減衰が顕著であるのに対し, 実験を行った 2 つのマクロセル環境においては, 互いに異なる減衰特性を示すことが観測された.

1 Introduction

Rapid progress of wireless communication systems results in the demands on more high speed and reliable wireless services. At the same time, it is a big issue to develop spectral efficient wireless systems. In this context, multiple-antenna technique (MIMO system) has appeared as a promising way to contribute these demands. Although MIMO systems offer significant benefits, the performance is heavily dependent on the condition of propagation channel, since such benefits are exploited in multipath-rich environments. The influence of channel condition on the MIMO systems can be mainly observed as performance degradation due to the spatial fading correlation among subchannels. Furthermore, the use of multiple antennas results in the increase of equipment size.

In this regard, adoption of polarization diversity technique into MIMO systems is proposed to realize compact MIMO user terminal keeping inter-subchannel correlations low. Indeed, the earlier studies validated that better separation among channels can be achieved by using dual-polarized antennas [1]. As mentioned above, since the performance of wireless systems in a real-world is determined by the propagation channel condition, knowing the multipath channel including the effect of depolarization through the channel plays a key role in realistic system design. Up to now, despite a number of measurement based studies have been conducted focusing on polarization behavior e.g. [2], some contradictory conclusions are found in these literatures.

In this context, to know the characteristics of polarization in the propagation channel is still a major challenge in the MIMO channel modeling. Therefore, to know the depolarization mechanism in the propagation channel is the main interest of this thesis. More specifically, this study figures out the answers to the following important questions.

1. Do the different polarization pairs suffer same path loss?
2. What are the causal factors of depolarization in the propagation channel?

2 Channel Measurements

The measurements were conducted in the areas around Tokyo, 1. Kawasaki City, 2. Ota ward Tokyo and 3. Oookayama campus of Tokyo Institute of Technology. Table 2 summarizes the basic information of the environments.

2.1 Channel Sounding System

Channel sounding was performed using Medav RUSK-Fujitsu wideband channel sounder [3] in all the three measurement campaigns. As for the array, uniform rectangular array and stacked uniform circular array are used for transmitter and receiver, respectively. Rubidium reference oscillators at both base station (BS) and mobile station (MS) ensure carrier and switching synchronization throughout the measurement duration. The specifications of this measurement system are summarized in Table 1.

Table 1: RUSK-Fujitsu Wideband MIMO Channel Sounder

Carrier frequency	4.5 GHz
Bandwidth	120 MHz
BS antenna array	Uniform rectangular array $2 \times 4 \times 2$ elements (row $\times$ col. $\times$ pol.)
MS antenna array	Stacked uniform circular array $2 \times 24 \times 2$ elements (row $\times$ col. $\times$ pol.) V & H polarized patch antennas
Transmit signal	Wideband multitone
Max. delay setting	3.2 μs

Table 2: Summary of three measurement environments

	Small urban **macrocell**		**Microcell**
	Kawasaki City Kanagawa	Ota ward Tokyo	In campus Tokyo Tech
BS height	85 m	30 m	1.79 m
MS height	1.80 m	1.65 m	1.65 m
BS-MS distance	230 m $\sim$ 400m	186 m $\sim$ 276m	50 m $\sim$ 125m
Structure type	residential & industrial	residential	building canyon

2.1.1 Measurement Environments

Layouts of each measurement setup are shown in Figure 1. With each setup, measurement are conducted midnight under a clear weather and the MS was moved at a slowly walking pace along the street. Distances between each MS positions are 20 m in Macrocell and 10m in a Microcell scenario, starting and ending with static measurements.

In Kawasaki macrocell scenario (Figure 1(a)), BS was placed on top of the building which is highest in this area. Most of other buildings are lower than half of BS height. In Tokyo macrocell scenario (Figure 1(b)), the site consists of four

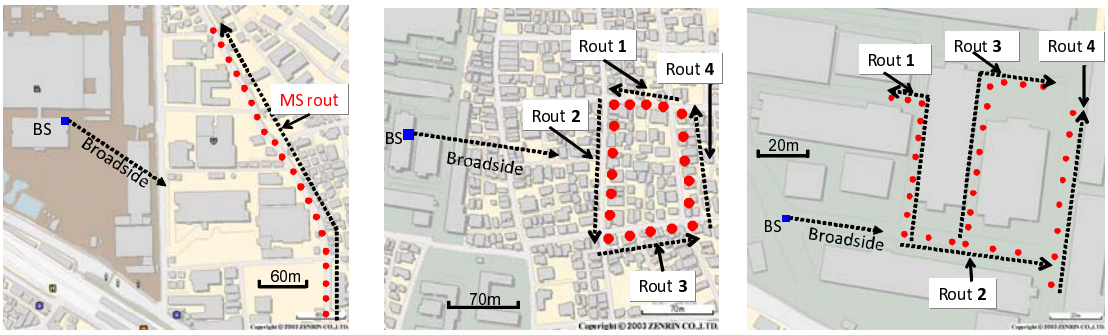

(a) Kawasaki, Macrocell. (b) Tokyo, Macrocell. (c) In campus, Microcell.

Figure 1: Layout of the measurement scenario

streets. Most of the measurement positions are categorized as non-line-of-sight (NLoS) or obstructed-line-of-sight (OLoS) in both of the macrocell scenarios, and observed some LoS paths are excluded in the analysis. In Tokyo Tech campus microcell scenario (Figure 1(c)), the site is divided into 4 routes, to analyze depolarization mechanisms more closely. The routes 1, 3, and 4 in this scenario, the line-of-sight from MS to BS is completely blocked by the buildings, while the sight is open at all the MS positions in route 2.

2.1.2 Parameter Estimation and Multipath Clustering

Estimating the parameters from real-world propagation channel is a essential element of measurement-based channel modeling. maximum-likelihood parameter estimation algorithm named RIMAX is originally developed in [4]. The path delay (τ), direction of departure (DoD) and arrival (DoA) are estimated for the 4 polarization pairs: co-vertical (γ_{VV}), co-horizontal (γ_{HH}), horizontal transmission-vertical reception (γ_{VH}) and vice versa (γ_{HV}). The data model is formulated as superposition of K 6-dimensional Dirac deltas weighted by a 2×2 polarimetric path weights matrix.

$$\begin{aligned}\mathbf{H}\left(\alpha,\tau,\phi_R,\theta_R,\phi_T,\theta_T\right) = \sum_{k=1}^{K} \begin{bmatrix} \gamma_{\mathrm{HH},k} & \gamma_{\mathrm{VH},k} \\ \gamma_{\mathrm{HV},k} & \gamma_{\mathrm{VV},k} \end{bmatrix} \\ \times\delta(\alpha-\alpha_k)\delta(\tau-\tau_k)\delta(\phi_R-\phi_{R_k}) \\ \times\delta(\theta_R-\theta_{R_k})\delta(\phi_T-\phi_{T_k})\delta(\theta_T-\theta_{T_k}) \quad (1)\end{aligned}$$

where ϕ_R, θ_R and ϕ_T, θ_T are the azimuth and elevation angles at MS and BS, respectively. The α is the Doppler-shift, but it is not included in this study due to the limitation of sounding system. The estimated parameters by RIMAX is then, clusterized by using the automatic multipath clustering framework [5]. This is to treat estimated polarimetric parameters in more accurate manner. The automatic clustering framework used in this study is based on following three steps:

1. Local optimization: k-means clustering
2. Global optimization: simulated annealing
3. Determination of number of multipath clusters: average rank aggregation

Therefore, the distance-measure is the most fundamental and important basis of this framework. The detail is available in [5].

3 Results and discussion

3.1 Polarization Characteristics

3.1.1 Formulation of Polarization States

To investigate the influence of polarization states on the system performance, Cross-polarization ratio (XPR) and co-polarization ratio (CPR), are often used. Recently in [6], authors discussed the influence of XPR and CPR on the capacity of dual-polarized systems. The authors concluded that XPR is the most important parameter which dominates the performance of polarized MIMO systems. The definition of cluster polarization ratios in this study is the power ratio of the different polarization combinations.

$$\mathrm{XPR}^{\mathrm{BS}}_{k,\mathrm{V}} = 20\log_{10}\left|\frac{\sum_{l\in\mathcal{C}_k}\gamma_{\mathrm{VV},l}}{\sum_{l\in\mathcal{C}_k}\gamma_{\mathrm{VH},l}}\right| \quad (2)$$

$$\mathrm{XPR}^{\mathrm{BS}}_{k,\mathrm{H}} = 20\log_{10}\left|\frac{\sum_{l\in\mathcal{C}_k}\gamma_{\mathrm{HH},l}}{\sum_{l\in\mathcal{C}_k}\gamma_{\mathrm{HV},l}}\right| \quad (3)$$

$$\mathrm{XPR}^{\mathrm{MS}}_{k,\mathrm{V}} = 20\log_{10}\left|\frac{\sum_{l\in\mathcal{C}_k}\gamma_{\mathrm{VV},l}}{\sum_{l\in\mathcal{C}_k}\gamma_{\mathrm{HV},l}}\right| \quad (4)$$

$$\mathrm{XPR}^{\mathrm{MS}}_{k,\mathrm{H}} = 20\log_{10}\left|\frac{\sum_{l\in\mathcal{C}_k}\gamma_{\mathrm{HH},l}}{\sum_{l\in\mathcal{C}_k}\gamma_{\mathrm{VH},l}}\right| \quad (5)$$

$$\mathrm{CPR}_{k} = 20\log_{10}\left|\frac{\sum_{l\in\mathcal{C}_k}\gamma_{\mathrm{VV},l}}{\sum_{l\in\mathcal{C}_k}\gamma_{\mathrm{HH},l}}\right| \quad (6)$$

These parameters do not include the influence of measurement antenna, so they only represent the degree of depolarization in the propagation channel.

3.1.2 Theorey of Depolarization Mechanisms

Considering the measurement environments in this study, following factors are expected as dominant propagation mechanisms which cause the difference between VP (horizontal transmission) and HP (vertical transmission) received power.

Macrocell scenarios

- Over-rooftop **diffraction**
- Over-rooftop **diffraction** + **reflection** from the walls of the houses

Microcell Campus scenario

- **Reflection** from vertical walls/pane (window glass) of the buildings
- **Reflection** from the ground (asphalt)
- **Diffraction** at building corner

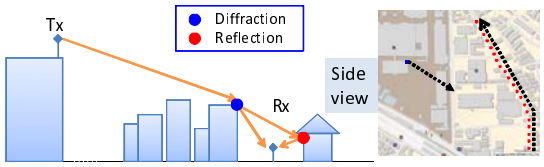

(a) Macrocell scenario

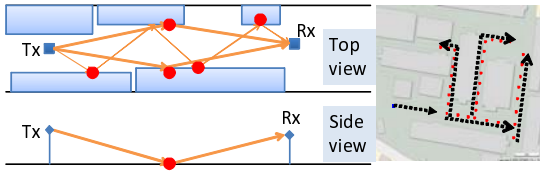

(b) Microcell scenario

Figure 2: Illustration of propagation mechanisms.

Therefore, reflection is a dominant propagation mechanism for all environments in this study. Especially in a Microcell campus scenario, most of the received wave experience reflection from building wall or asphalt road. Earlier studies provide theoretical way to understand difference of VP and HP reflection characteristics for the canonical problems. For example in case of reflection from vertical walls, behavior of VP and HP is greatly different in terms of the reflection coefficient. Both coefficients are unity at grazing incidence and decrease with increasing grazing angle. But no reflection phenomena exists only for the HP wave at a certain angle. The angle is called as **Brewster angle**. For the influence of diffraction, it is well known that VP shows better transmission (higher received power) in shadowing region compared to HP. So, this effect is considered as also applicable in this study.

3.1.3 Cluster Gain of Different Polarization Pairs

Figure 3(a), 3(b) and 3(c) show the results from Kawasaki City (Macrocell), Ota ward Tokyo (Macrocell) and Tokyo Tech campus (Microcell), respectively. Cluster gain $P_{k,RT}$ (subscripts RT indicates the polarization states in receive transmit order) are computed by narrowband approach as follow.

$$P_{k,RT}[\text{dB}] = 20\log_{10}\left|\sum_{l\in\mathcal{C}_k}\gamma_{RT,l}\right| \quad (7)$$

The cluster gain decay characteristics are shown as a function of BS-MS distance with linear fitting line obtained from the method of least squares. In this study, decay characteristics are modeled as:

$$P_{k,RT}[\text{dB}] = (\alpha_{\text{mean}} + \alpha_{\text{diff}}) \times \log_{10}(d) + \beta \quad (8)$$

where d is the distance between BS and MS, α_{mean}, α_{diff} and β are the site-specific constants. Table 3 shows the comparison of fitting parameters among three measurements. Comparing the difference between two Macrocell sites, decay coefficients are quite different. Especially in Tokyo measurement, HP showed better transmission than VP. This results do not match with the results from existing studies, since the VP is expected to show better transmission in shadowing region. Table 4 shows the power proportion of upper and lower horizon against overall received power. It is evident that most of the power comes from upper horizontal direction in both sites, but almost all the power is received from upper horizon in Tokyo measurement. These results indicates the existence of unknown but influential other propagtion mechanisms, which come from upper horizontal direction. As for Microcell scenario, faster decay of HP is clear. This is considered as due to the reflection from vertical walls, which strongly penetrate only the HP (Section 3.1.2).

Table 3: Fitting Parameters for Cluster Gain vs. Distance

[dB]		α_{mean}	α_{diff}	Mean gain
Kawasaki	$P_{k,\text{HH}}$	-90.44	-11.33	-114.7
	$P_{k,\text{VV}}$		8.39	-114.8
Tokyo	$P_{k,\text{HH}}$	-1.03	4.15	-127.96
	$P_{k,\text{VV}}$		4.00	-130.68
Campus	$P_{k,\text{HH}}$	-49.38	7.58	-108.26
	$P_{k,\text{VV}}$		0.37	-103.66

Table 4: Power proportion: [**Elevation** at MS]

		Roof/house	Ground
[%]	Overall	85.7 / 96.3	14.3/3.7
HH	51.2 / 63.5	46.9 / 63.7	77.1 / 58.9
HV	2.3/2.3	2.7/2.2	3.6/3.2
VH	4.7/3.5	3.8/3.3	10.4/7.5
VV	41.3/30.7	46.7 / 30.7	8.9 / 30.8

3.1.4 Cross- and Co-Polarization Ratios

This section presents the behavior of polarization ratios, which is defined in Section 3.1.1. From the definition of CPR, higher CPR indicates the goodness of vertical transmission against horizontal transmission. The severe loss of horizontal transmission in a Microcell in campus scenario is evident from the high CPR (4.5 [dB]). The main interest of this section is to know whether XCPRs are dependent on delay, azimuth and elevation DoA or not. To check the dependencies, the Spearman's rank correlation coefficients are calculated, and shown in Table 5. Blue color indicates the positive correlation, and negative correlation is indicated as red color. Overlooking the table, no clear dependencies are identified for all results. Especially in Tokyo measurement, no dependence on the azimuth DoA is evident. It is interesting that the elevation dependencies of Kawasaki and Tokyo measurement show opposite correlation (positive/negative). This difference may come from the above mentioned unknown mechanisms, but it is difficult to generalize and determine the causal factor only from these results. The further analysis is remained as future work.

4 Conclusion and Future Works

4.1 Conclusion

In this study, multipath cluster polarization model is presented based on the measured data from multiple scenarios

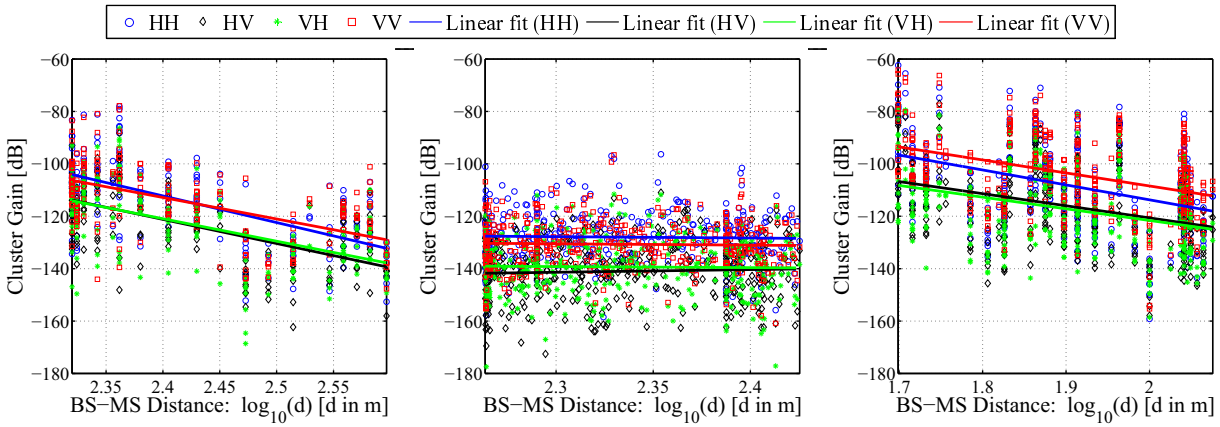

(a) Macrocell, Kawasaki City. (b) Macrocell, Ota ward, Tokyo. (c) Microcell, In campus, Tokyo Tech.

Figure 3: Cluster gain behavior against BS-MS distance

Table 5: Correlation coefficients

Correlation coefficients		Nakahara	Minami 3	Campus
Delay	XPR^{BS}_{V}	0.06	0.15	-0.04
	XPR^{MS}_{V}	0.14	0.08	-0.07
	XPR^{MS}_{H}	-0.15	0.11	-0.11
	CPR	0.23	0.01	0.05
Azimuth MS	XPR^{BS}_{H}	-0.2	0	-0.04
	XPR^{MS}_{H}	-0.12	0	-0.02
	CPR	0.21	0.02	-0.05
Elevation MS	XPR^{BS}_{V}	-0.17	0.16	0.01
	XPR^{BS}_{H}	0.07	0.24	-0.04
	XPR^{MS}_{V}	-0.13	0.21	-0.04
	XPR^{MS}_{H}	0.02	0.19	0
	CPR	-0.21	-0.02	-0.04

at 4.5 GHz. The contribution of this thesis is summarized as follows:

1. The path loss behavior of vertical and horizontal transmissions are observed as different between two Macrocell scenarios. Although this study can not determine the specific mechanisms, the results indicated the existence of unknown but influential propagation mechanism, which come from upper horizontal direction. In Microcell scenario, the horizontal transmission suffer severe path loss due to the reflection from vertical walls. This behavior is theoretically explained, and further the hypothesis testing results insisted that there is no counter-evidence on this subjective observation.

2. The influence of coherent paths in a cluster is identified as significant. The results of this study shows that the superposition of paths in a cluster should be based on a coherent sum approach.

3. XCPRs are identified almost independent on the channel parameters such as delay, azimuth and elevation DoA. However, the mean CPR indicated the better transmission of HP in Macrocell scenario, while VP in Microcell campus scenario.

4.2 Future works

In the future, following items must be analyzed.

1. Influence of coherent 'true path' in a estimated 'path' The estimated path by RIMAX is considered as sum (or split) of 'true path'. So the effect must be taken into account, especially in a cluster-based modeling. More specifically, cluster variation characteristics is needed to be analyzed by continuous measurement with tracking functionality.

2. More detail analysis to know the dominant depolarization factors in a Macrocell scenario is necessary. This should be clarified by conducting more object-specific measurement.

References

[1] V. Eiceg, H. Sampath, and S. Catreux-Erceg, "Dual-polarization versus single-polarization MIMO channel measurement results and modeling," *Wireless Communications, IEEE Transactions on*, vol. 5, no. 1, pp. 28–33, Jan. 2006.

[2] M. Shafi, M. Zhang, A. Moustakas, P. Smith, A. Molisch, F. Tufvesson, and S. Simon, "Polarized MIMO channels in 3-d: models, measurements and mutual information," *Selected Areas in Communications, IEEE Journal on*, vol. 24, no. 3, pp. 514–527, March 2006.

[3] [Online]. Available: http://www.channelsounder.de/ruskchannelsounder.html

[4] A. Richter, "Estimation of radiocchannel parameters: Models and algorithms," Ph.D. dissertation, Ilmenau University of Technology, 2005.

[5] L. Y. Materum, "Mobile station spatio-temporal multipath clustering of MIMO channel estimates of an urban cellular environment at 4.5 GHz," Ph.D. dissertation, Tokyo Institute of Technology, 2009.

[6] W. F. Tsen and H.-J. Li, "Correlations and channel capacities for multi-polarized MIMO systems," in *The 20th Personal, Indoor and Mobile Radio Communications Symposium 2009*, Tokyo, Japan, Sept, 2009.

ENVIRONMENTAL KARTE AS A TOOL FOR REGIONAL COOPERATION ON TOWN DEVELOPMENT IN WATERSHED

Student Number: 08M18074 Name: Kenji KOBAYASHI Supervisor: Manabu KANDA

地域協働による流域まちづくりツールとしての環境カルテ構築

小林　賢司

流域における地域協働による街づくりをサポートするためのツールとして環境カルテを提案した．環境カルテは(1)GISを利用した複合的流域環境情報の一元管理を行う静的データベース，(2)将来シナリオの検討を可能とする水文モデルを導入した動的データベース，(3)地域共同ツールとしての利用，の3本柱で構成される．本研究では環境カルテを呑川流域に適用し，流域の9団体からなる協働の枠組みで複合環境情報の蓄積を行った．また水文予測のためにWater Energy transfer Process モデルを導入した．また環境カルテは地域で利用され，本研究で環境カルテのひな形を作り上げた．

1. Introduction

Nowadays, more non-profit organizations and citizen's organizations engage on town development and environmental improvements. Furthermore, regional cooperation between public administration and citizens are getting more attention. From the view point of the hydrologic cycle and the ecosystem, the watershed is a suitable and important unit of town development and environmental improvement. However, specifying problems related to natural or artificial environment in a basin is difficult because the environment is a complex system and a watershed is often sub-divided by some administrative units. Therefore, a tool for understanding the watershed is necessary for concerned citizens and administrators to propose safe and accurate basin improvements.

Researchers have studied and proposed different methodologies to address this topic. Sadohara et al.[1)] proposed a Spatial Information Platform for Watershed Environment Assessments. This platform enables us to analyze water use or current water cycle and assess the water usage or cycles in the future using ArcGIS and ArcHydro, one of the applications of ArcGIS. Klimaatlas[2)] developed a methodology to know climate conditions in a region and contributed to the city planning in Stuttgart, Germany. However, his Spatial Information Platform lacks climate information and his method neglects water cycle effects. Given this background information, a methodology or tool which could consider all environmental elements including water cycle, climate, ecological system and even a watershed's history is deemed necessary.

Moreover, the tool must be able to gather this information from independent data-providers and in turn share this combined information back to the organizations or whoever would wish to analyze and study the watershed.

As a result, "Environmental Karte" was proposed in this study. The Karte compiles scattered information describing all aspects of an environment within a watershed. It also generates information from remote sensors and uses a hydrological model. This enhances ease of modification of gathered information and assessment of countermeasures in the watershed. The method was applied to Nomikawa watershed, Tokyo.

2. Concept of Environmental Karte

Environmental Karte is a medical record of the watershed since it unifies management of spatiotemporal information which contains up-to-date variety of environmental information, environmental history and environmental status forecasts. Supporting the analogy further, the karte provides diagnostics of a basin's environment delineates the direction of the watershed and provides remedies or countermeasures for potential problems. The Karte's functions (**Fig.1**) are summarized into three, namely;

(1) Compilation of various environmental datasets related to natural and human resources in the watershed using GIS-software (Static Karte),

(2) Creation of a dynamic database by coupling with advanced hydrological or meteorological models, thereby providing future scenarios of watershed development (Dynamic Karte),

(3) Utilization as a means of promoting cooperation among citizens.

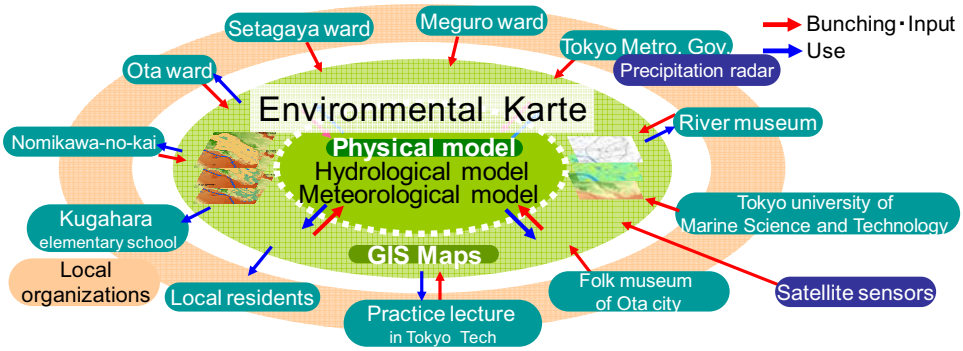

Fig.1 Schematic image of Environmental Karte and its example in Nomikawa watershed

Fig.2 Nomikawa River

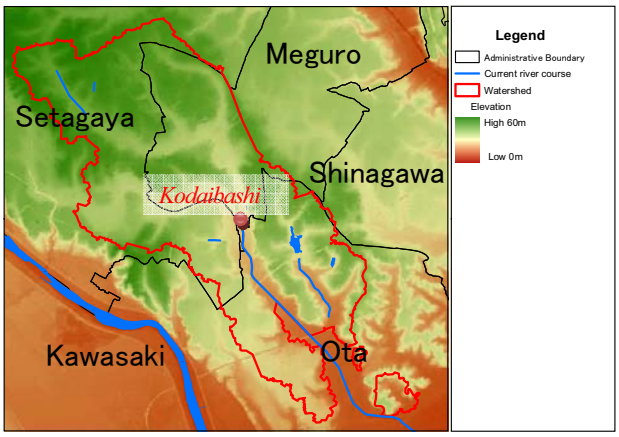

Fig.3 Study watershed and Administrative boundary

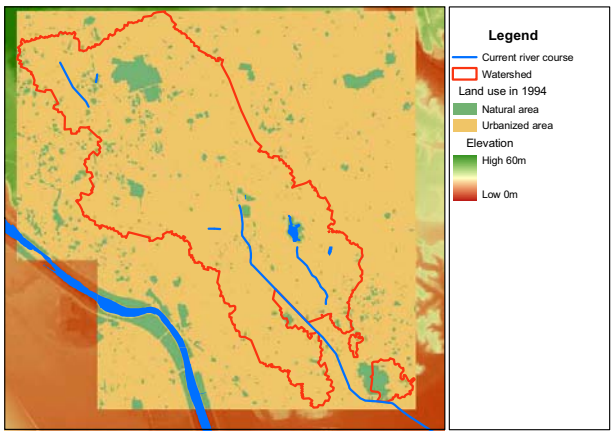

Fig.4 Land use in 1994

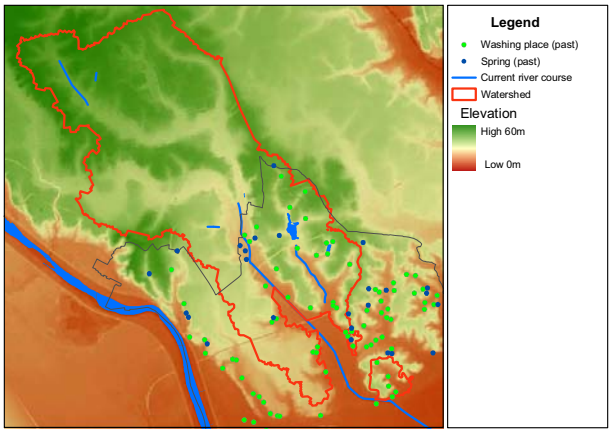

Fig.5 Spring and washing places in the past

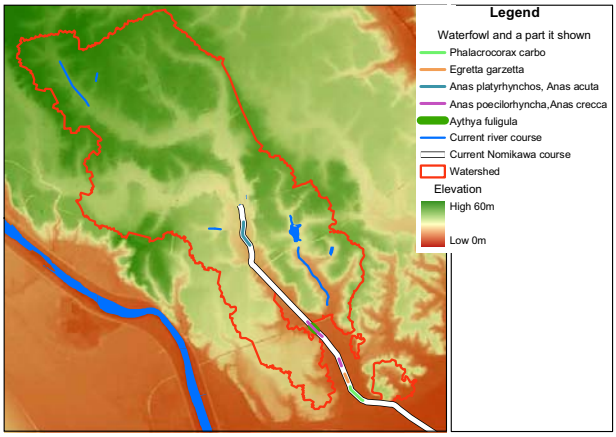

Fig.6 Waterfowl and parts where they were shown

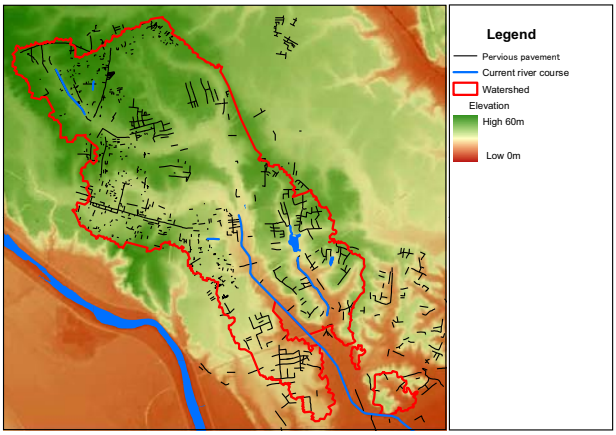

Fig.7 Location of pervious pavement

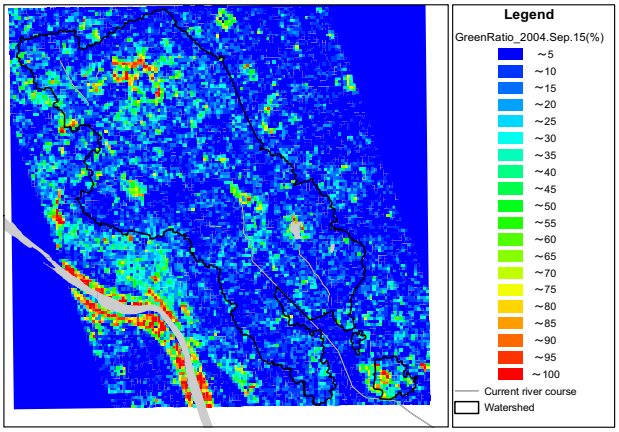

Fig.8 Vegetation ratio (%, in 50m mesh)

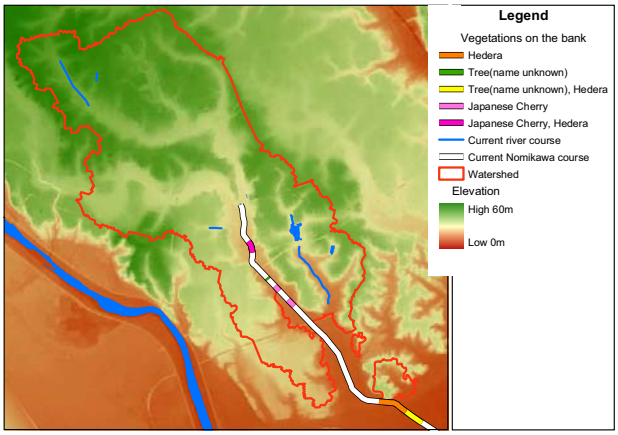

Fig.9 Vegetation on the bank

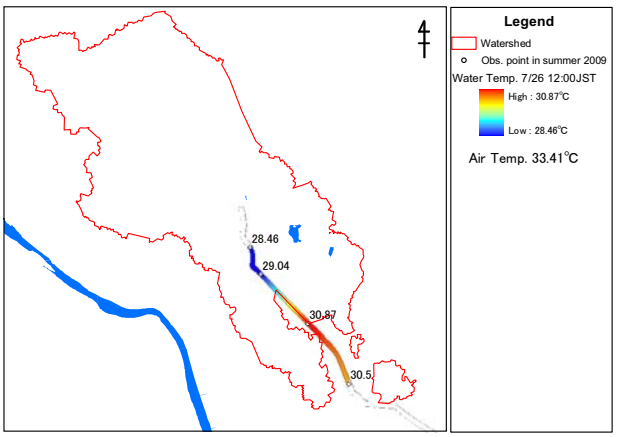

Fig.10 Spatial temperature variations of water in the River

3. Application

3.1 Target Watershed

Nomikawa Riverbasin (**Fig.2**) is the target watershed for the research. It is in Setagaya, Meguro and Ota wards (**Fig.3**). The riverbasin is inhabited by 370,000 people and is highly urbanized with a basin area of 17 km^2 (**Fig.4**). The head water of Nomikawa River was lost and treated sewage water flows from Kodaibashi through a concrete ditch. When it rains, sewage water overflows into the river causing flash floods. As a result, a fatal accident occurred 2 years ago. The water cycle in the watershed is completely artificial. Therefore, it is appropriate to study the regeneration of the water cycle and the environment.

Nomikawa-no-kai, a citizen's organization, works actively for the improvement of the river environment and its ecosystem.

3.2 Static Karte

Static Karte was established with the cooperation of nine organizations (**Fig.1**). Approximately 50 maps were generated. Among the nine organizations were the Nomikawa-no-kai, River Museum, Folk Museum of Ota City and Tokyo University of Marine Science and Technology (TUMSAT). Their assistance in the research activities through their unique information and their cooperation brought great progress in the creation of Karte.

Fig.5 shows the location of past springs and washing places. This information was bought by Nomikawa-no-kai and Folk Museum of Ota City. This map is highly valued because it shows how the water cycle of the watershed was in the past.

Fig.6 is the map of waterfowls in the river at winter season from 2008-2009. This map is based on one of five materials which were acquired from the continuous investigation of Tokyo University of Marine Science and Technology (TUMSAT). Other materials were also compiled in Static Karte. However, a seasonal database of town development which includes ecological investigations does not exist. Although the number of maps related to ecological system is small, Environmental Karte provides new ways to grasp the residential environment.

Fig.7 comes from the information of location of infiltration pavements. This kind of information is rarely updated even despite its importance to realizing current state of water cycle and attitude of government, and to considering a future plan. Inspite of this, Environmental Karte could consolidate such official information through its framework of cooperation. This is one of the advantages of this study.

Fig.8 shows vegetation ratio in the watershed. This map is the result of NDVI analysis using high resolution satellite image, QuickBird. This map is useful to investigate a green plan.

Fig.9 shows the river bank vegetation.

Some additional measurements were also conducted in this research. The measurement of air temperature, which revealed the spatial distribution in summer, was done in the center of the water shed.

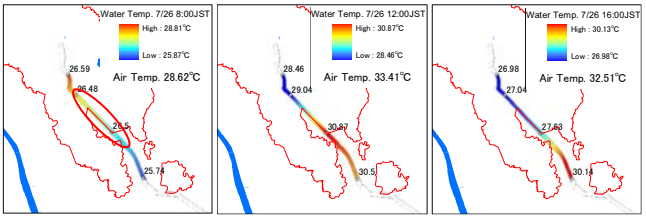

Fig.11 spatial and temporal temperature variations of water (left:8:00 a.m., center: 12:00, right: 14:00 p.m. on Jul. 26th, 2007)

Temporal and spatial variations of water temperature were measured for a year in the river. The result indicates that the temperature in downstream of Nomikawa River reaches 32 degree Celsius during summer (**Fig.10**). Time series of the spatial temperature variations (**Fig.11**) suggest that water mass is warmed up in the linear part of the river surrounded by a red circle as shown in **Fig11**. Comparing these maps to **Fig.9** discloses the cause of warming. Little vegetation lies along the river and the river flows from north-west to south-east. This river flow direction shows that sunshine has fully stuck the riverbed by noon. As a result, the riverbed and river wall warm up enough to warm the water body as well. Furthermore, its relatively small depth of water accelerates the warming process.

Static Karte was initiated and is now being used for diagnostics by superimposing it with other maps, as shown above, and is used as input data for WEP model.

3.3 Dynamic Karte

Water and Energy transfer Process (WEP) model which is a physically based spatially distributed hydrological model was introduced into Environmental Karte. This dynamic part of Environmental Karte enables users to understand the actual state of water cycle and assess future scenarios.

In order to simulate the water cycle in the watershed more accurately, WEP model was improved in two ways, namely:

(1) temporal input resolution from 60 minutes (WEP60_Co) to 10 minutes (WEP10_Co) through WEP program modification.

(2) spatial resolution of precipitation input. Precipitation was given in 250m mesh by the Tokyo Amesh radar precipitation data (WEP10_Am) where the data was distributed, originally using Thiessen method (**Fig.12**).

The simulated result of flood discharge was compared with the observed discharge at Kodaibashi, the starting point of Nomikawa river

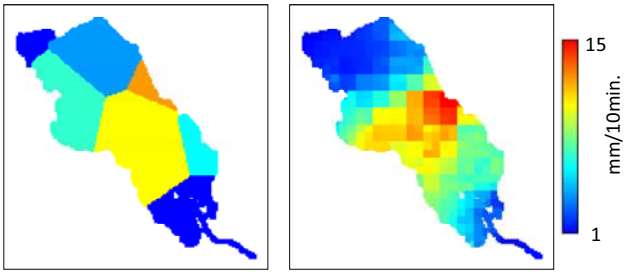

Fig.12 Difference in the spatial pattern of precipitation (Left: Thiessen method, Right: Tokyo Amesh)

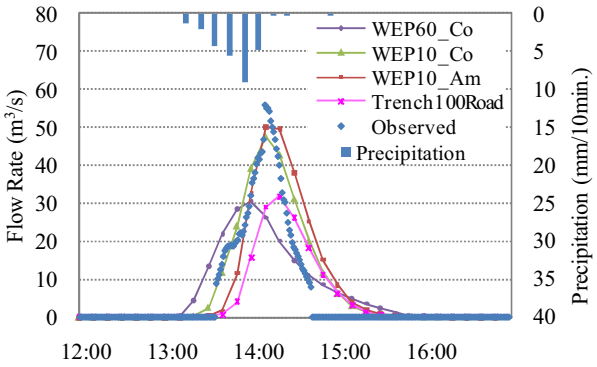

Fig.13 Comparison of simulated discharges with obsevered

(**Fig.13**). It is obvious that the simulated flood of WEP10_Co reproduced a better hydrograph than the WEP60_Co. However, there was no improvement on the hydrographs of WEP10_Am based on its comparison with the WEP10_Co hydrographs. This is mainly because few distinct differences are seen between the precipitation patterns given by Tokyo Amesh and by the Thiessen method. Even though the patterns were different, as shown in **Fig.12**, temporal resolution was too large to simulate flood discharges with a 250m of spatial resolution data. Assuming a 2m/s of runoff, the flow reached 1200m in 10 minutes. This means 250m of spatial resolution is meaningless in current settings. Though WEP10_Am showed no improvement, WEP10_Am and WEP10_Co reproduced rapid increase of flow rate of observed flood discharge well, which is the most important phenomena to study accident prevention in urban rivers.

A future scenario was also simulated. Infiltration trenches and water retentive pavements were assumed to be installed in all buildings and on all impervious surfaces, respectively (Trench100Road). Maximum flow rate becomes 64% of that of WEP10_Am. The time of maximum flow rate was delayed. This was the first simulation which assessed the impact of a flood control in the basin. The result of the simulation was used in a workshop.

3.4 Application

The Karte was used and in three ways. First the Karte is available on the web site and users can download them (http://www.ide.titech.ac.jp/~kandalab/ja/project/nomikawa/). Secondly, the Karte was used in classes of Tokyo Institute of Technology (Tokyo Tech.) and Kugahara elementary school. In the practice lecture of Tokyo Tech., the lecture did not only introduce Karte but improve its database from the results of its application by the participants. Thirdly, the Karte was used seven times in workshops (**Table 1**). The map of vegetation ratio and other maps were used in the regular meeting of Nomikawa-Network, the superior organization of Nomikawa-no-kai with an objective to provide a green plan in the watershed.

The future scenario was used during the regular meeting of Nomikawa-no-kai held on Dec. 12th, 2009. Measures to reduce the amount of sewage discharges were discussed in the meeting.

Lastly, the spatial and temporal temperature variations of water in Static Karte provided river assessments for Nomikawa renovations. In the watershed, it is useful in the heated discussion among Nomikawa-no-kai, Tokyo metropolitan government and Ota ward for the on-going river renovation..

4. Conclusions

The conclusions of this study are as follows:

1) Environmantal Karte was proposed as a tool for regional cooperation for town development within a watershed.
2) The Karte was developed in Nomikawa watershed.

5. References

[1] Sadohara, S., Kawasaki, A. and Yoshida, S.: Spatia; Information Platform of Water for Environmental Risk Management using GIS, a working papers of Environmental Risk Management for Bio/Eco-Systems, The 21st Century COE Program, pp.171-180, 2006.

[2] Baumueller J., Reuter U., Hoffmann U., Esswein H. : Klimaatlas Region Stuttgart, Schriftenreihe Verband Region Stuttgart, ed.: Verband Region Stuttgart, Nr. 26, 2008.

[3] Jia, Y., Ni, G., Kawahara, Y. and suetsugi, T.: Development of WEP model and its application to an urban watershed, *Hydrological Processes*, Vol.15, No.11, pp.2175-2194, 2001.

[4] Geographical Survey Institute: Digital Map 5m Grid (Elevation), 2003.

[5] Geographical Survey Institute: Digital Map 2500 (Spatial Data Framework), 2003.

[6] Geographical Survey Institute: Detailed Digital Information (10m Grid Land Use), 1998.

[7] Education board of Ota city: Articles for everyday use of Ota city (water and life), The book of the cultural property of Ota city, vol.21, 1985.

Table 1 Application in workshops

Date	Name	Content
21-Feb-09	Meguro Eco Festa	Intruduction & Share
27-Jun-09	Nomikawa symposium	Intruduction & Share
13-Jul-09	Board meeting of Nomikawa-no-kai	Intruduction, Share & Feedback
19-Aug-09	Regular meeting of Nomikawa-no-kai	Share & Discussion
2-Dec-09	Eco-Walking	Share & Discussion
12-Dec-09	Regular meeting of Nomikawa-no-kai	Share & Discussion about the impact of Seepage facilities
14-Jan-10	Regukar meeting of Nomikawa Network	Share & Discussion about Green cover

MECHANISMS OF URBAN EFFECTS ON LOCALIZED HEAVY RAIN IN TOKYO USING NUMERICAL SIMULATION

Student Number: 08M18097 Name: Ryo SHIMOJU Supervisor : Manabu KANDA

気象モデルを用いた都市型集中豪雨の発生メカニズムに関する研究

下重　亮

本研究では首都圏で夏季に発生する局地的集中豪雨への都市影響を評価し，発生メカニズムを明らかにする事を目的に，気象モデルを用いて解析を行った．その結果以下の事が明らかになった．①都市型集中豪雨の発生に都市幾何形状が大きく影響する．②都市は海風前線上に孤立的に発生する積乱雲のみでなく，内陸の熱や水蒸気の分布にも影響を与える事で，首都域での集中豪雨に繋がる積乱雲を発生させやすい大気場を形成する．③都市の熱と都市幾何形状は積乱雲通過時の降水系にも影響を与え，それぞれ降水量を増加させる．

1. Introduction

Localized heavy rainfall in summer has attracted attention in recent years. Rainfall sometimes reaches more than 20-50 mm per hour and this can cause urban floods. These localized rainfalls are still difficult to predict. Urbanization is suspected to be one of the key factors that generate localized heavy rainfall. However, this has not been clarified. To investigate the urban effect on rainfall, implementation of various urban parameters to a weather forecast model is needed. Recently, urban canopy model (UCM) and Anthropogenic heat and vapor (AH・AWV) have been developed for integration in weather prediction models. Yet, urban geometry has not been included in these models. Modification of the displacement height by the urban geometry is considered in this study. Displacement height was calculated from detailed building information of Tokyo and thus represents the "bulk building landscape". Detailed displacement height was added to the original terrain map to further define the boundary conditions of the weather prediction model.

Firstly, localized heavy rainfall days were extracted and statistically investigated, and the displacement heights for Tokyo were calculated.

Secondly, three simulations of a typical sea breeze day were executed with the following settings (Table 1): RUN1 includes UCM, AH・AWV and the displacement height map; RUN2 considers only UCM and AH・AWV; while RUN3 does not include any of the above-mentioned models that the previous 2 simulations use.

Thirdly, 16 occurrences of one-day localized heavy rainfall occurring between 2005 and 2008 were simulated, using an urban and a non-urban cases for simulation. By comparing the results of these two case simulations, various mechanisms of localized heavy rainfall affected by urbanization were analyzed.

Table 1 Numerical Settings for the 3 runs

	Displacement height	UCM	AH・AWV
RUN1	○	○	○
RUN2	×	○	○
RUN3	×	×	×

Finally, how rainfall changes when rainfall cell goes over an urban area was investigated.

2. Statistics on anomaly of heavy rainfall

Ensemble-averaged rainfall was examined to detect any anomaly of heavy rainfall and its relationship with the urban landscape. Historical localized heavy rain days were extracted from rainfall data of the Tokyo Construction Bureau River Department, including six summer periods (July - September) of 2000-2006. The following are the conditions set for rainfall data extraction (Fujibe et al. [1], Nakanishi et al. [2]) :

1) Maximum daily temperature is above 30° C.
2) The day when rain starts anytime from 12:00 to 21:00 and ends before 24:00.
3) 1-hour rainfall is more than 15 mm.
4) The rainfall events under the influence of the synoptic weather were discarded.

Rainfall for each point were summed up and averaged. Spatial deviation from corresponding averages were plotted to see the spatial anomaly of rainfall (Figure 1). Wards A, B and C in Figure 1, which are on the north-west side of high rise buildings in Shinjuku (D in Figure 1), had more than 40% rainfall than other wards. The general sea breeze in this area is a north-west one coming from Tokyo Bay, crossing Shinjuku, making these three towns to be downstream of Shinjuku. This result implies high-rise buildings enhance rainfall cell in downstream regions.

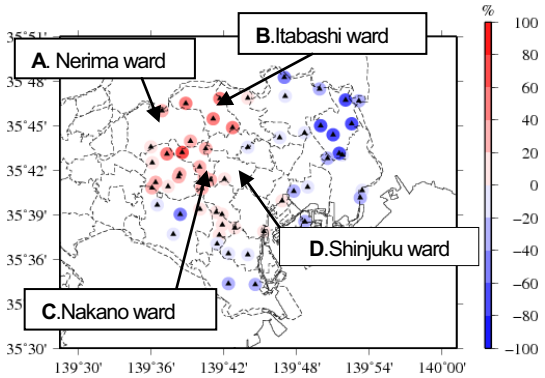

fig.1 Anomaly of rainfall in 23 wards

3. Dataset of urban displacement height

Urban geometry can be represented by displacement height. Displacement height of Tokyo was calculated by using the following equation (MacDonald et al.[3]):

$$d = H(1 + 4.43^{-\lambda_p}(\lambda_p - 1)) \qquad (1)$$

where H is the average building height and λp is building-to-land ratio. To calculate these parameters, information of floor space, number of stories and building use type were used. Figure 2 shows the calculated displacement heights for Central Tokyo. Almost the whole area is elevated more than 2m. Large city areas E, F and G in Figure 2 are especially elevated at 12 - 26m. These areas have many closely packed high-rise buildings. From Figure 3, which presents the sum of the displacement height and terrain height, the height around Shinjuku (H in Figure 3) is more than 40 m. The altitude within a 3-km radius of Central Shinjuku looks like an isolated mountain.

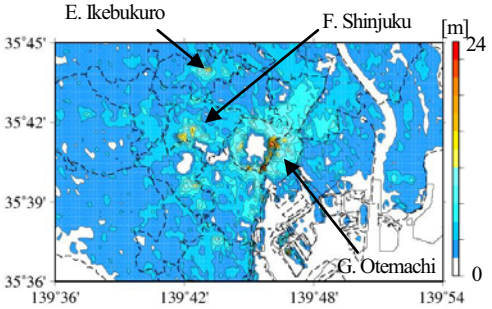

fig.2 Distribution of displacement height of Central Tokyo

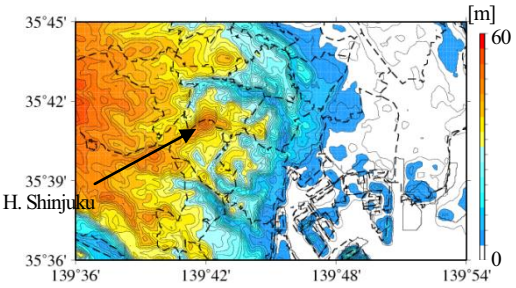

fig.3 Sum of displacement height and terrain height

4. Numerical analysis

To evaluate how urbanization affects localized heavy rain, Weather Research & Forecasting Model (WRF) was used.

4. 1 Urban effect on sea breeze from Tokyo Bay

August 10, 2004 was used for analysis. This day is typical sea breeze day and localized heavy rain occurred around Shinjuku. The 3 simulations previously mentioned were run.

A conspicuous difference for the wind and temperature field is seen between RUN1 and RUN3. Figure 4 shows wind at 10 m and temperature at 2 m at 12:00. In RUN1, sea breeze penetration was delayed. Also, the sea breeze, which contains AH of Central Tokyo, changes direction and blows towards Nerima (encircled in white in Figure 4). This is due to the drag caused by urban geometry and thermals. This results in a higher temperature for the north-west side of the 23 Wards of Tokyo for RUN1 with respect to RUN3.

If there is no urban area, the sea breeze and water vapor will quickly move inland.

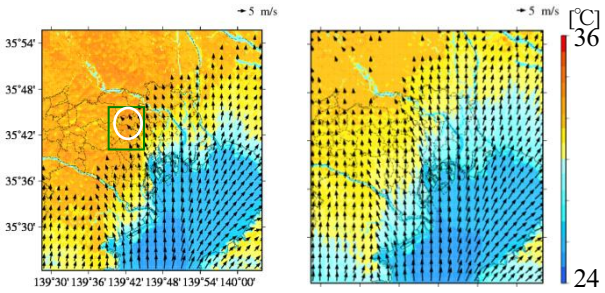

fig.4 2 m temperature and 10 m wind field at 12:00 (left:RUN1, right:RUN3)

On the other hand, the difference between RUN1 and RUN2 is most obvious at the time sea breeze goes through Shinjuku (Figure 5). A change in wind direction creates a convergence zone only for RUN1 (encircled in white in Figure 5). At the same time, a strong updraft (6m/s) and cumulus were analyzed corresponding to this area. This results show urban geometry clearly affects the generation of localized heavy rainfall.

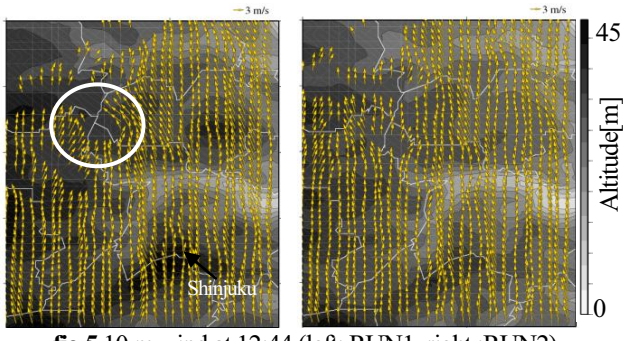

fig.5 10 m wind at 12:44 (left: RUN1, right :RUN2) Domain is green square in fig.4

4.2 Case analysis of localized heavy rain

To extract various mechanisms of urban effect on localized heavy rainfall, a total of 16 localized heavy rain events were numerically investigated. Two cases were considered, the urban case, which considers UCM, AH・AE and displacement height, and the non-urban case (Table 2). The urban effect was seen in 9 rainfall events. Moreover, the mechanisms of urban effect were classified into 3 types. Following section shows examples of each type.

Table 2 Numerical Settings for Case Analysis

	Displacement height	UCM	AH・AWV
Urban	○	○	○
No urban	×	×	×

4.2.1 Urban effects on Kanto scale (Rainfall cell develops in inland)

Rainfall at the Kanto region at 13:00 16th August 2008 is shown in Figure 6. The rain band moved from mountain area to the east side. The Rainfall cell developed and heavy rain was resolved at Central Tokyo only in urban run.

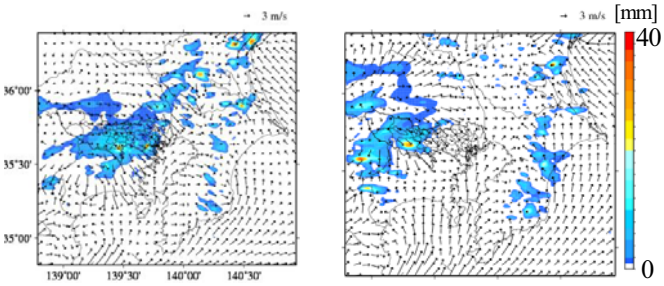

fig.6 Rainfall in 30min. at 13:00 (left: Urban, right: No urban)

In the previous day, the sea breeze for non-urban run penetrates more than the urban run (Encircled in green in Figure 7). Sea breeze advected water vapor and makes inland atmosphere unstable. The Rainfall cell in the non-urban run was more developed than that for the urban run. As a result, dry and cool outflow of rainfall cell sweeps wet air out of the Kanto Plain for the non-urban run. On the other hand, in urban run, wet and hot air remains near Central Tokyo at night and was advected toward mountain area at dawn by valley wind (Figure 8). Therefore, atmosphere of mountain area was unstable in the morning of the 16th August 2008.

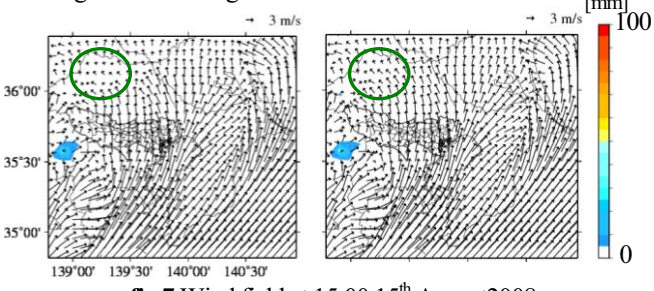

fig.7 Wind field at 15:00 15th August2008
(left: urban, right:No urban)

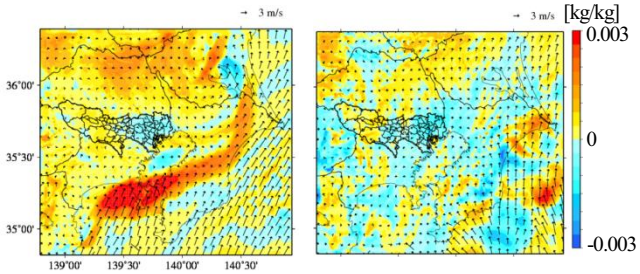

fig.8 Difference (urban – no urban) of 2 m water mixing ratio (left:1:00, right:8:00 16th August)
Vector represents wind of urban run

4.2.2 Urban effect on local scale (Rainfall cell develops on sea breeze front)

Rainfall at 11:14 29th July 2008 is shown in Figure 9. Sea breeze from Tokyo Bay was analyzed. Rainfall at the sea breeze front was resolved only in the urban run (encircled in green in Figure 9). Before sea breeze penetration, the temperature of Central Tokyo is higher for the urban run relative to the non-urban run. Urban heat effect enhances the updraft at the sea breeze front, as simulated by Yoshikado (1992). The results of this study suggest that the sea breeze from Tokyo Bay generates isolated Rainfall cell in Central Tokyo as an effect of urban heat.

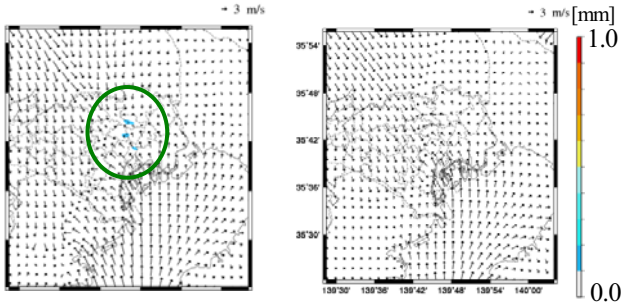

fig.9 Rainfall in 2 min. at 11:14
(left : Urban, right : no urban)

4.2.3 Urban effect on both Kanto and local scale

Both Kanto and local scale effects were seen at 4th August 2008. Mid morning rainfall at the sea breeze was analyzed in the urban run (not shown). At the same time, Rainfall cell developed at mountain area (encircled with green in Figure 10). Before Rainfall cell in mountain area was formed, a convergence zone developed for the urban run only (encircled in red in Figure 11). When atmosphere over the Kanto Region is stable, the sea breeze and valley wind converge. The Kanto Plain was completely covered with the southerly wind (extended sea breeze) during the daytime. In theory, this extended sea breeze becomes weak as the night comes. But for the urban run, the thermal low due to the heat island leaves a strong extended sea breeze in the night. As a result, convergence can be formed easily between the extended sea-

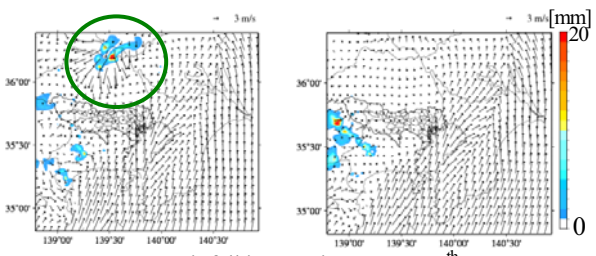

fig.10 Rainfall in 30 min. at 10:30 4th August
(left: urban, right: No urban)

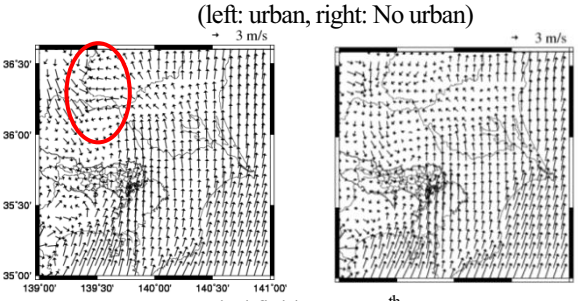

fig.11 Wind field at 5:00 4th August
(left : urban, right : no urban)

breeze and the outflow of rainfall cell generated at the mountain area.

The Kanto and Kanto + local scale effects on rainfall are manifested in seven out the nine cases (78%).

4.3 Development of rainfall cell going over urban area

When Rainfall cell goes over an urban area, how each urban factor affects rainfall was investigated. Weather data when rainfall cell develops at mountain area was used for each runs as initial condition. Settings are shown in Table 3.

Table 3 Numerical settings for Rainfall cell verification runs

	Displacement height	UCM	AH・AWV
RUN1(CNTL)	○	○	○
RUN2	○	×	×
RUN3	×	×	×

Difference of total rainfall from 12:00 to 14:30 is shown in Figure 12. The UCM and AH・AWV increase rainfall 50 mm (100%) or more above Central Tokyo. On the other hand, the displacement height increases about 6 mm (20%) at the leeward of Shinjuku.

To clarify the relationship of displacement height and rainfall, additional experiment was done. The distribution of displacement height was modified (not shown). Table 4 shows the average and variance of the altitude for each run. Results show that the average and variance of altitude are proportional to the amount of rainfall (Table 5). Moreover, they are closely connected to the locality of heavy rainfall (not shown).

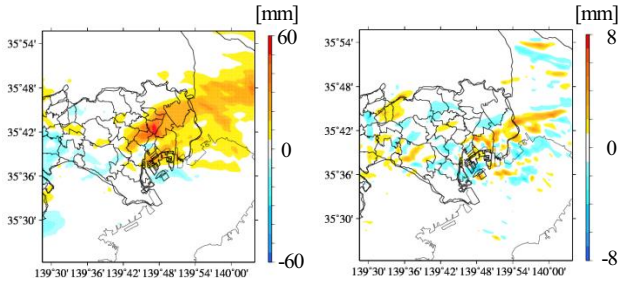

fig. 12 Difference of total rainfall from 12:00 to 14:30
(left: RUN1-RUN2, right : RUN2-RUN3)

Table 4 Average altitude and variance of height of each run

	Average altitude (m)	Variance of height
RUN1(CNTL)	19.22	297.39
RUN2	19.08	289.73
RUN3	19.34	300.82
RUN4	20.03	327.41

Table 5 Ratio of total precipitation of Tokyo 23 wards

RUN2/CNTL	RUN3/CNTL	RUN4/CNTL
0.99	1.00	1.02

5. Conclusion

The conclusions of this study were summarized as follows:

1. New simple method to reflect urban geometry to a weather forecast model was devised. Urban geometry can trigger the break out of localized heavy rainfall in Tokyo.
2. When localized heavy rainfall occurs, urbanization, specifically by drag due to urban geometry and heat, affects the Kanto scale weather more than the local scale.
3. When Rainfall cell goes over an urban area, it can develop and increase the rainfall at least 100%, mainly by urban heat. Although the effect of geometry can increase rainfall by about 20%, the average and variance of displacement height are proportional to the amount of rainfall and have a relationship with rainfall distribution.

References

[1] Fujibe,F.,Sakagami,K.,Chubachi,K.,Yamashita,K.,:Surface wind patterns preceding short-time heavy rainfall in Tokyo in the afternoon of midsummer days,Tenki,49,395-405,2002

[2] Nakanishi,M., Hara,Y.,:Characteristics of local winds associated with the intensification of short time rainfall in the Tokyo urban area in the afternoon of summer days,Tenki,50,91-102,2003.

[3] Macdonald, R.W., Griffiths, R.F., and Hall, D.J., 1998. An improved method for the estimation of surface roughness of obstacle arrays, *Atmos. Environ.*, Vol. 32, pp.1857-1864.

[4] Yoshikado, H., : Numerical study of the daytime urban effect and its interaction with the sea breeze. J.Appl. Meteor., 31, 1146-1164,1992.

Study of propagation channel for wireless sensor network in the vicinity of human body

Student Number: 08M18105 Name: Yuuki TERAO Supervisor: Jun-ichi TAKADA

人体近傍の無線センサネットワークにおける伝搬チャネルに関する研究

寺尾 優輝

近年，人体上での無線通信への関心が高く，医療，ヘルスケアのみならずエンターテイメントとしての需要も高まっている．コンピュータネットワークに関する国際標準化機関である IEEE（米国電気電子技術者協会）802 標準化委員会の下に設置された 802.15.6 タスクグループ (TG) では現在，医療およびヘルスケアを主用途としたボディエリアネットワークの標準化が進められている．伝搬チャネルモデルは，無線通信方式の標準化プロセスの中で最初に規定する必要があり，同 TG においても BAN 標準チャネルを 2008 年 11 月に制定している．しかしながら，このチャネルモデルでは人体がチャネル特性に与えるメカニズムは考慮されておらず，使用するアンテナや被験者の影響を含んでいる．本研究では伝搬チャネル特性からアンテナの影響を切り分けるために人体による受信レベル変動のメカニズムを究明する事を目的として，主に人体にアンテナを装着することによって生じるインピーダンス不整合， アンテナ放射パターンの変化などについて考察する．

1 Introduction

A growing interest in the body centric wireless communication technology has been taken in various applications including medical, health care and consumer electric industry for entertainment and wearable technology for fashion as well as space and military applications, the body area network (BAN) has become more important to connect devices around the human body. Currently, IEEE 802.15.6 task group on wireless body area networks is discussing the standardization of body area network mainly for medical and health care applications[1]. Among a few categories of BAN, this research focuses on the channel between body surface and body surface. Firstly, path loss model should be established among the standardized process in wireless communication standards, which was established on November 2008 in TG. However, in existing path loss model, the antenna effects are treated as a part of the channel, because it is difficult to separate these effects from the measured channel responses in BAN. The problem is that the channel models depend on the antenna and individual test subjects. In these models, there is no reproducibility when the antenna and the test subject are different, and consequently the link budget prediction will be difficult. Therefore, more generalized channel model channel model is necessary.

This research to de-embed the antenna effects from human body focuses on investigating the mechanism of variation of the received signal level due to human body, and studies changes of impedance matching and radiation pattern of antenna due to proximity to human body surface.

2 Path Loss Model

In order to develop the BAN channel model, the propagation characteristics are represented by path loss. Measurements were conducted in an office environment. The frequencies of 444.5 MHz for wireless medical telemetric service (WMTS) in Japan, 611 MHz for WMTS in US, and 953 MHz for active RFID in Japan were chosen among the candidate frequencies in IEEE 802.15.6. A vector network analyzer (VNA) was used to measure path loss and two test subjects were employed for this measurement. The specifications are shown in Fig.1. From measured data, the path loss model was obtained from two test subject data. And I drew an approximation plane to compare with the measured data as follows.

$$PL(d, f) = \alpha \cdot \log_{10}(d) + \beta \cdot \log_{10}(f) + \gamma \qquad (1)$$

To obtain the coefficients α, β, and γ of the approximation plane of Eq.(1), LMS algorithm was used. The obtained values for α, β, and γ are 14.71, 3.96, and 2.92 respectively. When antennas are attached on human body surface, there are some mutual interactions between body and antennas, i.e. distance variability by the body movement, distortion of antenna radiation pattern due to proximity to human body, polarization rotation by the human body motion, propagation loss due to the absorption, impedance mismatch of the antenna. So far, it has been considered that separating antenna effects from the measured channel responses in BAN is very difficult. Therefore, the antenna effects are generally treated as parts of the radio channel. In this path loss model which was obtained in this time, the model only focused on distance variation between Tx and Rx antennas. Therefore, all the factors have been mixed up. The problem is that this channel models depend on the antenna effects and individual differences of test subjects. The changes of radiation pattern and reflection coefficient of antenna were investigated to examine the antenna effect from this model, when the antenna was attached to human bodies.

3 Antenna Radiation Pattern

3.1 Measurement Equipments

The measurement was conducted in radio anechoic chamber to remove the environment effects. The setup consisted of VNA, transmitting and receiving antennas,

Table 1: Measurement specifications

Parameters	Values
VNA	Model: 8720ES (zero span mode)
Number of points	801
IF bandwidth	300Hz
Tx Antenna position	navel (fixed)
Rx Antenna position	10 positions on body
Frequency	444.5, 611, 953 MHz
Test subjects	2 persons

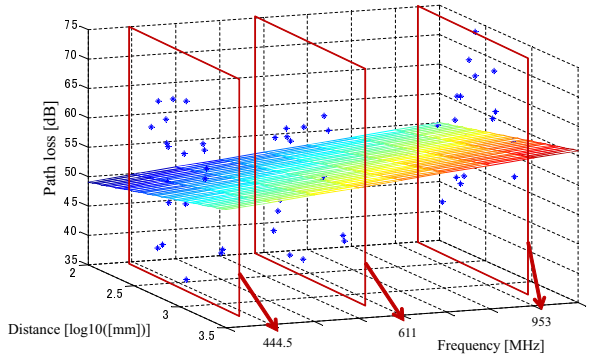

Figure 1: Path loss model

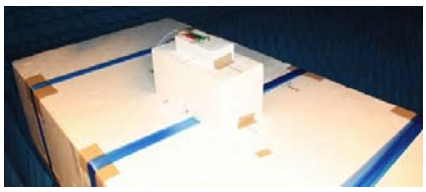

(a) Free-space measurement

(b) On-body measurement

Figure 2: measuremant

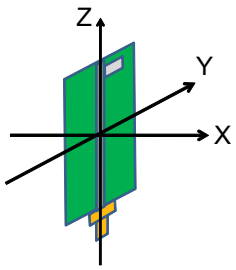

Figure 3: Coordinates for chip antenna

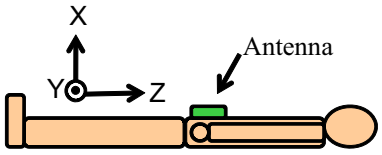

Figure 4: Coordinates for body and antenna

antenna rotator, personal computer to control and to synchronize the VNA and rotator, and to record the measurement data output. The antenna pattern measurement was conducted on body in lay-down position. The receiving antenna is a standard dipole antenna, while the antennas under-test are three surface mountable dielectric chip antennas operating at for 444.5 MHz, 611 MHz, and 953 MHz, which were set in the transmitter side[4]. In order to aboid the influence from rotator, I utilized polystyrene form (100cm × 200cm × 50cm). The effect of body to the antenna pattern was investigated by comparing the antenna without spacer (0 mm) and with 15 mm spacer. In order to make a space between antenna and human body, polystyrene foam, which is with very low permittivity of 1.03–1.05, was used as a spacer. To increase the validity of measurement data, the antenna patterns for free-space and on-body of two male subjects are observed. The effect of body to the antenna pattern was investigated by attaching the antenna in two positions namely as YZ-plane as shown in Fig.2. Co-polarization and cross-polarization patterns were measured in each of the planes.

3.2 Results

Antenna and human body coordinate are shown in Fig.3 and Fig.4 respectively. Figures 5 are radiation pattern of YZ-plane. As a general trend, it was assessed that on-body pattern without spacer has a smaller gain compared to free-space possibly due to the absorption of human body. while, the antenna gain of on-body pattern was almost the same of free space pattern when antenna was separated by a 15 mm spacer.

Antenna patterns for two subjects as well as in free space at 611 MHz in Fig.6. When antenna was directly attached on human body surface without spacer, a perceivable difference of patterns was found by comparing S1 and S2 results. The difference of ripple comes from individual breathing period. In this case, one measurement took 207 seconds. However, by using 15 mm spacer, it was effective to replicate the antenna radiation pattern, which does not depend on test subjects. Moreover, in comparison with 0 mm case, it is possible to say the pattern differences tend to vanish and become homogeneous. Therefore, it would be an useful information in case of practical system designing.

4 Impedance Matching

To investigate the influence of human body to antenna matching, dipole and chip antennas were used for this measurement. Human body and antenna coordinate are shown in Fig.7. In this measurement, the frequencies of 444.5, 611 and 953 MHz were used, and two test

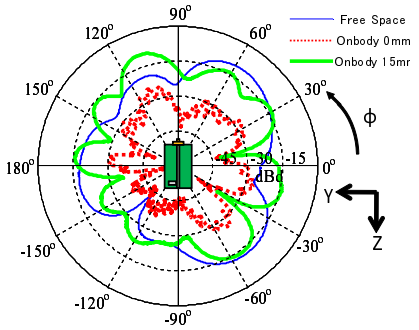

(a) 444.5 MHz x-polarization

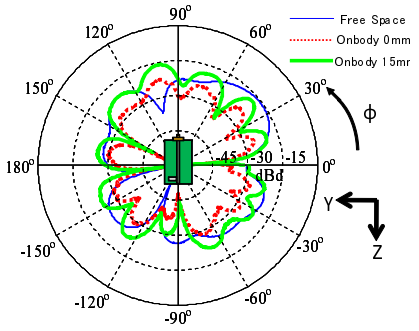

(b) 611 MHz x-polarization

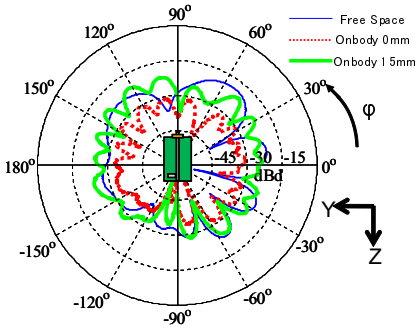

(c) 953 MHz x-polarization

Figure 5: Antenna radiation patterns at different frequencies

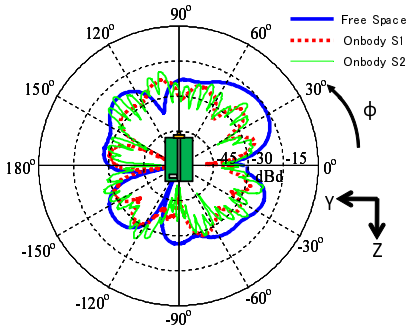

(a) Spacer thickness 0 mm

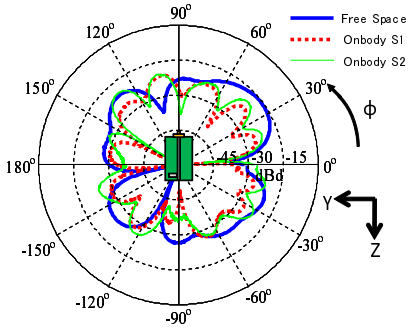

(b) Spacer thickness 15 mm

Figure 6: Comparison of antenna radiation patterns for different samples at 611 MHz

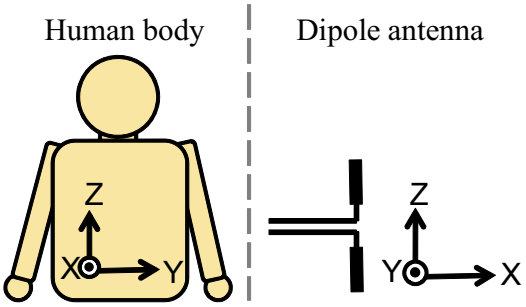

Figure 7: Coordinates for body and dipole antenna

subjects were examined for this measurement. The antenna was fixed on navel with styrene foam and tripod stand, which is shown in Fig.8. The measured reflection coefficients using dipole and chip antenna are shown in Fig.9 (a) and (b) respectively. The influence to impedance matching has been almost completely ignored when the antenna is separated by using 15mm spacer from the human body surface.

4.1 Frequency characteristics of reflection coefficient

Frequency characteristics around the center frequency were investigated to obtain the variation mechanism of reflection coefficients. Frequency characteristics of the reflection for dipole antenna and chip antenna are shown in Fig.10 (a) and (b), respectively. In the Fig.10 he resonant frequency was enormously shifted from free-space, when antenna was attached without spacer. The frequency shift for dipole antenna is more obvious as the effective wavelength changes due to the human body, while the resonant frequency of chip antenna is dominated by the internal structure and less influenced by the human body. When antenna was separated in 15 mm from human body surface change of reflection characteristics is negligibly small. It would be useful information in practical system design.

Figure 8: Measurement setup

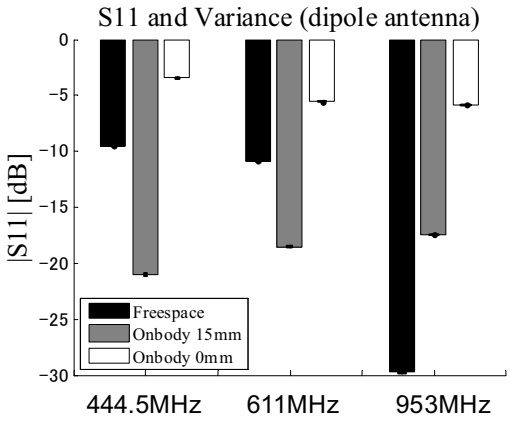

(a) Dipole antenna

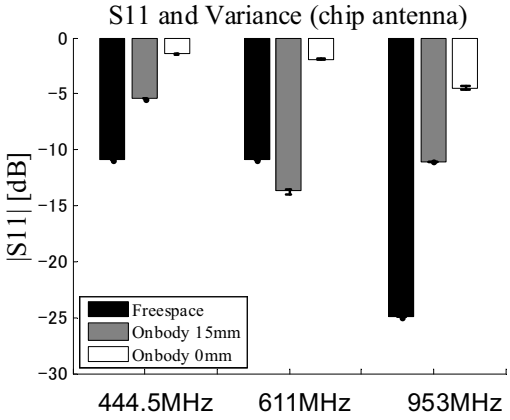

(b) Chip antenna

Figure 9: Reflection coefficient

5 Conclusions

In this study, the changes of antenna radiation pattern and reflection coefficient were investigated on navel for de-embedding the antenna effects from human body in BAN. The reflection property was almost unchanged when the antenna was separated 15 mm from the body surface. Moreover, using 15 mm spacer was effective to replicate the antenna gain which does not depend on test subjects. Although it was found that these results coincide with those for the mobile phones, they still provide useful information for BAN system/device design.

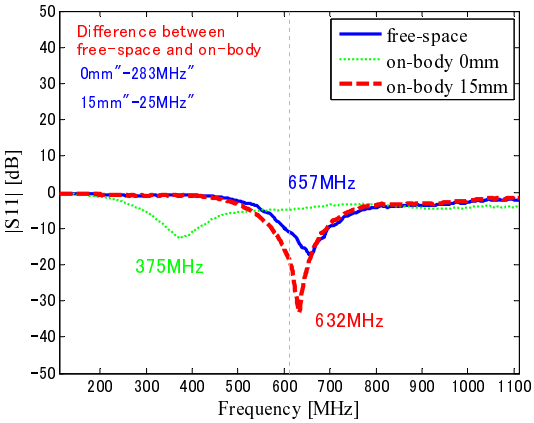

(a) Dipole antenna (Test subject 1)

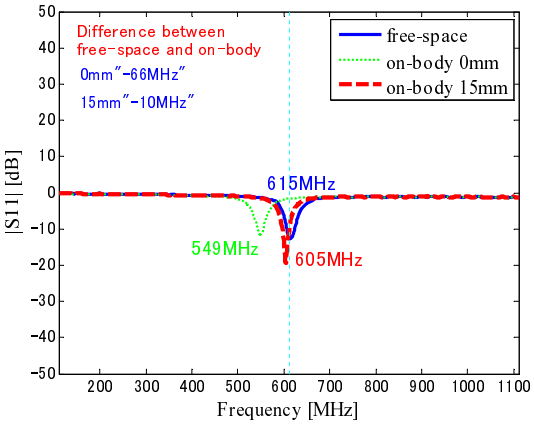

(b) Chip antenna (Test subject 1)

Figure 10: Frequency characteristics of reflection coefficient for 611 MHz configuration

References

[1] "Body area networks," http://www.ieee.org/15/pub/TG6.html

[2] K. Yazdandoost, and K. Sayrafian-Pour,"Channel Model for Body Area Network (BAN)," IEEE 802.15-08-0780-04, Nor. 2008.

[3] Y. Hao, et.al., "Antennas and propagation for body centric wireless communications," in Proc. IEEE/ACES 2005, pp. 586-589,

[4] "Chip antenna, Mitsubishi material," http://www.mmc.co.jp/corporate/ja/index.html

Utilization of Byproducts in the Process of Biodiesel Production from Jatropha

Student Number: 08M18134 Name: Tomoki HAYASHI Supervisor: Ryuichi EGASHIRA

ジャトロファ由来バイオディーゼル燃料製造プロセスにおける副生成物の利用

林　知輝

まず，粗ジャトロファ油を，前処理後，メタノールとエステル交換することによりバイオディーゼル燃料およびグリセリン(副生成物)を作成しこれらを分析した。粗グリセリンの収率は約 0.23 と一定値であり、理論的なグリセリンの生成量と未反応メタノールの和に等しい。グリセリン中には未反応メタノールと中間生成物であるモノオレインが含まれるため、各々濃度を測定した。ついで，油脂圧搾後のジャトロファ殻(副生成物)を熱処理し活性炭を作成した。熱処理前のジャトロファ殻の化学処理や熱処理における水蒸気雰囲気の利用などにより表面積および細孔容積は増加した。さらに，上記で得られたジャトロファ殻活性炭を用いてメタノールおよびモノオレインの不純物を含むグリセリン溶液の平衡吸着を行った。ジャトロファ殻活性炭はグリセリン中の不純物を良好に吸着した。グリセリンの精製に十分な活性炭量が得られたことを確認した。

1. Introduction

The jatropha fruit is a promising biomass especially for the biodiesel production as its kernel-oil (crude jatropha oil, CJO) is inedible and has no competition with food oils. The utilization of CJO could contribute to the concerns over the economic imbalance and destruction of ecosystem.

In transesterification glycerol is produced as byproduct. In current glycerol market high purity glycerol is required. In order to remove color and trace impurities from crude glycerol adsorbent such as activated carbon, ion exchange resins and molecular sieves are used. After jatropha seed is removed for biodiesel production, the shell approximately 40% of the fruit is remained and it may initiate the waste problem. A more viable option would be conversion of this shell waste into value added product, for example thermal treatment of shell waste to produce activated carbon.

This dissertation tried to utilize byproducts in biodiesel process. Transesterification of CJO was carried out to obtain biodiesel and glycerol and to measure composition of glycerol. Thermal decomposition of jatropha shell was conducted to obtain activated carbon. The yield and characteristics of the activated carbon were estimated. Adsorption experiment was carried out to confirm the feasibility of glycerol purification by the activated carbon from jatropha shell.

2. Transesterification of crude jatropha oil

2.1 Experimental

Feed oil

The compositions of feed oil and other plant oils are summarized in **Table 2.1**. CJO and model jatropha oil (MJO) was selected as feed oil in this study. The MJO was made of a mixture of tripalmitin (C_{16}) and triolein (C_{18}).

Feed pretreatment

Since CJO contained high amount of free fatty acid, the feed pretreatment (FP) is necessary before transesterification. FP removes phosphatide (degumming, DG), FFA (deacidification, DA), and water (drying) from feed oil. Two methods of DA were used: one was alkali neutralization (ALDA) and the other was acid esterification (ACDA). The procedure of FP was same as previous works[1-2].

Transesterification

The experimental conditions in the transesterification are summarized in **Table 2.2**. The mixture of methanol and catalyst (sodium hydroxide) were added to the pretreated oil. The transesterification is a set of simultaneous reactions and is heterogeneous during reactions. Therefore, the liquids in the reactor were well mixed by a magnetic stirrer. The pretreated oils were transesterified to fatty acid methyl ester (biodiesel) and glycerol.

Purification of biodiesel and glycerol

Biodiesel was washed by water. Crude glycerol was washed by H_3PO_4aq to remove salt (soap) then methanol was vaporized at 378K for 0.5hr.

Table 2.1 Compositions of Jatropha oil and other plant oils

Plant oil	Fatty acid composition				
	14:0	16:0	18:0	18:1	18:2
Jatropha	0	0.103	0.138	0.427	0.263
Palm	0.011	0.350	0.046	0.421	0.166
Corn	0	0.117	0.019	0.252	0.606
Cottonseed	0	0.283	0.009	0.133	0.575
Peanut	0	0.114	0.024	0.483	0.320
Rapeseed	0	0.035	0.009	0.644	0.223
Soybean	0	0.118	0.032	0.233	0.555
Sunflower	0	0.061	0.033	0.169	0.737

Table 2.2 Experimental conditions in transesterification

MeOH/oil molar ratio	[-]	6
NaOH/oil mass ratio as catalyst	[-]	0.01
Reaction temperature	[K]	333
Reaction time	[h]	1

2.2 Results and Discussion

The yield of pretreated oil in FP (Y_{PO}), the yield of each product (biodiesel and crude glycerol) in transesterification (Y_{BDF}, Y_{CG}), and overall yield of each product in whole biodiesel production ($Y_{OA.BDF}$, Y_{OACG}) were defined as,

$$Y_{PO} = \frac{M_{PO}}{M_{FO}} \quad (1) \qquad Y_i = \frac{M_i}{M_{TO}} \quad (2) \qquad Y_{OA,i} = Y_{PO} \times Y_i \quad (3)$$

Figure 2.1 shows the effect of DA method on the

yield in FP. Y_{PO} steeply decreased with $x_{FFA,0}$ in the case of ALDA, since the saponification of triglyceride was more remarkable with larger amount of NaOH used for the deacidification[2]. In the case of ACDA, Y_{PO}'s were higher than those in the case of ALDA.

The Y_{BDF} and Y_{CG} are plotted against $x_{FFA,FP}$ in **Fig.2.2**. Y_{BDF}'s were almost constant at about 1. Y_{CG} was close to 0.23, which value equaled to theoretical amount of glycerol plus unconverted methanol in transesterification in this study. The method of DA did not influence Y_{BDF} and Y_{CG}.

The overall yields in biodiesel process are shown in **Fig.2.3**. The method of DA influenced both $Y_{OA,BDF}$ and $Y_{OA,CG}$ strongly. Triglyceride loss in ALDA was larger than that in ACDA.

Table 2.3 shows the compositions of crude and purified glycerol. Unreacted alcohol and intermediate glyceride especially monoglyceride are remained in glycerol. In this study methanol and monoolein were analyzed since methanol was used in transesterification and triolein was the highest mass fraction in CJO. By alkali removal and methanol removal, amounts of salt and methanol were reduced. Mass fractions of alcohol and monoglyceride in glycerol have to be less than 0.00002 and 0.0005, respectively. More purification process such as adsorption by activated carbon is necessary.

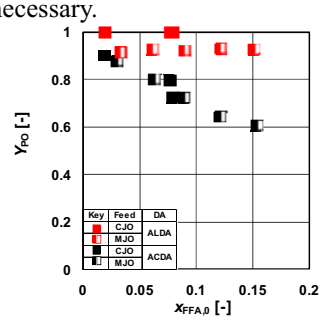

Fig.2.1 Yield of pretreated oil in deacidification

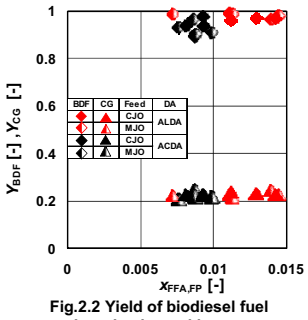

Fig.2.2 Yield of biodiesel fuel and crude glycerol in transesterification

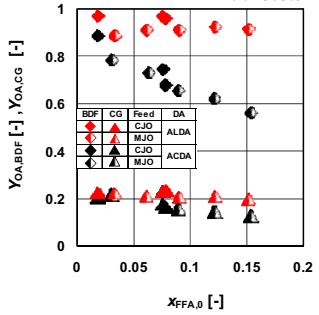

Fig.2.3 Overall yield of biodiesel fuel and crude glycerol in whole biodiesel production

Table 2.3 Compositions of glycerol

	Mass fraction [-]		
	Methanol	Monoolein	Glycerol
Crude glycerol	0.374	0.014	0.55
Purified glycereol	0.001	0.019	0.98

3. Thermal treatment of jatropha shell

3.1 Experimental

The compositions of jatropha shell and other biomasses are summarized in **Table 3.1**. In order to compare with other biomass, palm shell was also used as biomass feedstock. The jatropha shell and palm shell was washed with deionized water, dried at 378K for 24hr, crushed and sieved from 0.425 to 1.7mm. As option, the shells were impregnated in 10wt% KOH or H_3PO_4 solution for 24hr, then filtrated and dried before thermal treatment. KOH or H_3PO_4 are generally used as alkali and dehydration reagent, respectively. **Table 3.2** shows the experimental conditions in thermal treatment. The shells were thermally treated varying experimental conditions, such as thermal treatment atmosphere (nitrogen (n), steam (s)), and thermal treatment temperature. Solid products (char) from thermal treatment and commercial activated carbon (charcoal, Activated, Powder; Wako chemical) shown in **Table 3.3** were analyzed to measure BET surface area and pore volume.

Table 3.1 Chemical compositions of Jatropha shell and other biomasses

Material	Ultimate analysis [wt%]				Proximate analysis		
	C	H	N	O	Volatile	Fix-C	Ash
Jatropha shell[3]	43.13	5.53	1.33	50.01	90.26	0	9.74
Jatropha husk[4]	N/A	N/A	N/A	N/A	71.04	24.99	3.97
Palm shell[5]	47.6	5.38	0.66	41.38	72.7	23.6	3.6
Palm fiber[5]	46.64	5.66	1.73	39.46	73.7	12.6	6.6
Palm kernel[5]	41.47	5.77	3.00	43.49	80.3	10.3	3.2
Brazil nut shell[6]	50.0	5.8	0.7	43.5	76.1	22.2	3.6
Coconat shell[7]	47.00	6.06	1.02	45.92	79.9	18.2	1.9
Bagasse pitch[7]	48.96	6.77	0	44.27	86.0	10.8	3.2
Molasses[7]	59.22	7.48	0.08	33.21	75.4	20.6	4

Table 3.2 Experimental conditions in thermal treatment

Feed		Jatropha shell, Palm shell
Mass of feed	[kg]	0.03-0.04
Particle size	[×10^{-3} m]	0.425-1.7
Impregnation reagent		KOH, H_3PO_4
Temperature	[K]	423-1073
Holding time	[h]	0.5
Atmosphere		Steam, Nitrogen
Pressure	[atm]	1
Steam flow rate	[m^3/h]	0.03
Nitrogen flow rate	[m^3/h]	0.003 (Steam atm.)
		0.002 (Nitrogen atm.)

Table 3.3 Experimental conditions in thermal treatment

Run No	Feed	Pyrolysis Condition		
		Temp.[K]	Atm.	Impregnation
1	Jatropha	923	Steam	w/o
2	Jatropha	1073	Nitrogen	w/o
3	Jatropha	923	Nitrogen	KOH
4	Jatropha	923	Nitrogen	H_3PO_4
5	Jatropha	1073	Nitrogen	H_3PO_4
6	Palm	923	Steam	w/o
7	Jatropha	923	Nitrogen	w/o
8	Commercial activated carbon (CAC)			

3.2 Results and Discussion

The yield of each product in thermal treatment was expressed as,

$$Y_i = \frac{M_i}{M_{BF}} \quad (4)$$

In the case of steam atmosphere, the liquid product included steam.

The yield of solid product (Y_S) is shown in **Fig. 3.1**. The Y_S decreased with increasing the treatment

temperature due to the high consumption of the carbon. The Y_S with impregnation was higher than that of without. For the activation with H_3PO_4, the Y_S increased with temperature in the range of less than 800K. H_3PO_4 worked as dehydrogenation reagent and promoted porosity of carbon structure. For carbonization above 800K, the cross-section structure reached its thermal limit and a lot of bond cleavage was produced. With KOH impregnation, the Y_S decreased with temperature. Alkalis such as KOH were able to interact with carbon atoms and thus catalyze the dehydrogenation and oxidation reaction, leading to the suppression of tar evolution and development of porosity.

The yield of liquid product (Y_L) is shown in **Fig.3.2.** The liquid product was composed of the volatile components from biomass and the water from the feed steam. The Y_L in steam atmosphere was higher than that in nitrogen atmosphere. The Y_L decreased with temperature in the range of more than 800K. Tar were decomposed into solid and gas.

Figure 3.3 shows the yield of gaseous product (Y_G). The Y_G increased with temperature. In the case of steam atmosphere, more char and steam were reacted and more gaseous product was produced with higher temperature. The H_3PO_4 impregnation provided higher liquid yield than KOH impregnation, whereas the KOH impregnation provided high gas yield.

Figure 3.4 shows char characterization: BET surface area and pore volume. BET surface area and pore volume were higher with temperature. With impregnation, BET surface area and pore volume were much higher than those without impregnation.

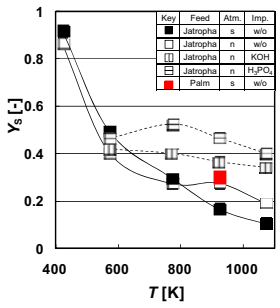

Fig.3.1 Yield of solid product in thermal treatment

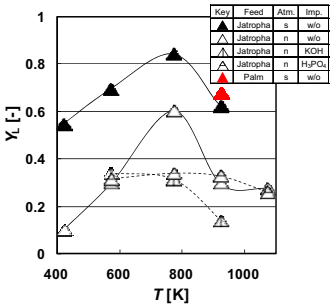

Fig.3.2 Yield of liquid product in thermal treatment

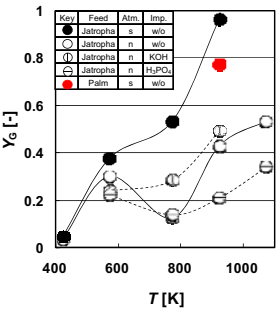

Fig.3.3 Yield of gaseous product in thermal treatment

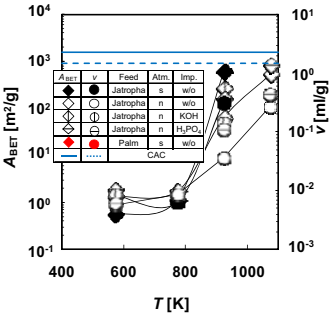

Fig.3.4 BET surface area and pore volume of char

4. Purification of glycerol using activated carbon from jatropha shell

4.1 Experimental

The char from jatropha shell, and palm shell were used as adsorbent. Also the commercial activated carbon was used to confirm whether the char could be useful as activated carbon. The experimental conditions of adsorption are summarized in **Table 4.1**. The char was mixed with various concentrations of model glycerol solution with methanol or monoolein and the mixtures were put in the shaker at 303K for 72hr enough for the adsorption equilibrium. Methanol and monoolein were selected as unconverted alcohol and intermediate glyceride in transesterification. After the adsorption experiment, the glycerol solution was separated from the char by filtration. The initial and equilibrium concentration of glycerol solution were analyzed.

I proposed an improved biodiesel process utilizing the thermal treated product and the purified glycerol as shown **Fig 4.1**. CJO of 1ton/year is provided to obtain biodiesel and purified glycerol. 2.143ton/year of jatropha shell is treated to activated carbon and used for glycerol purification[8]. The amount of adsorption in order to purify glycerol was assumed the saturated amount of adsorption.

Table 4.1 Experimental conditions of adsorption

Feed		Glycerol solution of methanol or monoolein
Mass of feed	[kg]	20×10^{-3}
Mass fraction of methanol or monoolein	[-]	1.0×10^{-4} - 1.0×10^{-1}
Adsorbent		Activated carbon from jatropha shell and palm shell Commercial activated carbon
Mass of adsorbent	[kg]	0.2×10^{-3}
Shaking amplitude	[m]	0.04
Shaking frequency	[h^{-1}]	5400
Contacting time	[h]	72
Contacting temperature	[K]	303

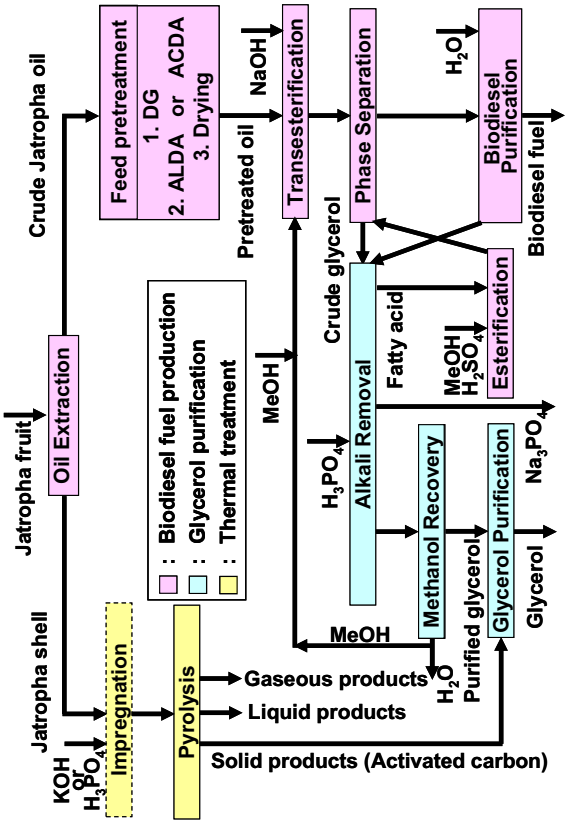

Fig.4.1 Proposal biodiesel process

4.2 Results and Discussion

The adsorption amount of each adsorbent was calculated by this material balance equation,

$$q_i = \frac{(x_0 - x_e)\, M_{sol}}{M_{AC}} \qquad (5)$$

Figure 4.2 shows the adsorption isotherms of methanol by the activated carbon. **Figure 4.3** shows the adsorption isotherms of monoolein. Lines in the figures were plotted by Langmuir isotherm equation. The amount of adsorption of each chemical increased with temperature of thermal treatment. The Langmuir isotherm equation was used to quantify the saturated amount of adsorption. Saturated amount of adsorption of each adsorbate increased with BET surface area. These relationships are shown in **Fig.4.4** and **Fig.4.5**.

The capacity of activated carbon for methanol and monoolein ($Y_{AC} \cdot q^*_i$) is plotted against the yield of methanol or monoolein in purified glycerol ($Y_{PG,i}$) in **Fig.4.6**. $Y_{PG,i}$ was mass ratio of methanol or monoolein relative to CJO. Y_{AC} was mass ratio of activated carbon relative to CJO. The diagonal line in **Fig.4.6** means that the activated carbon from jatropha shell can fully adsorb the component in glycerol. And it shows that all the plots of activated carbon are much higher than the diagonal line. Obviously the activated carbon from jatropha shell would have enough adsorption capacity for removing the yielded amount of methanol and monoolein in glycerol.

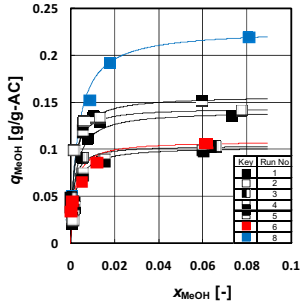

Fig.4.2 Adsorption amount of methanol

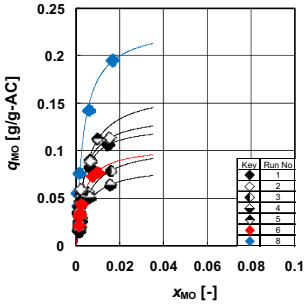

Fig.4.3 Adsorption amount of monoolein

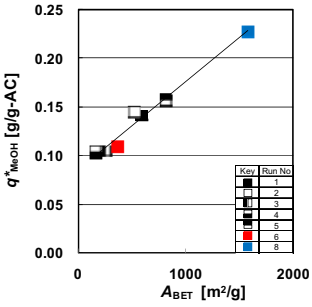

Fig.4.4 Saturated adsorption amount of methanol against BET surface area

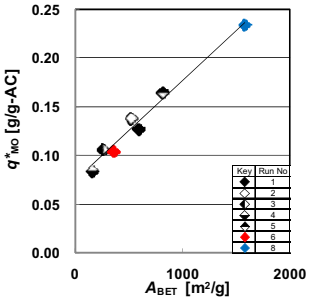

Fig.4.5 Saturated adsorption amount of monoolein against BET surface area

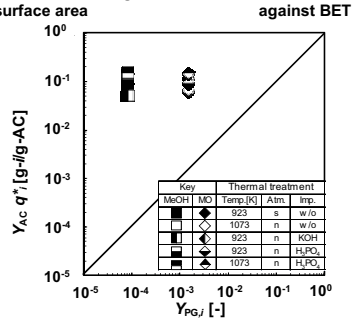

Fig.4.6 Adsorption capacity of activated carbon against yield of methanol or monoolein in glycerol

5. Conclusion

In biodiesel production yield of crude glycerol was close to 0.23. The method of deacidification influenced overall yield of products. The useful material was produced by thermal treatment of jatropha shell. Steam atmosphere and impregnation with KOH or H_3PO_4 were improved the char as activated carbon. The activated carbon from jatropha shell adsorbed impurities in crude glycerol. In overall biodiesel process there was enough amount of activated carbon from jatropha shell to purify glycerol.

Nomenclature

A	=	Surface area	[m^2/g]
M	=	Mass of material	[kg]
q	=	Amount of adsorption	[g/g-AC]
q^*	=	Saturated amount of adsorption	[g/g-AC]
T	=	Temperature in thermal treatment	[K]
x	=	Mass fraction	[–]
Y	=	Yield of product	[–]
<Greek>			
v	=	Pore volume	[ml/g]
<Subscript>			
0	=	Initial state	
AC	=	Activated carbon	
BDF	=	Biodiesel fuel	
BET	=	BET adsorption model	
BF	=	Biomass feedstock	
CG	=	Crude glycerol	
e	=	Equilibrium state	
FFA	=	Free fatty acid	
FO	=	Feed oil	
G	=	Gaseous product in thermal product	
i	=	Component i	
L	=	Liquid product in thermal product	
MeOH	=	Methanol	
MO	=	Monoolein	
OA	=	Overall biodiesel production	
PG	=	Purified glycerol	
PO	=	Pretreated oil	
S	=	Solid product in thermal product	
sol	=	Solution	
TO	=	Transesterified oil	

Literature Cited

1) Sinthupinyo P.; Master Thesis, Tokyo Tech (2007)
2) Hayashi T.; Bachelor Thesis, Tokyo Tech (2008)
3) Sinthupinyo P. *et al.*; SCEJ Sendai, C121 (2008)
4) Sardar P.; SPRERI annual report (2005-2006)
5) Luangkiattikhum P. *et al.*; *Bioresource Technology*, 99, 986-997 (2008)
6) Bonelli P. *et al.*; *Bioresource Technology*, 76, 15-22 (2001)
7) Das S. *et al.*; *Energy*, 27, 405-414 (2002)
8) Sinthupinyo P. *et al.*; *ISEEE Reyong,* 305 (2009)

Assessment of Users' Profitability and Perception of Residential Photovoltaic Systems under Failure Risk

Student Number: 08M18140 Name: Toshihiro Mukai Supervisor: Naoya ABE

故障リスクを考慮した住宅用太陽光発電システムユーザーの収益性と認識の評価

向井　登志広

住宅用太陽光発電システムには、1～2 割程度の割合で何らかの故障が生じることが明らかになっている。しかし、ユーザーに故障リスクに関する情報が適切に伝わっていない可能性があり、現状を評価・解明しないまま普及策を講じることは、将来的に消費者の不信感を不必要に引き起こす誘因となる。

そこで本研究は、故障が PV システムの収益性に与える影響を評価した上で、ユーザーの認識を意識調査により集計し、故障リスクに対する認識の違いをもたらす要因を分析した。これらの分析を通して、より長く PV システムを利用するための社会的体制の必要性を検討する。

1. Background and Objectives

To diffuse residential photovoltaic (PV) system in a society, it is necessary for the PV system users to recognize the risk of failures appropriately for adequate and sustainable generation of electricity without unnecessary disruption. While previous studies show that PV systems fail with a certain rate of probability, PV systems are often regarded as "maintenance free" products, implying that the current users may not be well-informed of the actual characteristics of PV systems such as profitability and failures.

Wakabayashi et al. (2009) shows a result of the field research with the sample number of 725 PV system users that 21.8 % of the total systems have experienced some kind of failures or troubles (with 1.0 % module failures and 9.9 % inverter failures, respectively) [1]. Kato (2009) indicates more severe result of the research with the sample number of 257 users that, within a decade after installation of PV system, 14.0 % of modules and 17.1% of inverters had failed respectively [2].

In parallel with the field researches, these studies have conducted surveys on users' perception of the risk of failures. The results indicate that a gap exists between users' recognition and the actual properties of the system, and that it is difficult for the users to find out failures of PV systems by themselves. Especially, failures which occur on surrounding modules are almost impossible to be noticed by general users because the system still continues to generate electricity with reduced output level. If the users continue to use the system with unrecognized failures on modules or other equipment, it may spawn a serious generation loss during the systems' long lifetime.

Recently the government of Japan and local governments have implemented both R&D support and market-based measures to accelerate the diffusion of PV system. There is, however, a danger that the users don't correctly recognize the risk of failures. Conducting diffusion policies without examining the current public perception relevant to the risk of failures is not only inefficient but also likely induces consumers' distrust on the PV industry.

Hence, the objective of this study is to examine the necessity of countermeasures for the risk of failures from the aspect of users' profitability. Firstly a model was developed and users' profitability considering the risk of failures was simulated throughout the systems' lifetime. To economically assess it, Net Present Value method (NPV) is conducted. Also, the users' perception of the risk of failures was assessed by conducting a questionnaire survey in Kakegawa City, Shizuoka Prefecture, and finally the causing factors of users' misunderstandings about failure risk and profitability of PV systems were analyzed.

2. Modeling Users' Profitability

2.1. Net Present Value method

NPV method is an economic tool to make decisions on public projects or company activities. The methodology of NPV, firstly, confirms the whole economic losses and gains of an investment, and then, calculates the Net Present Value (NPV) or the Internal Rate of Return (IRR) to compare with the benchmark rate of return. NPV can be written as:

$$\mathrm{NPV} = \sum_{n=0}^{N} \frac{\mathrm{NB}_n}{(1+r)^n} \quad (1)$$

where, r, NB_n and N represent, discount rate, a series of net benefits starting from the first year (n=1), and assumed duration of the project, respectively. IRR can be calculated as a discount rate when NPV becomes zero.

In this study, discount rate is assumed as 1%, a relatively low rate, because the users are purchasing PV systems without high profitability.

2.2. Conceptual Model

Fig.1 shows the concept of the developed model for assessing the impact of the risk of failures on the users' profitability.

The economic gains by purchasing a PV system are: (1) decrease of electricity charges by using the electricity generated by the PV system, (2) income by selling electricity. If some components of the PV system fail, economic loss emerges as a decrease in these incomes. The costs, on the other hand, are mainly considered as: (1) initial investment to purchase the PV system, (2) periodical payments for maintenance by manufacturers and (3) unanticipated payments for repairing or replacement of failed system equipment. These economic parameters are considered as inflow and outflow of users' profit.

The electricity power generation of a PV system is calculated by the following equation

$$E_{AS} = P_{AS} \cdot \frac{H_{Ag}}{G_S} \qquad (2)$$

where, E_{AS}, P_{AS}, H_{Ag}, and G_S are representing electricity production, standard test condition (STC) array maximum power, solar irradiation, and STC intensity of solar irradiation (G_S=1), respectively. Correspondence of the equation to the developed model is shown in Fig.1.

Under these assumptions, electricity generation per month were calibrated and the results were in the range of 77.1 [kWh/kW*month] to 95.1 [kWh/kW*month] verifying reliability of the model.

3. Methodology for Assessing Users' Perception

3.1. Hypotheses to test

To assess the users' perception of the risk of failures, a questionnaire survey was conducted for the users in Kakegawa City, Shizuoka Prefecture, and tested responses with following hypotheses.

Firstly, the resistance to the risk of failures might be different among generations, and the number of years of PV system use. For example, compared to the elderly, middle aged users could be more interested in the economic return since they have more uncertainty in their longer life.

Moreover, it is probable that those who have

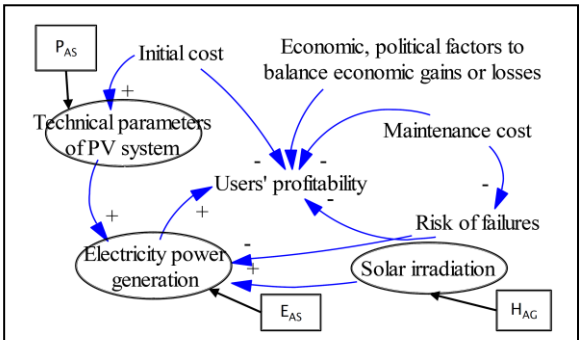

Fig.1. Correspondence of Equation (2) to Conceptual Model

experienced failures might have resistance, anxiety or, potentially, distrust on PV systems as an industrial product which might fail again.

In addition to the possible factors above to make difference on the user's resistance to the risk of failures, ten other questions were asked in the questionnaire survey to use as explanatory variables in ordered logit model. Nine other questions, for classifying the users' resistance and applying as dependent variables, were also asked by the survey.

3.2. Ordered Logit Model

As a method to analyze the response data gathered by the questionnaire survey, ordered logit model (OLM) [3] [4] was adopted. Suppose dependent variable y is ordinal number {0, 1, 2, …, J}, latent variable y^* is assumed as following;

$$y^* = \boldsymbol{x\beta} + \varepsilon, \quad \varepsilon|\boldsymbol{x} \sim \text{Normal}(0,1) \qquad (3)$$

where

$$\boldsymbol{x\beta} = x_1\beta_1 + \ldots + x_k\beta_k$$

In these equations, x_i and β_i represent explanatory variables and estimated coefficients respectively. And ε is an error term which is assumed to follow standardized normal distribution on each x_i.

Each response probability P{y = (0, 1, 2,…, J)|$\boldsymbol{x}$} is estimated by the following equations;

$$\begin{aligned}
P(y=0|\boldsymbol{x}) &= P(y^* \le \alpha_1|\boldsymbol{x}) = P(\boldsymbol{x\beta} + \varepsilon \le \alpha_1|x) \\
&= \Lambda(\alpha_1 - \boldsymbol{x\beta}) \\
P(y=1|\boldsymbol{x}) &= P(\alpha_1 \le y^* \le \alpha_2|\boldsymbol{x}) \\
&= \Lambda(\alpha_2 - \boldsymbol{x\beta}) - \Lambda(\alpha_1 - \boldsymbol{x\beta}) \\
&\vdots \\
P(y=J-1|\boldsymbol{x}) &= P(\alpha_{J-1} \le y^* \le \alpha_J|\boldsymbol{x}) \\
&= \Lambda(\alpha_J - \boldsymbol{x\beta}) - \Lambda(\alpha_{J-1} - \boldsymbol{x\beta}) \\
P(y=J|\boldsymbol{x}) &= P(y^* \ge \alpha_J|\boldsymbol{x}) \\
&= 1 - \Lambda(\alpha_J - \boldsymbol{x\beta}) \qquad (4)
\end{aligned}$$

These response probabilities represent the occurrence

of y_i for a particular set of $\boldsymbol{x}$.

The expected value $E(y|\boldsymbol{x})$ can be simply estimated by the equation;

$$E(y|x) = a_0P(y=a_0|\boldsymbol{x}) + a_1P(y=a_1|\boldsymbol{x}) + \ldots + a_JP(y = a_J|\boldsymbol{x}) \quad (5)$$

Estimates of the expected values can be compared at different values of the explanatory variables to obtain partial effect for discrete x_i.

Tab.1. Parameters Assumed in the Model

Parameters	*Min. value*	*Max. value*	*Const. value*	*Data sources*
Solar Irradiation per month [kWh/m^2]	-	-	116.65	METPV3
STC array power [kW]	-	-	3	-
Performance Ratio [%]	66.1	81.6	-	Ueda(2009)
Price rate of PV system [JPY/kW]	-	-	661,000	NEF
Rate of selling electricity[%]	50	55	-	NEF
Price rate of selling electricity [JPY/kWh]	-	-	24	Tokyo Electric Power Co.
Electricity price [JPY/kWh]	-	-	22.86	TEPCo.
Failure occurrence on module [%]	-	-	0.11	Kato(2009)
Failure occurrence on inverter [%]	-	-	0.14	Kato(2009)

Tab.2. Cumulative Probability Density and Corresponding NPVs

CPD	NPV (JPY)
-	-1,434,420 (Minimum Value)
5.0%	-693,175
10.0%	-610,629
25.0%	-394,512
50.0%	-247,279
75.0%	-111,391
90.0%	-22,376
95.0%	13,457
-	55,699 (Maximum Value)

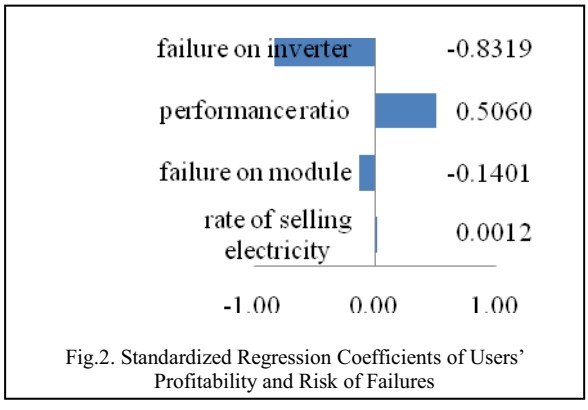

Fig.2. Standardized Regression Coefficients of Users' Profitability and Risk of Failures

4. Results and Discussions

4.1. Users' Profitability under Failure Risk

Tab.1 lists the initial values and parameters used for the Monte Carlo simulation (the calculation number was five thousands), and the results are shown in Tab.2 and Fig.2.

The result in Tab. 2 confirms the well known fact that the profitability of PV systems is still low. The most important part of the result is that the risk of failures requires 5% of users large expense burden in the range of 700,000 to 1,400,000 yen, while 50% of all users are required the burden of expense for less than 250,000 yen. It is regarded that sellers supply PV systems to users without explaining this economic impact of failures.

The standardized regression coefficients in Fig.2 especially show the large impact of inverters' failures on the users' profitability. It is larger than that of the Performance Ratio, which is commonly used as an efficiency indicator for residential PV systems [5].

4.2. Users' Perception of Failure Risk

Before analyzing the responses gathered by the questionnaire survey, with 98 observations, explanatory variables were chosen by checking Spearman's rank coefficients to exclude multicollinearity of explanatory variables.

Tab.3 lists the descriptive statistics of variables chosen for OLM regression analysis. As it can be seen from the explanatory variables *age*, *nmonth* and *newhs*, the sample data seems to be consistent and follows a population of PV system users living in Kakegawa City well.

Although nine dependent variables, relative to the profitability or technical characteristics including the risk of failures, were analyzed, statistically significant results were obtained on only two variables, *willfail* and *willfnd*, listed in Tab.3.

Tab.4 shows estimated regression coefficients, standard errors, and significance level of each variable. The most interesting finding is that the users joining in a civic organization which is active on PV systems (representing the variable *org*) tend to think that their PV systems might fail (*willfail*), while those who just wish to contribute to environmental issues (*env*) think in an opposite way. By calculating equation (5), where *org* ascends from 0 to 1, the expected value of *willfail* also ascends from 3.5 to 4.3, while, where *env* ascends from 1 to 5, the expected value descends from 4.2 to 3.3.

The reason for these results is the consideration that civic group members share information and learn from each other about PV systems, but the

Tab.3. Descriptive Statistics of Explanatory and Dependent Variables for OLM Regression Analysis

	Meanings of variables	Mean	Std.Dev.	Min.	Max.
age	the number of age	56.745	13.620	29	86
fail	if respondent has experienced failures, 1	0.094	0.294	0	1
nmonth	the number of months using PV	30.411	32.295	0	108
newhs	if a respondent installed PV when bought a new house, 1	0.369	0.485	0	1
env	Were you encouraged to purchase PV for contribution on environmental issue? (5 = strongly, 1 = totally not)	4.204	0.824	1	5
econ	Were you encouraged to purchase PV for economic return? (5 = strongly, 1 = totally not)	4.418	0.759	1	5
renew	if a respondent uses other renewable energy technologies, 1	0.196	0.399	0	1
org	if a respondent joins in civic activity related to PV, 1	0.095	0.295	0	1
willfail	Do you think your PV will fail? (5 = strongly think so, 1 = totally not)	3.388	1.118	1	5
willfnd	If your PV fails, do you think you can find it out by yourself? (5 = strongly think so, 1 = totally not)	3.133	1.081	1	5

Tab.4. OLM Regression Results about Users' Perception of the Risk of Failures

	willfail		*willfnd*	
age	-0.0326		0.0200	
	0.0216		0.0208	
fail	0.0658		0.1910	
	0.8875		0.8553	
nmonth	-0.0003		0.0340	***
	0.0082		0.0101	
newhs	1.1849	**	-0.3977	
	0.5360		0.5381	
env	-0.5825	*	-1.0034	***
	0.3365		0.3591	
econ	-0.0448		0.8081	**
	0.3176		0.3352	
renew	0.1936		1.4224	*
	0.8482		0.7690	
org	2.7713	**	0.7849	
	1.2108		1.1968	
χ^2	13.98		29.08	
p-value	0.0823		0.0003	

Statistical significance: *** p<0.01; ** p<0.05; * p<0.1

environment-friendly users are, on the other hand, satisfied only with the installation of a PV system on their houses and not so much interested afterwards. In case the users encounter failures, they will be disappointed and distrust the PV market. It is implied by these findings that networking has a positive effect to improve the resiliency of the PV market.

It is equally interesting that the longer users use PV systems (*nmonth*), the more people think that failures on PV systems are easily found out (*willfnd*). A long and safe duration of use might eventually make users to trust PV systems, and feel confident enough to do it. But the risk of failures certainly increases as time goes on. It is more necessary to support users in a longer term.

In this analysis, no significant findings relative to the users' perception of the profitability could be obtained. It might be partly because the users are confused whether PV systems are profitable or not and the government has recently provided several types, and amount, of subsidies for residential PV systems. The effect of these subsidies on the users' perception should be analyzed as a further study.

5. Conclusions

The main finding of this study, in evidently, is that the risk of failures, especially which on the inverter, has relatively high impact on users' profitability, and the current users have not recognize it properly. In particular, users who wish to contribute to the environmental issues tend to think that their PV systems will not fail. To use PV systems sustainably, it is critical to inform the risk of failures to users.

The future direction of this study will be to probabilistically examine the risk of failures in greater detail, considering other components of failures or troubles such as failures on bypass diodes or deficient work of installation. There is also a need to assess social costs by failures, especially those on modules, which are hard to find out by the users alone but continue generating electricity with decreased output.

References

[1] Wakabayashi H., T. Igarashi, K. Otani, T. Takashima (2009) Users' awareness of residential PV systems' failures. *IEE Japan Technical Meeting of Power and Energy*, 08 – 3.

[2] Kato K. (2009) Reality of the maintenance condition of residential PV systems. *AIST Fifth Annual Symposium of Research Center for Photovoltaics*, pp. 179 – 180.

[3] Greene W. H. (2008) Econometric Analysis: Sixth Edition. Pearson Prentice Hall.

[4] Wooldridge J. M. (2002) Econometric Analysis of Cross Section and Panel Data. MIT Press.

[5] Ueda, Y., K. Kurokawa, K. Kitamura, M. Yokota, K. Akanuma, H. Sugihara (2009) Performance analysis of various system configurations on grid-connected residential PV systems. *Solar Energy Materials and Solar Cells*, **93**, pp. 945 – 949.

[6] Gnedenko B., I. Pavlov, I. Ushakov, S. Chakravarty (1999) Statistical Reliability Engineering. Wiley Interscience.

A NUMERICAL STUDY ON TURBULENCE IN THE URBAN CANOPY LAYER AFFECTED BY THE ATMOSPHERIC BOUNDARY LAYER

Student Number: 08M18157　Name: Yoshimi YAMASHITA　Supervisor: Manabu KANDA

大気境界層の影響を考慮した都市キャノピー層の乱流に関する研究

山下　佳美

本論ではLESモデルを使って，都市キャノピー層内の瞬間的な流れ場について研究した．ストリートキャニオンの瞬間的な流れ場は平均場とは全く異なっており，中でも特に，大規模上昇流(フラッシング)や強い渦を巻く流れ(キャビティ渦)は鉛直方向の熱輸送に大きく寄与している．更に，ストリートキャニオンの個々の流れ場は局所的に発生しておらず，接地境界層に発達する組織的乱流構造にかなり対応して発生している．

1 Introduction

Recently, various environmental problems in cities, such as heat island and concentrated heavy rainfall, are worsening. To figure out these problems, it is important to investigate the turbulent characteristics within the Atmospheric Boundary Layer (ABL) above an urban setting, because turbulence determines the transport of heat, momentum and scalars between the surface and the atmosphere. Various studies have revealed that these processes are dominated by turbulent coherent structures (CS), which is observed in the Surface Layer (SL) (Inagaki [1]).

Flow field in the Urban Canopy Layer (UCL) has been also studied. Uehara et al. [2] investigated the characteristics of the mean flow in a street canyon under various atmospheric stabilities by wind tunnel experiment. Kanda et al. [3] observed that the instantaneous flow in a street canyon is completely different from the mean flow. Takimoto [4] observed strong upward motions in Particle Image Velocimetry (PIV) experiment at a comprehensive outdoor urban scale model (COSMO). These upward motions might be related to the CS in the SL. Since previous researches about the urban canopy did not consider the effect from the CS in SL, interactions between the UCL and the SL above is unclear.

On the other hand, turbulence in the SL is affected by the mixed layer (ML), as Inagaki and Kanda [5] demonstrated that the turbulent CS is affected by the outer scale (ML) eddy. Therefore, in simulating the SL, it is necessary to include the whole ABL. Zhang [6] simulated the whole ABL above the UCL, resolving the structures by LES (Large Eddy Simulation). The turbulent CS is also observed in this simulation. This LES model is useful to study a connection between the SL and UCL because it included the ABL and the urban structures in the simulation. However the flow in the UCL is not investigated in his study because the resolution is not fine enough.

This present study investigates the characteristics of the instantaneous flow fields in the UCL with the same LES model using smaller grid spacing. Specifically, the relation between the UCL and the turbulent CS in the SL is also analyzed.

2 Simulation Condition

In this study, the UCL affected by the ABL is simulated. An LES model, PALM (Parallelized Large-eddy simulation Model), which is developed in Hannover University, is employed, and TSUBAME grid cluster system in TITech was used to calculate (Castillo et al [7]).

The computational domain, which has a size of 2560m × 2560m × 17096.0m, is large enough to simulate the whole ABL. The grid spacing, which is 2.5m, is small enough to resolve the flow detail in the UCL. 1024 cubes of 40m (=H; building height) dimension are arranged uniformly on the ground with a plane area density is 0.25. To simulate the real ABL, the initial temperature is set up as follows; temperature on the ground was initially set up as 300K, the temperature gradient from 0m to 800m as 0.07 K/m, and that from 800m to the top as 0.74K/m. The initial wind velocity was set up as 20m to the streamwise (x) direction. The heat flux is supplied from the ground and the roof, and set as 0.10 K・m/s.

3 Result and discussion

3.1 Mean flow in the street canyon

Characteristics of the mean flow field at the street canyon are discussed using phase averaged data compared with the results from PIV experiment (Takimoto [4]) measured in COSMO. The phase average was obtained by averaging all the 2H horizontal square sections which includes one cube.

Figure 1 shows the streamwise-vertical (xz) cross sectional vector map, which passes the center of building, and the potential

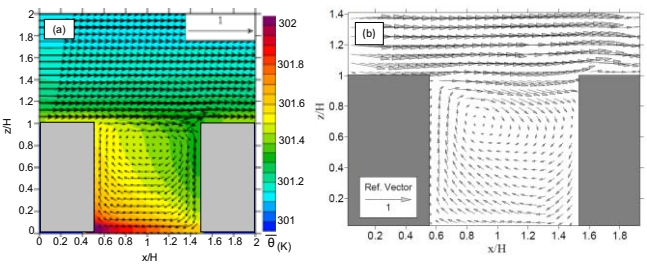

Fig-1 Vector map of mean flow (a) Simulation (b) PIV

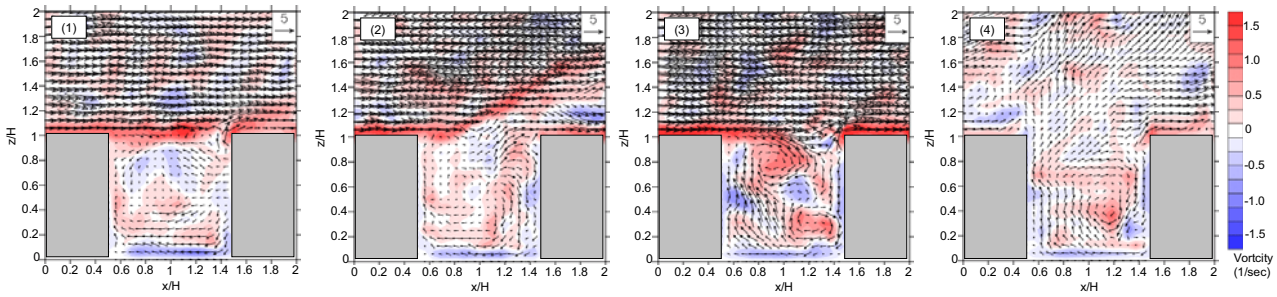

Fig-2 Example of classifications

temperature contour. Velocity is normalized by the mean velocity at z=2H, U_{2H}. According to Figure 1, an eddy is blowing between the blocks, which is called cavity eddy. For the PIV results [4], the center of this eddy is located at the upstream side of the block. This anomaly may be due to the difference in stability for the two experiments. In this simulation, the stability is near-neutral, while in the PIV experiment the stability is slightly unstable. Moreover, in the PIV measurement, wind direction is not always parallel with the x-direction. The potential temperature in the canyon at z=H is lower than that at the roof since heat is also supplied from the roof. The potential temperature by the leeward wall is lower than that at the windward wall since there is a strong downdraft at the leeward wall.

3.2 Instantaneous flow in the street canyon

Instantaneous flows in the street canyons are completely different from the mean flow. They can be classified into four groups using its vorticity distribution as an index. Moreover, large-scale upward wind, which is called flushing by Takimoto [4], and flows into the canyon, which is referred as cavity eddy, are important events.

a) Classifying the flow fields

Figure 2 shows an example of the vector map of each flow classification group. They are classified by the vortex sheet developing from the windward roof. The vortex sheet is located between a fast flow field above the canopy, and the slow flow field within the canopy. Thus, the vortex sheet is treated as the boundary between the flows. The following are the definition of groups and their characteristics.

(1) Fully capped: in this group (Figure 2 (1)), the vortex sheet is developed from the windward roof and continues to the other roof. Thus, the flow fields within and above the canopy are separated.

(2) Opening capped: in Figure 2 (2), the vortex sheet divides the flow field as well, then the vortex sheet opens up and goes over the UCL. There is an updraft of slow flow from the UCL, penetrating the SL.

(3) Caving capped: the vortex sheet is within the canyon (Fig.2 (3)). The fast flow field above the canopy is brought down into the canyon, increasing the velocity in the canyon.

(4) None-capped: there is no peak in the vorticity (Fig.2 (4)). Since the velocity gap between flow fields within and above the canyon is insignificant, there is no obvious vortex sheet. The air can easily go upward, and the vectors in this flow are not large.

b) Flushing

Takimoto [4] observed instantaneous large scale upward motion and named it “flushing”. Flushing is defined as “more than 55% of vectors satisfy the condition of $w > |u|$ in street canyon”. This definition is also applied in this study. All the xz-cross sections which pass through the center of a building are used in the extraction of flushing events (992 sections). Thirty-one flushing events are extracted. In Figure 3 (a), an example of a contour shows the spanwise vorticity. The large scale upward wind occurs and continues above the building. The vorticity is small since the velocity gap is very small.

Figure 4 (a) shows the ensemble-averaged vector map of all the sections where flushing occurs. Here, the velocity is normalized by U_{2H} and the contour shows potential temperature. It is relatively warmer in the canyon where flushing occurs.

Figure 5 shows the streamwise-spanwise (xy) cross sectional vector map of ensemble averaged flushing near the ground (z = 0.0625H) and at roof level (z = H). Ensemble averaged flushing is obtained by averaging all the 3H horizontal square sections which includes two cubes. Because flow converges at z = 0.0625H and does not diverge at z = H, the flow from the y-direction at z=0.0625H continues to flow upward (i.e. flushing). Thus, flushing occurs with the upgathering of air at the lower region of the UCL, and transporting this air toward above the canopy. Also, the potential temperature in the street canyon is higher because the spanwise convergence transports heat.

Figure 7 (a) illustrates the sensible heat flux profile where flushing occurs within and above the canopy. Dashed-line shows the average from all the canyons, while dotted-line for the other canyons from flushing. When flushing occurs, the sensible heat flux within and above the canyon is larger than the mean sensible heat flux. The value is more than 0.10 K·m/sec, which is the heat flux from the ground. This means that the heat is gathered from the entire canyon and brought to the flushing points. This demonstrates that the flushing events contribute to the heat transport from the ground to the atmosphere, and flushing is quite important event in considering the relation between the SL and the UCL.

c) Cavity Eddy

Figure 3(b) shows the instantaneous cavity eddy. The flow just above the building is very fast and comes down into the canyon along the leeward wall. This downward motion makes a strong eddy (i.e. cavity eddy). Focusing on vorticity distribution,

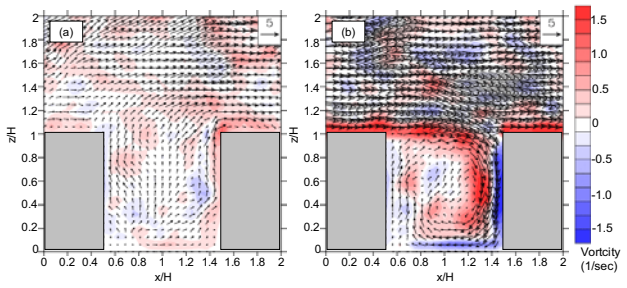

Fig.3 Example of (a) Flushing, (b) Cavity eddy

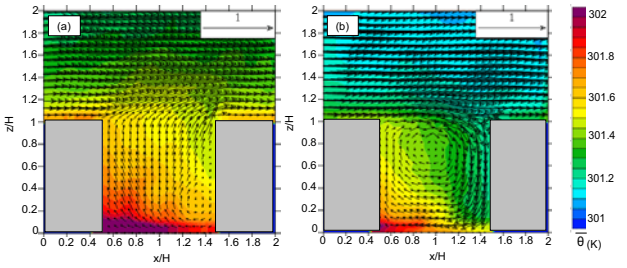

Fig.4 Vector map of ensemble averaged (a) Flushing (b) Cavity eddy (Xz-sectional profile through the center of building)

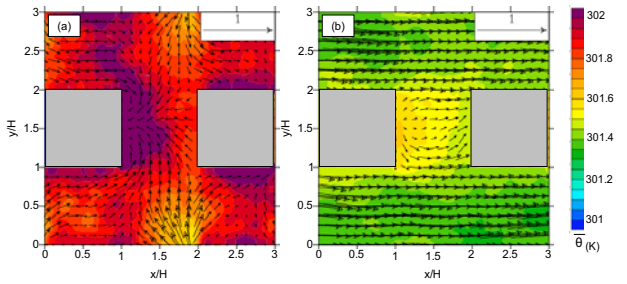

Fig.5 Xy-sectional vector map of ensemble averaged Flushing (a) z=0.0625H (b) z=H

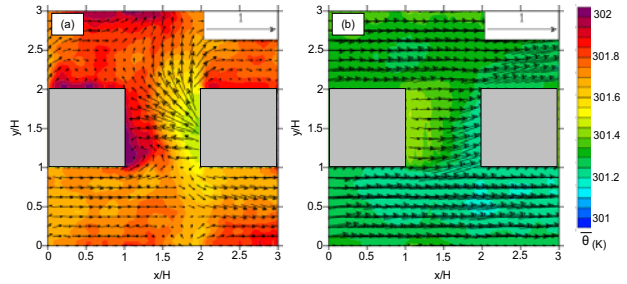

Fig.6 Xy-sectional vector map of ensemble averaged Cavity eddy (a) z=0.0625H (b) z=H

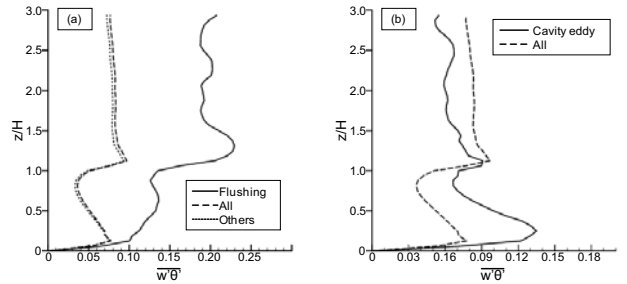

Fig.7 Sensible heat flux profile within and above the street canyon (a) Flushing (b) Cavity eddy

the positive vortex sheet developing from the windward roof continues down into the canyon just in front of the leeward roof. Moreover, a strong negative vortex sheet is developed between the positive vortex sheet and the leeward wall. This flow field can be classified into group (3).

In this study, this cavity eddy is defined as follows: more than 70% of vectors satisfy the condition of $w < 0$ and $\sqrt{u^2 + w^2} > |\sqrt{u^2 + w^2}|$ in a quarter leeward region of the street canyon, where $|\sqrt{u^2 + w^2}|$ represents the averaged $\sqrt{u^2 + w^2}$ in the target xy-section in a street canyon. All the xz-cross sections passing through the center of a building are used, wherein 37 events are extracted as the defined cavity eddy.

Ensemble averaged vector map from these sections is shown in Figure 4 (b). For the mean flow, a stronger cavity eddy exists and cooler downdraft enters intensely along the leeward wall, thus, transporting cooler air into the UCL.

Figure 6 shows the xy-cross sectional vector map of ensemble averaged cavity eddy at z = 0.0625H and z = H. Since each cavity eddy has a spanwise directionality, the flow field's negative spanwise flow is transformed to make it symmetrical with respect to y-axis. At z = 0.0625H the downward flow caused by a strong cavity eddy reaches the leeward side of the upstream block (i.e. the upstream side of the street). At z=H the spanwise flow is smaller than that of z=0.0625H. In this level, the velocity in the upstream side is smaller than that in the downstream side. In both figures, the upstream side is warmer than the downstream side. As a consequence, when cavity eddy occurs, flow on one side of the canyon street is warmer and faster than the other, and the air goes to the warmer side of the canyon.

Figure 7 (b) shows the sensible heat flux profile within and above the canyon where cavity eddy occurs. Dashed-line shows the average from all the canyons as well. Within the street canyon, more heat transports upward than by the mean flow. However the heat flux above UCL is not larger than the mean flow. Thus, cavity eddy transports the heat locally in the street canyon.

3.3 Relation between flow in the UCL and the turbulent CS

Figure 8 shows the streamwise velocity distribution at z = H/16 and turbulent CS at SL. The Low speed streak at z = 2H is visualized as a CS by illustrating the negative fluctuation of the mainstream velocity. This fluctuation contains only the inner scale motion, distinguished by spatially filtering the instantaneous fluctuation velocity using an area of 10H×10H (Castillo et al. [7]). From this figure, the spanwise velocity is converging under the streak. The flow field in the UCL is not localized but well organized and is affected significantly by the SL.

Figure 9 shows the CS and the points where flushing occurs. In this figure, the CS is visualized by sweep-ejection events, which are obtained from quadrant analysis. Black lines show the sections where flushing occurs. Flushing events are extracted from the canyons of all the xz-cross sections. According to Figure 9,

flushing events occur along ejections, of which u' is negative and w' is positive. Thus, under the ejection events, flushing occurs frequently. Since an ejections correspond to low speed streaks, air converges in the spanwise direction at z=0.0625H under ejections. In fact, the flow converges along the spanwise direction in the street canyon during flushing.

Figure 10 illustrates the sweep-ejection events and the points where cavity eddy exists. Most cavity eddy occurs between ejections and sweeps (white region). This is the region where the air flows in a spanwise direction at z=0.0625H. In fact, the street canyon with cavity eddy has a spanwise flow at z=0.0625H.

4 Conclusion

In this study, the flow in the UCL affected by the ABL is well simulated with LES. The following are the deductions from the simulation results.

- Instantaneous flow fields at the street canyon, which are completely different from the mean flow, can be classified into four groups, using their vorticity as the index.
- Flushing, a large-scale upward wind in the street canyon, is the upgathering of air and heat at the lowest level of the street canyon and brought up above the canopy. It has significant contribution of heat transport.
- Cavity eddy, a strong eddy blowing down into the street canyon, transports the cool air from the SL into the canyon. At the lowest level, the air going only to the warmer side of the street.
- The flow field in the UCL corresponds to the turbulent CS in the SL. Specifically, flushing frequently occurs under an ejection event, and cavity eddy between ejections and sweeps.

Reference

[1] Inagaki, A.: 'Atmospheric turbulence over an array of massive cubes', Phd thesis, Tokyo Institute of Technology, 2008.

[2] Uehara, K., Murakami, S., Oikawa, S., and Wakamatsu, S.: 'Wind Tunnel Experiments on How Thermal Stratification Affects Flow in and above Urban Street Canyons', *Atmos. Environ.* **34**, pp.1553–1562, 2000.

[3] Kanda, M., Moriwaki, R., and Kasamatsu, F.: 'Large Eddy Simulation of Turbulent Organized Structure Within and Above Explicitly Resolved Cube Arrays', *Boundary-Layer Meteorol.* **112**, pp.343–368, 2004

[4] Takimoto, H.: 'PIV measurements of atmospheric turbulence within and above an outdoor urban scale model', Master thesis, Tokyo Institute of Technology, 2009

[5] Inagaki, A. and Kanda, M.: 'Turbulent flow similarity over an array of cubes in near-neutrally stratified atmospheric flow'. *J. Fluid Mech.*, **615**, pp101-120, 2008.

[6] Zhang, J.: 'LES study on hierarchical turbulence organized structure above urban canopy', Master thesis, Tokyo Institute of Technology, 2009.

[7] Castillo, M. C. L., Zhang, J., Inagaki, A., Kanda, M. and Letzel, M. O.: 'Coherent structures of a neutrally stratified urban boundary layer using large-eddy simulation, Urban Climate News, International Association for Urban Climate, **33**: 19-22, 2009.

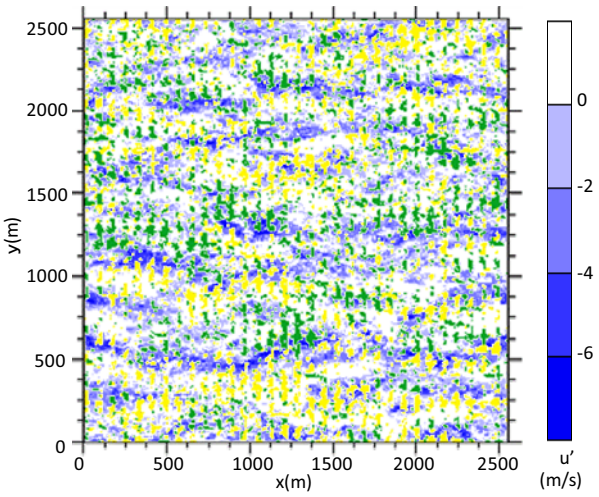

Fig.8 Comparing the distribution v' at z=0.0625H with low speed streak in surface layer (yellow; v'>2.0m/s, green; v'<-2.0m/s)

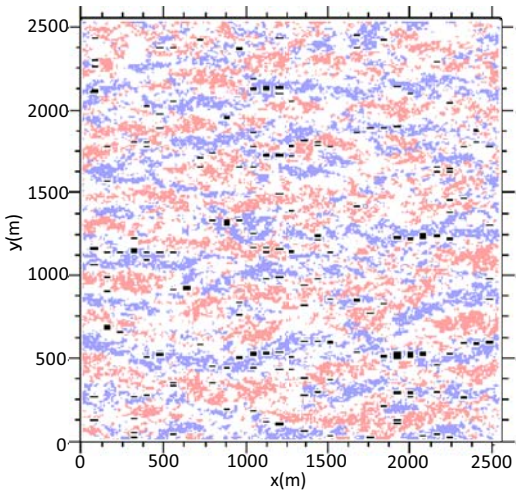

Fig.9 Flushing points and sweep/ejection (red; sweep, blue; ejection)

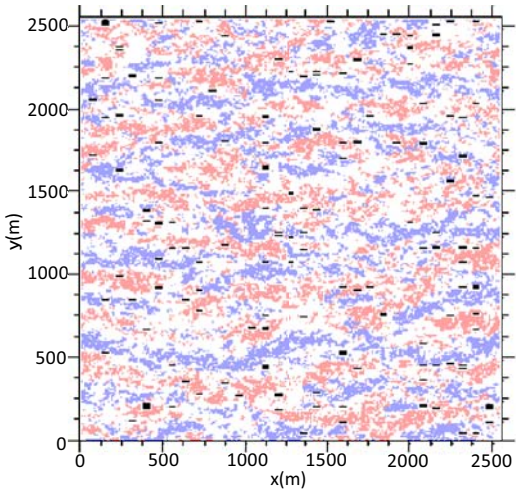

Fig.10 Cavity eddy points and sweep/ejection (red; sweep, blue; ejection)

Evaluation on Durability of the Autoclaved Cement-based Material using γ-C_2S

Student Number: 08M18163 Name: Tatsuya YUMOTO Supervisor: Nobuaki OTSUKI

γ-C_2S を混和しオートクレーブ養生したセメント系材料の耐久性評価

湯本達也

常温では水硬性を示さないが，炭酸ガスと高い活性を示すγ-C_2S を混和材としてセメント系材料に添加することで，高い耐久性を得る研究が注目されている．すなわち，OPC，γ-C_2S およびケイ石微粉末を用いたセメント系材料にオートクレーブ養生および炭酸化養生を行うことで，化学的安定性および収縮抵抗性を有するとともに外部劣化因子に対して高い浸透抵抗性を示す材料設計が提案されている．しかしながら，コンクリート構造物において重要となる耐硫酸塩性については未だ検討されていない．したがって，本研究ではγ-C_2S を混和しオートクレーブ養生したセメント系材料の耐硫酸塩性を実験的に検討した．その結果，OPC に対するγ-C_2S 置換率を 80%とすることで，高い耐硫酸塩性を有することが確認された．

1. Introduction

Nowadays, the use of cement-based materials in engineered barriers is being considered in the construction of radioactive waste disposal facilities. A material design of cement-based material is expected to obtain a good mechanical performance and shielding properties against aggressive ions. For this purpose, it undoubtedly is obvious that high durability cement-based material is in demand, especially, in the Middle East region, wherein sulfate soil is abundantly found. Sulfate attack is one of the major factors that can contribute in the deterioration of the concrete structures.

On the other hand, the research on the high durability of the cement-based material using γ-$2CaO{\cdot}SiO_2$ (hereafter"γ-C_2S") is focused. γ-C_2S does not react with water under normal curing but it reacts well with CO_2 gas. The cement-based material, mixed with γ-C_2S and resulted densified surface through carbonation curing, has high durability for the long term purpose was reported[1]. Furthermore, the amount of 1.1nm tobermorite ($5CaO{\cdot}6SiO_2{\cdot}5H_2O$, hereafter"tobermorite") which has high shrinkage resistance is increased by mixing γ-C_2S and conducting the autoclave curing. Saito[2] has proposed the concept of material design for high durability cement-based material in high shrinkage resistance by generating the tobermorite in the hardened body using autoclave curing and high permeability resistance to external aggressive ions such as chloride ion by densifying the surface on the hardened body through carbonation curing (Fig.1).

However, the designed material has high durability only in theoretical consideration but experimental durability performance, especially the sulfate attack, has

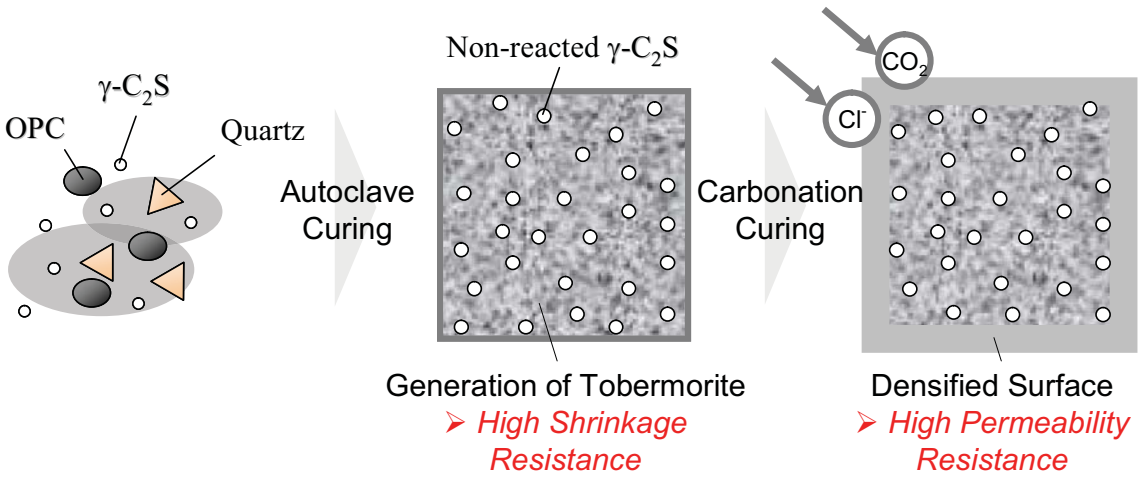

Fig.1 Concept of material deign for high durability cement-based material

Table.1 Chemical composition and physical property of materials

	Chemical composition (mass%)						Density (g/cm^3)	Blane specific area (cm^2/g)
	SiO_2	Al_2O_3	Fe_2O_3	CaO	SO_3	f.CaO		
OPC	21.6	5.08	2.93	64.5	1.95	0.4	3.16	3310
γ-C_2S	35.0	1.7	0.10	61.9	-	-	3.01	3060
Quartz	93.3	1.6	1.4	-	-	-	2.66	3870

Table.2 Mix proportions and curing method of cement paste specimens

Name	W/ (C+γ+Q)	Unit mass (kg/m^3)							Curing	
		W	C	γ	Q	S	G	CA*	Autoclave	Carbonation
Ref	0.3	487	1622	0	0	-	-	7.70	-	-
γ-0		464	774	0	774	-	-	7.70	○	○
γ-20		463	617	154	772	-	-	7.70	○	○
γ-40		462	462	308	770	-	-	7.70	○	○
γ-60		461	307	461	768	-	-	7.70	○	○
γ-80		460	153	613	766	-	-	7.70	○	○

*CA: High AE water reducing reagent

not been investigated yet. Therefore, this study aims to evaluate an effect of the γ-C_2S substitution ratio, autoclave curing and carbonation curing to the sulfate resistance from the view point of the reactive products and the sulfate ions penetration.

2. Experimental Methodology

2.1 Materials and Mixing

The materials used in this study as binder are ordinary portland cement (OPC), γ-C_2S and quartz. Table.1 shows the chemical composition of these materials. Chemical admixtures used were high AE water reducing reagent.

Table.2 shows the mix proportions of cement paste specimens and curing method. γ-C_2S was mixed with 0, 20, 40, 60 and 80% of OPC to provide a source of lime. The lime source (OPC+γ-C_2S) and quartz were mixed in a ratio of 5:5 and deionized water was added to the powder at water-binder ratio (W/{C+γ+Q}) of 0.3. The mixed cement paste was cast in a mold (volume of 10×10×80mm and ϕ50×100mm).

2.2 Curing

After the initial curing at RH100% for 4 hours, the cement paste was demolded and autoclaved for 8hours at 180ºC and 1MPa. Accelerated carbonation curing of the specimens was carried out in CO_2 concentration 5vol% at 20ºC and RH60% for 28days. In addition, non-autoclaved and non-carbonated cement paste of only OPC, which we assumed a generally cement-based material, was made.

2.3 Sulfate Exposure Test

The sulfate exposure test that the specimens were exposed to the solution of Na_2SO_4 5% by mass at 20ºC for 36weeks was conducted. In order to keep a concentration of Na_2SO_4, the solution was exchanged every 2weeks. After the exposure test, each specimen was dipped into a large volume of acetone at 20 ºC for 1 hour under reducing pressure ($2.33\times10P^3$a), to terminate the hydration. Afterwards, reduced pressure drying was carried out for 24 hours for each analysis.

2.4 Evaluation on Performance

Compressive strength was measured according to JIS R 5201 using the cylinder specimens (ϕ50×100mm).

The identification of reactive products by using X-ray diffraction (XRD) was conducted. The samples were grinded to give a sample, which were cut at 0-2mm (surface part) and 8-10mm (core part) from exposed surface. The samples were scanned between 5º and 70º with an X'Celerator detector.

In order to evaluate the sulfate ion penetration, elemental analysis of the hardened body by using the

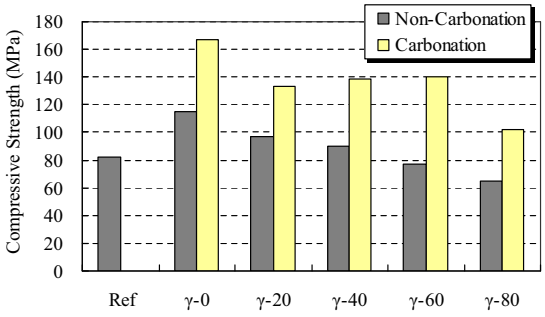

Fig.2 Compressive strength before exposure

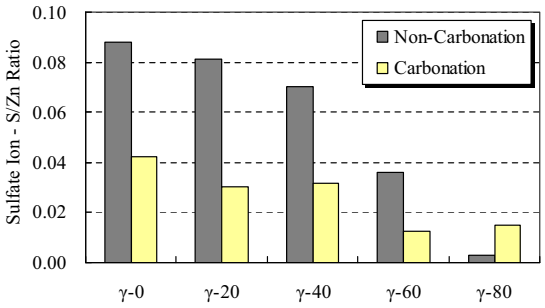

Fig.3 Sulfate ion penetration after exposure

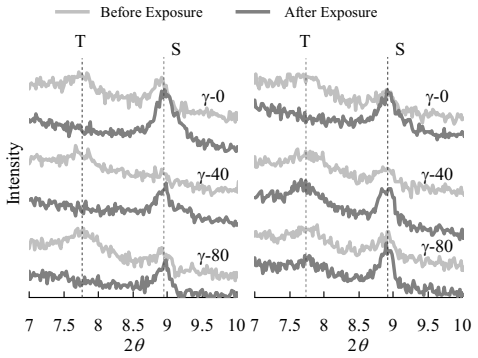

(a) Non-carbonation (b) Carbonation

Fig.4 XRD patterns at core part after exposure

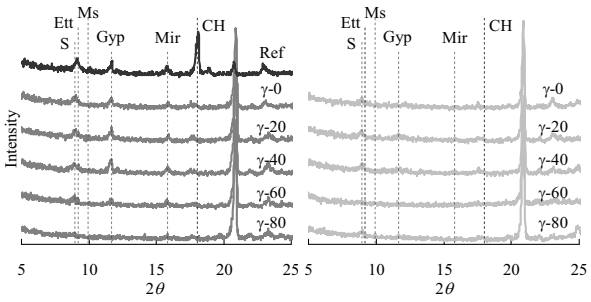

(a) Non-carbonation (b) Carbonation

Fig.5 XRD pattern at surface part after exposure

Energy Dispersive X-ray spectrometry (EDX, current: 60~80μA, voltage: 15V) was carried out. The sulfate ion penetration was calculated as S/Zn ratio by identification of the sulfate and zinc element using the internal reference (ZnO) method. Additionally, Ca/Si molar ratio and decreasing rate of Ca/Si molar ratio after exposure test were also calculated.

3. Results and Discussion

3.1 Compressive Strength

Fig.2 shows the experiment result of compressive strength before exposure test. The compressive strength decreased as γ-C_2S was mixed with OPC. However, the compressive strength of carbonated specimen increased. Therefore, admixing OPC with γ-C_2S and conducting the carbonation curing improved the compressive strength.

3.2 Effect to the Sulfate Ion Penetration

The sulfate ion penetration measured by elemental analysis using EDX is shown in Fig.3. The sulfate ion penetration decreased as the γ-C_2S substitution ratio increased and carbonation curing was conducted. Especially, in the case of γ-C_2S substitution ratio was 80%, the sulfate ion penetration was the smallest.

3.3 Effect to the Reactive Product

Fig.4 shows XRD patterns of the specimens at the core part on before and after exposure test. Here, the “T” corresponds to tobermorite and “S” is sericite, which represents the impurities included in quartz. In the case of carbonated γ-40 and γ-80, the peak intensity of the tobermorite after exposure was confirmed. On the other hand, the peak intensity of tobermorite in the non-carbonated specimens was not confirmed. This result is attributed to densification due to the generation of vatelite by the reaction of γ-C_2S with CO_2 gas conducting the carbonation curing[1]. It can be considered that the dissolution of tobermorite in the core part by sulfate attack was inhibited due to densified surface of hardened body.

Fig.5 shows XRD patterns of the specimens at surface part after exposure test. Here, the “Ett” corresponds to ettringite, “Gyp” is gypsum, “Mir” is mirabilite ($Na_2SO_4 \cdot 10H_2O$), which are known as the expansive reaction products regarding the sulfate attack, the “Ms” is monosulfate, “CH” is $Ca(OH)_2$, and “S” is sericite. The expansive reaction products such as Ett, Gyp and Mir were not generated with a γ-C_2S substitution ratio of 80%. Additionally, in the case of carbonated specimens, the expansive reaction products were also not generated

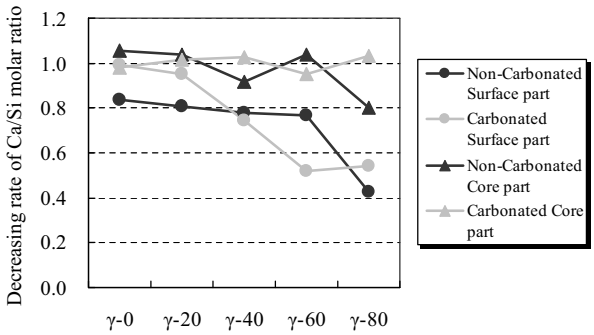

Fig.6 Decreasing rate of Ca/Si molar ratio

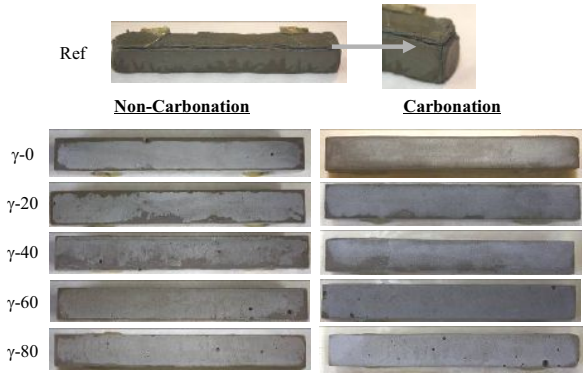

Fig.7 SEM photographs of specimens after exposure

in each mix proportion. However, in the case of Ref, which is non-autoclaved and non-carbonated specimen, the expansive reaction products were generated.

The decreasing rate of Ca/Si molar ratio is shown in Fig.6. The decreasing rate of Ca/Si molar ratio at the surface part decreased as the γ-C_2S substitution ratio increased in spite of the carbonation curing. Especially, in the case of γ-C_2S substitution ratio 80%, it was the smallest.

These results are attributed to dissolution of γ-C_2S. Silica gel and C-S-H gel, whose Ca/Si molar ratio was low, was generated at the surface part due to the much Ca^{2+} leaching from the non-reacted γ-C_2S, because there are much non-reacted γ-C_2S in the hardened body in the case of the high γ-C_2S substitution ratio (60 and 80%). Therefore, it can be considered that the surface part of hardened body was densified due to generation of a silica gel and low Ca/Si molar ratio's C-S-H gel caused by the dissolution of non-reacted γ-C_2S. Furthermore, if carbonated, the sulfate ion penetration more decreased due to densification by generation of vatelite[2] ($CaCO_3$) was confirmed. Then, the sulfate ion penetration was inhibited at the surface part and the tobermorite remained at the core part.

3.4 Evaluation on the Sulfate Resistance

Fig.7 shows the photographs of specimens after exposure test. In the case of Ref, the large crack on its surface was confirmed due to generation of the expansive reaction products such as an ettringite, from Fig.5. This means the deterioration by sulfate attack was occurred. On the other hand, the crack and deterioration on the autoclaved specimens were not observed by visible observation. Therefore, the sulfate resistance was improved by conducting the autoclave curing. Especially, in the case of carbonated γ-C_2S substitution ratio is 80%, the sulfate ion penetration was the smallest and the tobermorite in the hardened body remained, due to generation of silica gel, low Ca/Si molar ratio's-S-H gel and vatelite. Therefore, the highest sulfate resistance was obtained with γ-C_2S substitution ratio 80% and conducting the autoclave curing and carbonation curing.

4. Conclusion

The conclusions of this study are as follows:

- In the case of γ-C_2S substitution ratio 80% conducted autoclave curing and carbonation curing, the highest sulfate resistance was obtained. Because the sulfate ion penetration was the smallest and the tobermorite in the hardened body remained.
- It could be considered that the mechanism of sulfate resistance was densification on the surface of the hardened body due to generation of a silica gel and low Ca/Si molar ratio' C-S-H by dissolution of non-reacted γ-C_2S and generation of the vatelite by conducting the carbonation curing.

【References】

1) K. Watanabe *et al* : High durability cementitious material with mineral admixtures and carbonation curing, Waste Management, No.26, pp.752-757(2006)

2) Tsuyoshi Saito *et al*: Carbonation Reaction of Calcium Silicate Hydrates by Hydrothermal Synthesis at 150ºC in OPC- γ-Ca_2SiO_4-a-Quartz Systems, Journal of Advanced Concrete Technology, Vol.5, No.3, pp.333-341(2007)

Process of absorption oil separation using solvent extraction and distillation

Student Number: 08M18170 Name: Yoshihisa YOSHIMURA Supervisor: Ryuichi EGASHIRA

溶媒抽出法、蒸留法を用いたコールタール吸収油の分離プロセス

吉村　克久

まず，吸収油に含まれる成分の一部（キノリン，2-メチルナフタレン）および抽出溶媒成分（メタノール，水）からなるモデル系に対して，計算により気液液平衡関係を推定した。ついで，吸収油の溶媒抽出における抽出相を想定した同モデル混合物の回分単蒸留を行い，前述の推定結果を定性的に確認した。さらに，これらの結果およびプロセス計算に基づいて，吸収油を含窒素複素環式化合物と同素環化合物等とに分離するプロセスを合成，提案した。

1. Introduction

Absorption oil (AO), one of the coal tar fractions (b.p. =470~550K), contains nitrogen heterocyclic compounds, such as quinoline (Q), homocyclic compounds, such as 2-methylnaphthalene (2MN), etc., which are useful as industrial raw materials. Currently, this AO is, firstly, separated into acid, base, and neutral fractions by reactive extraction with acid and base, and these three fractions are, secondly, provided to downstream step to be separated into respective compounds. In this first separation step, there are some problems such as difficulty in solvent recovery and equipment corrosion. To solve these problems, several alternative methods, such as solvent extraction method, have been studied. Solvent extraction technique can separate AO into nitrogen compound and the other compounds by polarity difference. In one of these studies[1], distillation was applied to recover the extraction solvent, mixture of methanol(M) and water (W). In this distillation, the bottom product formed two immiscible liquid phases; extracted components rich and water rich phases. These were easily separated by decantation. As result, this study showed that not only recovery of solvent, but also further separation between nitrogen compound and the others were achieved.

In this study, the AO separation process including the solvent recovery was investigated. In the first, the phase equilibrium of representative components of AO and solvent components was calculated. Next, the mixture of AO and solvent components were separated by a simple distillation. Finally, some AO separation processes were investigated by calculation.

2. Phase equilibrium in AO and solvent components

2.1. Calculation

The mass fraction of some main compounds in AO is shown in **Table 1**. Q and 2MN are largest components in nitrogen heterocyclic compounds and homocyclic compounds in AO, so these were selected as representative components. Phase equilibrium in Q-2MN-M-W quaternary system was calculated. In this calculation, following equations were used,

< Thermodynamic equation >

$$y_i P = \gamma_i^{\mathrm{A}} x_i^{\mathrm{A}} P_i^{\mathrm{S}} = \gamma_i^{\mathrm{B}} x_i^{\mathrm{B}} P_i^{\mathrm{S}} \quad (i = 1, 2, \ldots, C) \qquad (1)$$

< Material balance equation >

$$F = V + L^{\mathrm{A}} + L^{\mathrm{B}} \qquad (2)$$

$$F z_i = V y_i + L^{\mathrm{A}} x_i^{\mathrm{A}} + L^{\mathrm{B}} x_i^{\mathrm{B}} \quad (i = 1, 2, \ldots, C) \qquad (3)$$

where x_i, y_i, P and P_i^S denote the mole fraction of component i in liquid phase, that in vapor phase, the total pressure and saturated vapor pressure of component i. Thermodynamic equations consist of two parts: vapor - liquid equilibrium part and liquid - liquid equilibrium part, and overall equation shows vapor - liquid - liquid equilibrium. The UNIFAC thermodynamic model and Antoine equation were applied estimating the activity coefficient, γ_i, and saturated vapor pressure of component i, P_i^S.

Table 1 Mass fraction of component *i* in AO

Nitrogen heterocyclic compounds			Homocyclic hydrocarbons etc.				
Q	IQ	IL	N	1MN	2MN	BP	DBF
0.07	0.02	0.04	0.03	0.10	0.24	0.06	0.10

2.2. Result

2.2.1 Liquid-liquid equilibrium

The two liquid phases region in quaternary system is shown in **Fig.1**. For example, solvent extraction calculation was carried out with the conditions in **Table 2**, and extract phases on tieline were obtained. **Table 3** shows composition of feed, solvent, and extract phase.

Table 2 Calculation connditions for solvent extraction

Feed		model AO
Solvent		three type of methanol aqueous solution
Mass ratio of solvent to feed, *S/F*	[-]	1
Pressure, *P*	[atm]	1
Temperature, *T*	[K]	293

Table 3 Composition of feed, solvent and extract phase

	feed	solvent			extract phase		
		solA	solB	solC	extA	extB	extC
Q	0.197	—	—	—	0.0181	0.040	0.06
2MN	0.803	—	—	—	0.0003	0.003	0.02
M	—	0.3	0.5	0.7	0.2635	0.442	0.61
W	—	0.7	0.5	0.3	0.7181	0.515	0.31

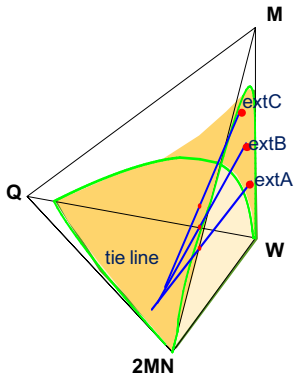

Fig.1 Phase diagrams at 293K and 1atm

2.2.2 Vapor-liquid and vapor-liquid-liquid equilibrium

Vapor-liquid and vapor-liquid-liquid equilibrium are

difficult to present in tetrahedral coordinate like **Fig.1**, so that it is discussed by using **Fig.2**. These graphs show effect of temperature on phase equilibrium, and average compositions in each graph were fixed in the composition of extA, extB and extC. In the figure, result of only Q and W are shown. When temperature was lower than boiling point, there was one liquid phase. In area b, there were vapor and liquid phases. In all case, liquid phase was water phase. In area c, there were one vapor and two liquid phases. In the case of when water content was relatively high such as extA, this tree phases region was narrow. In area d, there were vapor liquid and liquid phases. In the case of extA, liquid phase was water phase. On the other hand, In the cases of extB and extC, liquid phase was oil phase. In area e, there is one vapor phase.

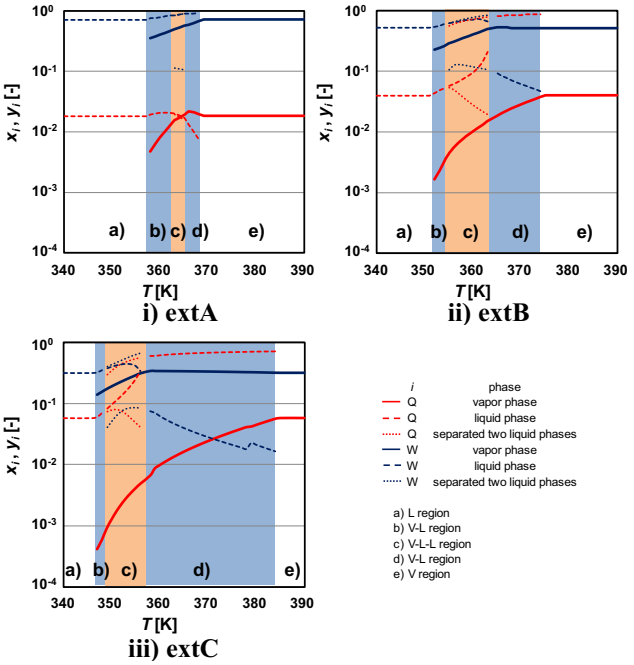

Fig.2 Effect of temperature on phase equilibrium

3. Batch simple distillation of AO and solvent mixture

3.1. Experimental

The experimental conditions are shown in **Table 4**. The real extract phase and model extract phase and were used as feeds for the distillation. The composition of these feeds are shown in **Table 5**. The data of RunNo1~6 were from previous study[2].

3.2. Result

The still liquids consisted of two immiscible liquid phases at higher temperature in the cases of RunNo1, 2, 10, and 11.In this run, the content of Q in the feed for the distillation was relatively high.

Figure 3 shows mass fraction in each phase in RunNo6 and 10. In these graph, effect of temperature on phase equilibrium that average composition fixed in extA and extC are shown also. Feed in RunNo6 and extA had near water and methanol content, and feed in RunNo10 and extC had near water and methanol content. If compare the change of mass fraction with increment of temperature in RunNo6 with phase equilibrium, they had same tendency of increment. But the orders of mass fraction of Q in RunNo6 were different from that in the case of extA, and it was due to difference of feed composition. As result, phase equilibrium by calculation was confirmed qualitatively.

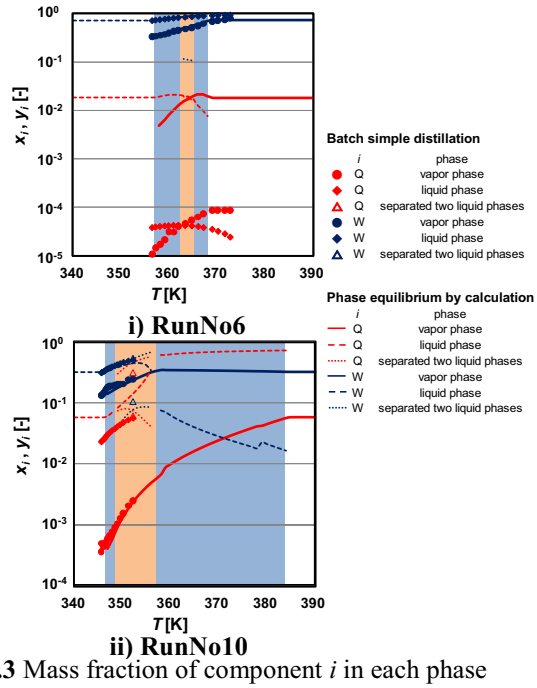

Fig.3 Mass fraction of component *i* in each phase

Based on these results, two flows for solvent recovery were proposed (**Fig.4**). One is that bottom product consist one liquid phase. Solvent components are recovered as top product, and bottom product become nitrogen heterocyclic compounds product. But when water content in extract phase is high, this flow can't be applied because bottom product becomes pure water. The other is that bottom product is separated into aqueous phase and organic phase. Solvent components are recovered as the mixture of top product and aqueous phase. Organic phase become nitrogen compounds product.

Table 4 Experimental conditions of batch simple distillation

Mass, *F*	[kg]	0.05-0.06
Sampling interval	[min]	3
Distillation time	[min]	45
Initial temperature	[K]	room temperature

Table 5 Mass fraction of component *i* in extract phase

Run No	1	2	3	4	5	6	7	8	9	10	11
	real	real	real	model	model	model	model	model	model	model	model
Q	0.0237	0.0105	0.00278	0.006	0.0007	0.00004	0.006	0	0.007	0.022	0.042
IQ	0.0057	0.0025	0.00063	—	—	—	—	—	—	—	—
IL	0.0088	0.0025	0.00050	—	—	—	—	—	—	—	—
N	0.0015	0.0002	0.00001	—	—	—	—	—	—	—	—
1MN	0.0033	0.0004	0.00003	—	—	—	—	—	—	—	—
2MN	0.0077	0.0008	0.00003	0.006	0.0007	0.00003	0	0.006	0.003	0.007	0
BP	0.0022	0.0003	0.00003	—	—	—	—	—	—	—	—
DBF	0.0028	0.0003	0.00002	—	—	—	—	—	—	—	—
M	0.658	0.535	0.315	0.730	0.5417	0.30647	0.664	0.664	0.654	0.655	0.641
W	0.291	0.442	0.697	0.258	0.4568	0.69347	0.330	0.331	0.336	0.316	0.317

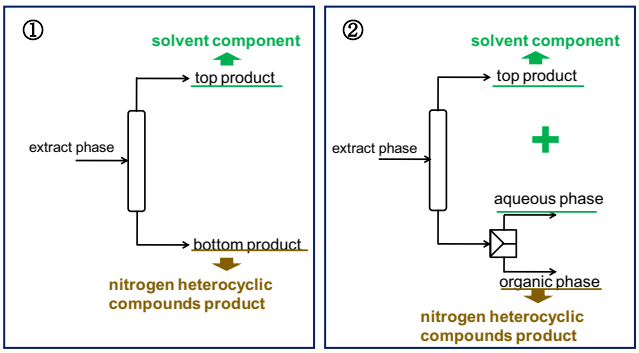

Fig.4 Schematic diagram of flow for solvent recovery

4. Process of AO separation

4.1 Process scheme

The schematic flow sheet of AO separation process is shown in **Fig.5**. The AO is separated roughly into nitrogen heterocyclic compounds and other compounds by using solvent extraction with methanol aqueous solution. Single-stage extraction was applied. Next, the solvent components in extract phase are recovered by distillation and nitrogen heterocyclic compounds product is obtained. For this distillation, multi-stage distillation was applied.

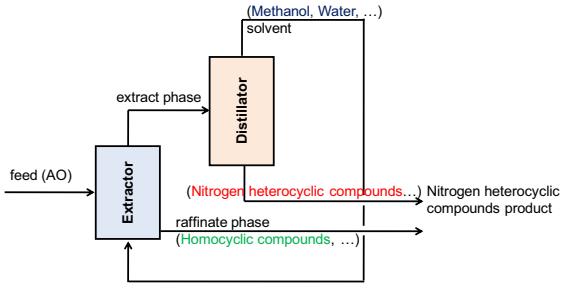

Fig.5 Schematic diagram of AO separation process

4.2 Calculation

4.2.-1 Solvent extraction

Single-stage extraction was carried out with same conditions in chapter 2 (**Table 2**), and extA, extB and extC were used as feed of following distillation.

4.2.-2 Distillation

This calculation was conducted by the commercial process simulator *CHEMCAD III*. **Table 6** shows the calculation conditions of the distillation. Thermodynamic model was same as that in previous chapter. The conditions and specifications of distillation calculation are summarized in **Table 7**.According to the process suggestions in chapter3, three kinds of cases were examined.

Table 6 Calculation conditions of distillation

Number of stages		15
Condenser		total condenser
Extract phase flow rate, F	[kg]	1
Pressure, P	[atm]	1
Feed		liquid at boiling point
Feed stage,n_F		min$\lvert T_F - T_{n_F} \rvert$

Table 7 Specifications in each Case

	Spec 1	Spec 2
Case1	$D = Fz_M$	$Wx_M < 1\times10^{-4}$
Case2	$D = Fz_M + Fz_W$	reflux ratio, R = 1
Case3	$Wx_W < 1\times10^{-4}$	reflux ratio, R = 1

4.3 Result

The results are shown in **Table 8**. In RunNoA2 and A3, solvent recovery was not achieved. In RunNoA2, bottom product became pure water as expected, and A3, specification could not be satisfied. In Case1 or 2, solvent recovery was achieved by flow②. On the other hand, in Case3, that was achieved by flow①.

Table 8 Result of each RunNo

RunNo	Case	ext	Solvent recovery
A1	1	A	②
B1	1	B	②
C1	1	C	②
A2	2	A	×
B2	2	B	②
C2	2	C	②
A3	3	A	×
B3	3	B	①
C3	3	C	①

Mass fraction

Figure 6 shows the mass fractions in top product and nitrogen compounds product. In Case3, water was not contained in the nitrogen heterocyclic compounds product. On the other hand, when applied Case1 or 2, it is inevitable that water was contained in the nitrogen compounds product with amount of solubility. The products that extracted component content was over 90% were obtained.

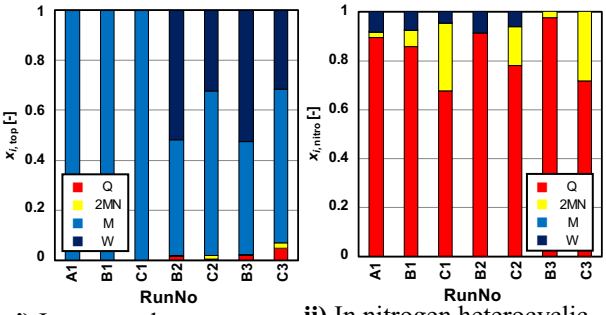

i) In top product, $x_{i,\mathrm{top}}$ **ii)** In nitrogen heterocyclic compounds product, $x_{i,\mathrm{nitro}}$

Fig.6 Mass fraction of component *i* in top product and nitrogen heterocyclic compounds product

Yield

Figure 7 shows the yield in top product and nitrogen compounds product. In Case1, $Y_{\mathrm{2MN,nitro}}$ was larger than $Y_{\mathrm{Q,nitro}}$. It is due to small solubility of 2MN in the aqueous phase. On the other hand, in Case2 or 3, $Y_{\mathrm{Q,nitro}}$ was larger than $Y_{\mathrm{2MN,nitro}}$ because 2MN was contained in top product. Further separation between nitrogen compounds and the others was occurred.

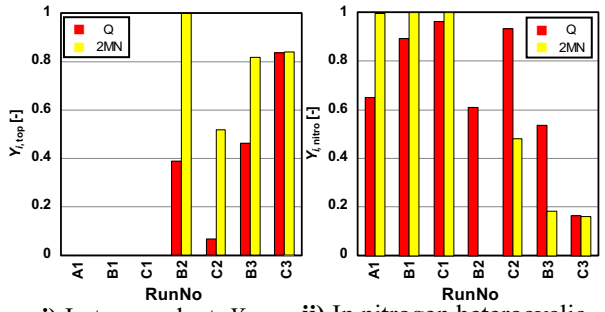

i) In top product, $Y_{i,\mathrm{top}}$ **ii)** In nitrogen heterocyclic compounds product, $Y_{i,\mathrm{nitro}}$

Fig.7 Yield of component *i* in top product and nitrogen heterocyclic compounds product

Energy requirement (reboiler duty)

Figure 8 shows the energy requirement that is equal to reboiler duty in the each run. The energy requirement in Case3 was higher than that in Case1 or 2. In addition, the range of distillation temperature in Case3 was very wide. In Case1 and 2, the highest temperature in the column was about 372K, but that in Case3 was about 510K.

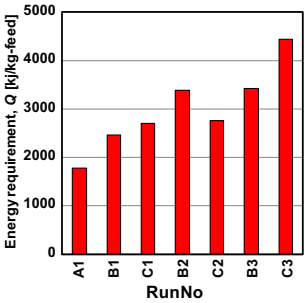

Fig.8 Energy requirement, *Q*

When water content in extract phase is low such as extC, Case2 shows high purity, further separation between Q and 2MN and low energy requirement. When water content in extract phase is high such as extA, it is necessary to select Case1 because bottom product became pure water so solvent recovery can't be achieved in Case2 or 3.

4. Conclusions

First, by calculation of phase equilibrium, it was confirmed that when water content in feed was high vapor-liquid-liquid three phases region was small and liquid phase was water at high temperature. On the other hand, when water content was low, liquid phase was oil. Next, by batch simple distillation, phase equilibrium by calculation was confirmed qualitatively. Based on the result of phase equilibrium estimation and batch simple distillation, two type of solvent recovery were proposed. Finally, process of AO separation was estimated and accessed, and AO separation and solvent recovery were achieved.

Acknowledgment

The author wish to thank JFE Chemical Co., Ltd. for providing coal tar absorption oil.

Nomenclatures

C	= number of components	[-]
D	= mass of distillate	[kg]
E	= mass of extract phase	[kg]
F	= mass of feed	[kg]
L	= mole of liquid phase	[mol]
Q	= energy requirement	[kj/kg-feed]
R	= reflux ratio	[-]
S	= mass of extraction solvent	[kg]
V	= mole of vapor phase	[mol]
W	= mass of bottom product	[kg]
x	= mole or mass fraction in liquid phase	[-]
y	= mole or mass fraction in vapor phase	[-]
z	= mole or mass fraction in feed	[-]
Y	= yield	

<Greek>

γ	= activity coefficient	[-]

<Subscript>

1MN = 1-methylnaphthalene
2MN = 2-methylnaphthalene
AO = absorption oil
BP = biphenyl
D = distillate
DBF = dibenzofuran
E = extraction solvent
F = feed
i = component *i*
IL = indole
IQ = isoquinoline
N = naphthalene
nitro = nitrogen heterocyclic compounds product
Q = quinoline
top = top product

<Superscript>

A = liquid phase A
B = liquid phase B
S = saturated vapor

Literature Cited

[1] Salim. C, Egashira. R; *Journal of the Japan Petroleum Institute*, **49**, (6), 326 (2006)
[2] Yoshimura.Y; Bachelor thesis, Tokyo Tech (2008)

FUTURE ESTIMATION OF THE AIRCRAFT CO_2 EMISSIONS FOR FLIGHTS BETWEEN JAPAN, CHINA AND SOUTH KOREA

Student Number: 08M18186 Name: Ying QIAO Supervisor: Shinya HANAOKA

日中韓路線に就航する航空機からの CO_2 排出量の将来推定

喬 顥

本論文では、航空機からの CO_2 排出量を高い精度で推定するため、日中韓間の国際直行便に着目し、2008 年の CO_2 排出量を路線別に算出した。Grey 予測モデルにより、2020 年の同じ路線の航空旅客需要を予測し、航空機の機材サイズが同じ構成であると仮定して、CO_2 排出量を推定した。また、機材サイズを変更した時の CO_2 排出量の変化を分析した。

1. Introduction

In current years, with the development of socio-economic globalization, international trade and tourism using air transport have been becoming increasingly common. In the mean time, the issue of CO_2 emission caused by the phenomenon deserves our serious consideration. The latest surveys show that the amount of CO_2 emission in aviation sector has contributed to for approximate 2.5%~3% [1] of the world's total amount. In addition, it is estimated that the air transport passenger traffic will show a growth trend in the future [2], which likely increase CO_2 emission and arouse adverse impacts. Thus, it is important to explore how to predict the future CO_2 emission of aircraft and how to adopt some efficient methods to decrease the emissions.

So far, different nations have varied attention degrees to research the CO_2 emission of aircraft. Europe and North America conducted a large number of researches in relation to calculating the current CO_2 emission of aircraft and predicting the future trend. Also, they formulated related plans to limit CO_2 emission from civilian aircraft. Asian countries, however, spent less resource in studying CO_2 emission of aircraft. Recently, along with the economic and trade development, the demand for aircraft in some Asian countries led by China is becoming increasingly large. Based on the data from ICAO (International Civil Aviation Organization), the average growth rate of demand for aircraft in Asia is 6.1% from 2002 to 2015, which is larger than that of world average growth rate (4.4%). With unpredictable future trend of the Asian aviation market, the air transport demands are expected to rapidly increase, as well as CO_2 emissions. Therefore, should be useful for Asia to research on CO_2 emission of aircraft.

Some researches for CO_2 emission of aircraft aimed at the world's flights. There is few research for focusing on specific regions or some individual routes.

This paper selects the three economic growth nations in North Asia, Japan, China and Korea, as the target to analyze the current situation and future trends. Firstly, based on the aircrafts of international direct flights among these nations, the amount of CO_2 emissions is obtained in 2008. Secondly, by forecasting the passenger traffic for aircraft of 2020, CO_2 emissions in 2020 is approximately estimated. Finally, this paper analyzes the impacts of changing the aircraft size on CO_2 emissions.

2. Estimation of current CO_2 emission

2.1 Basic concepts

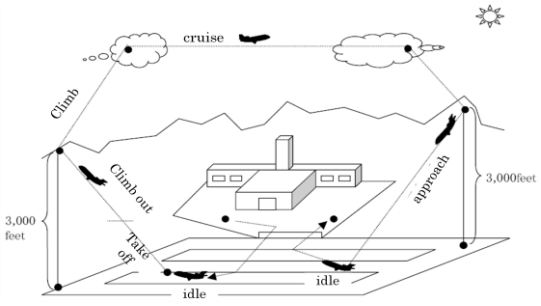

Figure1. The concept sketch map of each steps during the process of flight

Note：1 feet=0.3048m, 3000 feet equals to 914.4m.

Source: CO_2 Emissions from Fuel Combustion (2004)

There are two phases of flights needed to be taken into account for calculating aircraft CO_2 emission, i.e. cruise and LTO (Landing and Take Off) cycle. When the aircraft flies at the height of 3000ft above, it is called cruise. The rest of the stages is called LTO cycle, which includes 4 modes. They are take off, climb out, approach, and idle mode. Figure 1 shows the conceptual

sketch of each step during the process of flight.

2.2 Data collection

The data for calculating CO_2 emission are obtained from OAG (Official Airline Guide) time table, LTO cycle Engine Emission Data from ICAO and BADA (Base of Aircraft Data) from Euro Control Experimental Center. At first, international direct flights between China, Japan, and Korea are extracted from OAG time table, including 112 flights between China and Japan, 78 flights between China and Korea, 68 flights between Japan and Korea. They are shown in Table 1. In addition, all aircraft type of each flight, arrival and departure time, and flight frequency per week can be found. Secondly, 4 modes time of LTO cycle referred to ICAO provision, i.e. take off 0.7 min, clime out 2.2 min, approach 4 min, and idle 26 min. Therefore, the flight cruising time can be calculated by subtracting LTO time from the whole flight time (the differences between arrival time and departure time).The transit flights are not considered in this research.

Concerning each mode fuel flow of LTO cycle of each aircraft model, the engine data of corresponding aircraft type can be extracted, which are used in direct flights between China, Japan and Korea, from 2005 Jet Engine Specification Database of Home of the X-Plane Flight Simulator Community. Afterwards each mode fuel flow of LTO cycle of corresponding engine will be obtained from ICAO Aircraft Engine Emissions Databank of 2008 version. From BADA, the fuel flow at maximum altitude is selected as the cruising fuel flow of each aircraft model.

Table1. Flights between China, Japan and Korea

Flights					
round flights between China and Japan		round flights between China and Korea		round flights between Japan and Korea	
Beijing-Fukuoka	Qingdao-Nagoya	Busan-Beijing	seoul-hangzhou	Akita-Seoul	Nagoya-Seoul
Beijing-Nagoya	Qingdao-Osaka	Busan-Guangzhou	Seoul-Jinan	Aomori-Seoul	Niigata-Seoul
Beijing - Osaka	Qingdao-Tokyo	Busan-Hangzhou	Seoul-Kunming	Asahikawa-Seoul	Oita-Seoul
Beijing to Sapporo	Shanghai-Fukuoka	Busan-Qingdao	Seoul-Mudanjiang	Fukuoka-Busan	Okayama-Seoul
Beijing - Tokyo	Shanghai-Fukushima	Busan-Shanghai	Seoul-Nanjing	Fukuoka-Jeju	Okinawa-Seoul
ChangChun-Nagoya	Shanghai-Hiroshima	Busan-Shenyang	Seoul-Qingdao	Fukuoka-Seoul	Osaka-Busan
ChangChun-Sendai	Shanghai-Kagoshima	Busan-Weihai	Seoul-Sanya	Fukushima-Seoul	Osaka-Jeju
ChangChun-Tokyo	Shanghai-Komatsu	Busan-yanji	Seoul-Shanghai	Hakodate-Seoul	Osaka-Seoul
Dalian-Fukuoka	Shanghai-Moriyama	Chongqir-Beijing	Seoul-Shenyang	Hiroshima-Seoul	Sapporo-Busan
Dalian-Hiroshima	Shanghai-Nagasaki	Chongqir-Shanghai	Seoul-Shenzhen	Kagoshima-Seoul	Sapporo-Seoul
Dalian-Nagoya	Shanghai-Nagoya	Jeju-Beijing	Seoul-Tianjin	Komatsu-Seoul	Sendai-Seoul
Dalian to Okayama	Shanghai-Niigata	Jeju-Shanghai	Seoul-Urumqi	Kumamoto-Seoul	Takamatsu-Seoul
Dalian-Osaka	Shanghai-Okayama	Seoul-Beijing	Seoul-Weihai	Matsuyama-Seoul	Tokyo-Busan
Dalian to Sapporo	Shanghai-Okinawa	Seoul-Changchun	Seoul-Wuhan	Miyazaki-Seoul	Tokyo-Jeju
Dalian-Sendai	Shanghai-Osaka	Seoul-Changsha	Seoul-Xiamen	Nagasaki-Seoul	Tokyo-Seoul
Dalian-Tokyo	Shanghai-Sapporo	Seoul-Chengdu	Seoul-XiAn	Nagoya-Busan	Toyama-Seoul
Dalian-Toyama	Shanghai-Sendai	Seoul-Dalian	Seoul-Yanji	Nagoya-Jeju	Yonago-Seoul
Fuzhou to Osaka	Shanghai-Tokyo	Seoul-Guangzhou	Seoul-Yantai		
Guangzhou-Fukuoka	Shanghai-Toyama	Seoul-Guilin	Seoul-Zhengzhou		
Guangzhou-Nagoya	Shenyang-Fukuoka	Seoul-Harbin			
Guangzhou-Osaka	Shenyang to Nagoya				
Guangzhou-Tokyo	Shenyang-Osaka				
Hangzhou-Osaka	Shenyang-Tokyo				
Hangzhou-Tokyo	Tianjin-Nagoya				
Harbin-Niigata	Xiamen-Osaka				
Harbin-Osaka	Xiamen-Tokyo				
Nanjing-Osaka	XiAn-Tokyo				
Qingdao-Fukuoka	Yantai-Osaka				

2.3 CO_2 emission calculation method

By using Equations 2.1, 2.2 and 2.3, can calculate the CO_2 emission of all airlines between China, Japan, and Korea in 2008. Equation 2.1 and 2.2 are used to calculate the LTO cycle CO_2 emission and cruising CO_2 emission of each flight respectively. Equation 2.3 describes the method of calculating the total CO_2 emission for each airline.

Table2. The fuel flow of aircraft type

No	code	Aircraft Type	Engine Identification	Fuel Flow (kg/sec)					No.of Engine
				cruising	take off	climb out	approarch	idle	
1	310	A310 All Series	A310-304	1.093	2.152	1.771	0.590	0.192	2
2	319	A319	A319-111	0.565	1.051	0.862	0.291	0.101	2
3	320	A320	A320-200	0.633	1.051	0.862	0.291	0.101	2
4	321	A321	A321-231	0.725	1.331	1.077	0.377	0.138	2
5	330	A330	A330-343X	1.200	2.767	2.246	0.724	0.228	2
6	332	A330-200	A330-243	1.470	2.767	2.246	0.724	0.228	2
7	333	A330-300	A330-343X	1.200	2.767	2.246	0.724	0.228	2
8	343	A340-300	A340-300	1.595	1.373	1.131	0.370	0.120	4
9	346	A340-600	A340-600	1.988	2.240	1.830	0.620	0.230	4
10	733	B737-300	B737-300	0.617	0.946	0.792	0.290	0.114	2
11	737	B737 All Series	B737-300	0.620	1.245	0.997	0.354	0.147	2
12	738	B737-800	B737-600	0.617	1.103	0.910	0.316	0.109	2
13	739	B737-900	B737-900	0.617	1.221	0.999	0.388	0.113	2
14	744	B747-400	B747-400	1.988	2.647	2.085	0.703	0.213	4
15	752	B757-200	B757-200	0.967	1.800	1.470	0.540	0.200	2
16	757	B757 All Series	B757-200	0.967	1.800	1.470	0.540	0.200	2
17	763	B767-300	B767-300ER	1.147	2.127	1.757	0.600	0.198	2
18	767	B767 All Series	B767-300ER	1.147	2.127	1.757	0.600	0.198	2
19	772	B777-200	B777-200	1.647	3.100	2.570	0.880	0.280	2
20	773	B777-300	B777-300	1.617	3.515	2.844	0.917	0.304	2
21	777	B777 All Series	B777-200	1.647	3.100	2.570	0.880	0.280	2
22	73G	B737-700	B737-700	0.592	0.913	0.761	0.274	0.100	2
23	73H	B737-800WL	B737-800	0.617	1.103	0.910	0.316	0.109	2
24	74E	B747-400C	B747-400	1.988	2.647	2.085	0.703	0.213	4
25	74L	B747SP	B747SP	1.977	2.429	1.880	0.659	0.224	4
26	AB6	A300-600	A300B4-622R	1.265	2.400	1.953	0.636	0.199	2
27	M90	MD-90	MD-90-30	0.760	1.209	0.996	0.353	0.134	2

$$Q_{\text{LTOcycle}} = \sum \left(\begin{pmatrix} \text{each mode fuel flow in LTO cycle} \end{pmatrix} \times (\text{mode time}) \times (\text{engine number}) \right) \times f \quad (2.1)$$

$$Q_{\text{cruising}} = (\text{cruising time}) \times (\text{cruising fuel flow}) \times f \quad (2.2)$$

f: $CO_2 EI(Emission\ \ Index)(3.15kg - CO_2 / kg - Fuel)$

$$Q_{2008} = \sum \left(Q_{\text{LTOcycle}} + Q_{\text{cruising}} \right) \times freq \times 52week \quad (2.3)$$

$freq$: frequency per week

2.4 Result

The total CO_2 emission of international flights among these three nations is 4353.0 thousand tons. China-Japan flights has the largest proportion which accounts for 45.76%, 1992.0 thousand tons, while Japan-Korea flights accounts for 28.96%, 1261.0 thousand tons, and China-Korea flights accounts for 25.28%, 1100.0 thousand tons.

3. CO_2 emission forecast in 2020

It is required to forecast the aircraft passenger traffic before forecasting the CO_2 emission in 2020.

3.1 Passenger traffic forecast

When forecasting passenger traffic, it is essential to consider about how to choose the forecasting model and select the sample data. Since external factors makes a great impact on this forecast, such as the development of socio-economic development, natural disasters, it makes passenger sample data became fluctuated. In addition, limited valid data sample was provided in air transport field. According to the feature of aircraft passenger traffic forecast, this paper selected the Grey Theory Model — GM (1,1) forecasting model[3].

Usually, GM (1,1) model requires less

sequential data, and, thus, it satisfies data limitation in forecasting aircraft passenger traffic. Generally, 4 or 5 years of time series data are used.

3.2 Formulation of GM (1,1) model

Given there are n samples of a series, X(0)={X(0)(1), X(0)(2), X(0)(3), …, X(0)(n)}。

Step1: Do AGO (Accumulated Generating Operation) once through Equation 3.1. A new series is obtained like $X^{(1)}$={$X^{(1)}$(1), $X^{(1)}$(2), $X^{(1)}$(3), …, $X^{(1)}$(n)}.

$$X^{(1)}(k)=\sum_{m=1}^{k}X^{(0)}(m) \quad (3.1)$$

Step2 : The establishment of differential Equation 3.2

$$\frac{dX^{(1)}}{dt}+aX^{(1)}=b \quad (3.2)$$ (a,b :unknown coefficient)

Step3 : Given $\hat{a}=\begin{bmatrix}a\\b\end{bmatrix}$, calculate $\hat{a}$ utilizing least-squares method.

$$\hat{a}=(B^TB)^{-1}B^TY_n \quad (3.3)$$

Here, $B=\begin{bmatrix}-\frac{1}{2}\left[X^{(1)}(1)+X^{(1)}(2)\right] & 1\\ -\frac{1}{2}\left[X^{(1)}(2)+X^{(1)}(3)\right] & 1\\ \vdots & \vdots\\ -\frac{1}{2}\left[X^{(1)}(n-1)+X^{(0)}(n)\right] & 1\end{bmatrix}$ $Y_n=\begin{bmatrix}X^{(0)}(2)\\X^{(0)}(3)\\\vdots\\X^{(0)}(n)\end{bmatrix}$

Step4: Substitute a, b into differential Equation 3.2, obtain forecasting model

$$\hat{X}^{(1)}(i+1)=\left[X^{(0)}(1)-\frac{b}{a}\right]e^{-ai}+\frac{b}{a} \quad (3.4)$$

$\hat{X}^{(1)}(i+1)$ is forecasting model of $X^{(1)}$.

Step5 : Do IAGO(Inverse Accumulated Generating Operation) once to forecasting model $X^{(1)}(i+1)$, obtain the forecasting model of original series $X^{(0)}$

$$\hat{X}^{(0)}(i+1)=\hat{X}^{(1)}(i+1)-\hat{X}^{(1)}(i) \quad (3.5)$$

3.3 Model residual test

After solving the forecasting value, it is required to do residual test for examining the accuracy of forecasting models. Through Equations 3.6, 3.7and 3.8, the value of average relative residual can be obtained.

A) Residual: $\varepsilon^{(0)}(i)$

$$\varepsilon^{(0)}(i)=X^{(0)}(i)-\hat{X}^{(0)}(i) \qquad i=1,2,3\cdots,n \quad (3.6)$$

B) Relative residual: $e^{(0)}(i)$

$$e^{(0)}(i)=\frac{\varepsilon^{(0)}(i)}{X^{(0)}(i)}\times 100\% \qquad i=1,2,3\cdots,n \quad (3.7)$$

C) Average relative residual: $e^{(0)}(avg)$

$$e^{(0)}(avg)=\frac{1}{n}\sum_{i=1}^{n}\left|e^{(0)}(i)\right| \quad (3.8)$$

Average relative residual is classified into 4 levels to identify the accuracy of model. The detail criteria are shown in Table 3.

Table 3 GM (1,1)forecasting model accuracy

Average relative residual domai	Accuracy
$e^{(0)}(avg)<=0.1$	excellent
0.1<e(0)(avg)<=0.2	good
0.2<e(0)(avg)<=0.5	acceptable
e(0)(avg)>0.5	unacceptable

3.4 Data

TFS Module (Traffic by Flight Stage) from ICAO data will be adopted. Considering wide fluctuation in passenger traffic, make predictions based on the latest information that is the passenger data from year 2004 to 2008. The database includes passenger data within five years, less than five year and transit flights in 258 flights between China, Korea and Japan. Passenger data, more than 3 years, make forecast based on GM (1, 1) model. For 3 and 2 years passenger data, make use least of square and first-order linear equation method respectively. The data processing of module GM (1,1) utilizes numerical analysis software MATLAB R2007b.

3.5 Results of passenger traffic forecast

This paper makes predictions on passengers of 258 airlines. In 2020, passengers will be 1.086×10^7 between Japan and China, 1.59 times that of 2008(0.684×10^7). Between Japan and Korea, passenger will increase to 1.450×10^7, 1.68 times of 2008(0.864×10^7). And passengers will be 3.551×10^7 between China and Korea, 4.86 times of 2008(0.731×10^7). The total passenger will be 6.087×10^7 between three nations, 2.67 times that of 2008(2.279×10^7).

3.6 CO_2 emission in 2020

By assuming the aircraft type and flight time in year 2020 are the same with those in year 2008, all kinds of fuel flow remains unchanged. In other words, only flight frequency per year changes while CO_2 emission for each flight remains the same compared with those in 2008. So for each flight, the amount of CO_2 emission is proportional to passengers. From Equation 3.9, and 3.10, the CO_2 emission in year 2020 can be calculated.

$$\frac{\text{airline passenger}_{2020}}{\text{airline passenger}_{2008}}=\frac{\text{airline frequency}_{2020}}{\text{airline frequency}_{2008}}$$
$$=\frac{(Q_{\text{cruising}}+Q_{\text{LTO}})\times\text{total frequency}_{2020}}{(Q_{\text{cruising}}+Q_{\text{LTO}})\times\text{total frequency}_{2008}}=\frac{\text{CO2 emission}_{2020}}{\text{CO2 emission}_{2008}} \quad (3.9)$$

$$Q_{2020}=\frac{\text{passenger of each airline}_{2020}}{\text{passenger of each airline}_{2008}}\times Q_{2008} \quad (3.10)$$

The total CO_2 emission is about 9709 thousand tons from flights between China, Korea and Japan,

approximately 2.23 time that of 2008(4,353 thousand tons).

4. The effect on the CO_2 emission by changing aircraft size

Adopt simulation changing the size of the aircraft to evaluate the effect on the CO_2 emission, and use the sample of those flights with large type aircraft and the demand for more than 100 thousand passengers in 2008. Specifically, there are two cases involved: large type aircraft to medium size, and large to small size. It is assumed that the seat load factors are 70% for each flight and no new models of aircraft are adopt since then to 2020. Based on the result of calculation number of standard seating by using TFS data, the aircrafts can be classified into three types: large type with more than 300 seats; medium type with 150 to 300 seats and small type with less than 150 seats. There are total 28 flights are adapted: 6 flights between Japan and China, 8 flights between Japan and Korea, 14 flights between China and Korea, which are showed on the Table 4 below:

Table4. The extracted flights between China, Japan and Korea

Flights			
Beijing–Tokyo	Tokyo–Beijing	Seoul–Guangzhou	Beijing–Busan
Guangzhou–Tokyo	Tokyo–Guangzhou	Seoul–Beijing	Beijing–Seoul
Shanghai–Tokyo	Tokyo–Shanghai	Seoul–Qingdao	Guangzhou–Seoul
Seoul–Fukuoka	Fukuoka–Seoul	Seoul–Shanghai	Qingdao–Seoul
Seoul–Nagoya	Nagoya–Seoul	Seoul–Shenyang	Shanghai–Seoul
Seoul–Osaka	Osaka–Seoul	Seoul–Tianjin	Shenyang–Seoul
Seoul–Tokyo	Tokyo–Seoul	Busan–Beijing	Tianjin–Seoul

4.1 Calculation

By taking one flight as an example, the method to calculate CO_2 emission resulted from changing large-sized aircraft (B744) into a medium-sized aircraft (B767) is as follows.

1). Select the large-sized flight, and calculate the frequency in 2008 (F_{2008}) before changing the aircraft size. The predicted frequency of flights in 2020 (F_{2020}) can be calculated through the Equation 4.2 as follows:

$$F_{2008}(\text{Frequency}) = \frac{\text{Revenue Passenger}}{\text{seat} \times \text{load factor}} \quad (4.1)$$

$$F_{2020}(\text{Frequency}) = F_{2008}(\text{Frequency}) \times \frac{\text{Forecasting passenger traffic in 2020}}{\text{Passenger traffic in 2008}} \quad (4.2)$$

2). Calculate the total CO_2 emission for large-sized aircraft Q_{large} based on the Equation 2.3 and the results of F_{2020}.

3). Select one medium-sized aircraft（B767）to replace all the large-sized ones, and all the passengers are transported by using medium-sized aircraft (B767). The number of flight frequency F will be calculated for this medium-sized aircraft through Equation 4.3 as follows:

$$F = \frac{\sum F_{2020}(\text{large - type}) \times \text{model seat} \times \text{load factor})}{\text{medium seat(B767)} \times \text{load factor}} \quad (4.3)$$

4). Based on the result of F calculated from step 3 and the formula of CO_2 emission, the CO_2 emission Q_{medium} of medium-sized aircraft will be calculated. By comparing with the CO_2 emission of large-sized aircraft, calculate the difference for the two CO_2 emissions. Finally, the total difference Q_{change} will be obtained by calculating the sum of CO_2 emission differences from 28 flights.

$$Q_{change} = Q_{large} - Q_{medium} \quad (4.4)$$

4.2 Results

In case 1(changing large-sized aircrafts with medium-sized aircrafts), the CO_2 emission of aircrafts is reduced about 43.06 thousand tons. In case 2 (from large-sized aircrafts to small-sized aircrafts), the CO_2 emission of aircrafts is reduced about 182.45 thousand tons. According to the results identified above, it can be concluded that changing large-sized aircrafts into medium or small ones can reduce CO_2 emission.

5. Conclusion

In this paper, the CO_2 emission in 2008 can be mastered based on the research that used for 258 international direct airlines among China, Japan and Korea. By using GM (1,1) model, it can be predicted the passenger traffic for each flight and calculated the CO_2 emission in 2020, 2.23 times that of 2008. The simulation of changing the size of the aircraft was adopted to evaluate the effect on the CO_2 emission. It has been found that the CO_2 emission can be reduced by using medium or small size aircraft instead of using large type aircraft. This paper does not take account of the case that there are new engine aircrafts model entered in the future. Considering this case, the CO_2 emission forecasting method should make further adjustments.

Reference

[1] Kim, B. et al.: System for Assessing Aviation's Global Emissions (SAGE) Version 1.5: Global Aviation Emissions Inventories for 2000 through 2004. Washington,DC,USA,2005.

[2] Airbus Industrie: Global Market Forecast: The Future of Flying 2006-2025. Airbus S.A.S., Blagnac Cedex, France, 2006

[3] Deng Ju long. Introduction to grey system theory[J]. The journal of Grey System, 1989, 1: 1-24

Numerical Analysis of Micro-Scale Cavity Flow

Student Number: 08M18192　Name: Xin XIN　Supervisor: Yoshihiro MOCHIMARU

キャビティ内すべり流動解析

シンキン

本研究では，ナビエ–ストークス方程式（Navier-Stokes equations, 以降 N-S とする）を支配方程式とし，Kn=0.1~0.001 の範囲で，スリップ流れの境界条件の下で，スペクトル差分法を用いてすべり流動を解析することにより，スペクトル差分法の解析対象範囲の拡大を図ることを目的とする．解析例として，二次元のキャビティ内の非圧縮性ニュートン流体を解析対象として，すべりの境界条件の下，座標変換を行った計算空間にある未知量（流れ関数と渦度）を完備な級数（フーリエ級数）に展開した後，空間上の独立変数を一つ分離し，単一直交格子を形成し支配方程式を一方向のみ離散化して解き，時間進行で定常解を求める．

Key words: numerical simulation, spectral finite difference scheme, wall slip, Navier-Stokes equation

1. Introduction

As the number of applications of micro electro mechanical system (MEMS) increases, flows of micro-channel and micro-cavity to be analyzed are also increasing [1]. The flow in micro-scale shows different behaviors as compared with that in macro-scale. One possible basic step in understanding these processes is numerical study of fluid flow through a micro-scale cavity. In case of a small scale, the continuum approach under no-slip boundary condition is invalid. A dimensionless parameter that determines the degree of appropriateness of the continuum model is a Knudsen number, Kn, which is defined as the ratio of the fluid mean-free-path λ to the macroscopic length scale of the physical system L,

$$Kn = \frac{\lambda}{L} \tag{1}$$

Figure 1 describes different regimes of fluid flows. As Kn increases, rarefaction effect becomes more pronounced and eventually the continuum assumption breaks down.

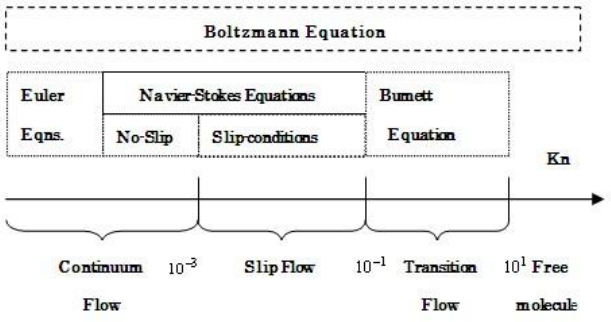

Fig. 1 Knudsen number regimes

The regimes are variable according to different flows. It has been pointed out that for a system with $Kn < 0.001$, the fluid flow can be treated as continuum. For $Kn > 10$ the system can be considered as a free-molecular flow. The fluid flow for $0.001 < Kn < 10$, which often appears in the MEMS [1]. Due to these results, the regime is treated as $0.001 < Kn < 0.1$ and the solution of the Navier-Stokes equation including the velocity-slip boundary condition with the parameter of Kn has been used in this report.

A micro-scale rectangular two-dimensional cavity flow is numerically analyzed with a slip boundary condition, using a spectral finite difference scheme, through a boundary fitted conformal mapping system. A semi-implicit time integration scheme in a diagonal predominant form is applied to get a steady-state solution.

2. Analysis

2.1 Basic Equations

A system of partial differential equations are formulated from a vorticity transport equation in a boundary-fitted conformal coordinate system, where the rectangular region is mapped into a circular region in w for which

$$\exp(\alpha + i\beta) \equiv w = \frac{(1+if)}{(1-if)} \tag{2}$$

where f is an analytic function of $x + iy$ in a Cartesian coordinate (x, y), dimensionless, such that along the closed boundary f is real and varies monotonously from $-\infty$ to $-\infty$ with increasing β. In this case if the said domain is expressed by $-\infty < \alpha \leq 0$, $-\pi < \beta < \pi$, then the governing equations lead to

vorticity transport equation

$$J\frac{\partial \zeta}{\partial t} + \frac{\partial \psi}{\partial \beta}\frac{\partial \zeta}{\partial \alpha} - \frac{\partial \psi}{\partial \alpha}\frac{\partial \zeta}{\partial \beta} = \frac{1}{Re}\left(\frac{\partial^2 \zeta}{\partial \alpha^2} + \frac{\partial^2 \zeta}{\partial \beta^2}\right) \tag{3}$$

Relationship between the stream function and the vorticity is given by

$$J\zeta = -\left(\frac{\partial^2 \psi}{\partial \alpha^2} + \frac{\partial^2 \psi}{\partial \beta^2}\right) \tag{4}$$

together with

$$J = \frac{\partial(x,y)}{\partial(\alpha,\beta)}, \frac{\sqrt{J}}{r} = \frac{2}{|f'||1+w|^2}, r \equiv \exp(\alpha) \tag{5}$$

a : ≡horizontal width of the cavity/π

J : Jacobian

Re : Reynolds number

t : dimensionless time based on a/U
U : $\equiv (\nu/a)\sqrt{Re}$
x, y : Cartesian coordinate system
α, β : elliptic coordinate system
ν : kinematic viscosity of the fluid
ψ : dimensionless stream function U/a
ζ : dimensionless vorticity aU

In general, for a given simply-connected cavity domain, f is not determined uniquely [2]. In the current case, at least the followings (6), (7) are possible:

$$f = \frac{1 + \sum_{n=1}^{\infty} b_n \cos 2nz}{-\sin z} \tag{6}$$

$$b_n = \frac{-2\sinh^2(H)}{\sinh(2n+1)H \sinh(2n-1)H} \tag{7}$$

$$z \equiv x + iy \tag{8}$$

$|x| \le \pi/2, 0 \le y \le H$.
x : horizontal
y : vertically upward
H : dimensionless cavity height

2.2 Formulation by Spectral Finite Difference Scheme

In case of periodic base functions, it is necessary to set up a coordinate system such that the physical quantities are periodic at least along one coordinate.

In order to express the physical quantities and to decompose the governing equations into each spectral component, the following Fourier series is used.

$$\psi(\alpha, \beta, t) = \sum_{k=0}^{\infty} \psi_{ck}(r,t) \cos k\beta + \sum_{k=1}^{\infty} \psi_{sk}(r,t) \sin k\beta \tag{9}$$

$$\zeta(\alpha, \beta, t) = \sum_{k=0}^{\infty} \zeta_{ck}(r,t) \cos k\beta + \sum_{k=1}^{\infty} \zeta_{sk}(r,t) \sin k\beta \tag{10}$$

ψ_{ck} and ψ_{sk}... are the Fourier coefficients, which are the functions of argument r and t.

Jacobian, J, is an even function in this case and also can be decomposed as

$$J(\alpha, \beta) = \sum_{k=0}^{\infty} J_{ck}(\alpha) \cos k\beta \tag{11}$$

Substituting these expressions shown above into the original governing equations (3), (4), gives the following form

$$\sum_{k=0}^{\infty} F_{ck}(r,t) \cos k\beta + \sum_{k=1}^{\infty} F_{sk}(r,t) \sin k\beta = 0 \tag{12}$$

which gives

$$F_{ck}(r,t) = 0 \tag{13}$$

$$F_{sk}(r,t) = 0 \tag{14}$$

The spatial variable β is separated and two systems of simultaneous partial differential equations (with respect to one spatial variable r and dimensionless time t) are obtained.

Vorticity transport equation

$$J_{c0} \frac{\partial \zeta_{cm}}{\partial t} - \frac{1}{Re}\left(\frac{\partial^2 \zeta_{cm}}{\partial \alpha^2} - m^2 \zeta_{cm} \right) = B_{cm} \tag{15}$$

$$J_{c0} \frac{\partial \zeta_{sm}}{\partial t} - \frac{1}{Re}\left(\frac{\partial^2 \zeta_{sm}}{\partial \alpha^2} - m^2 \zeta_{sm} \right) = B_{sm} \tag{16}$$

Relationship between the stream function and the vorticity is given by

$$J_{c0} \zeta_{cm} - \left(\frac{\partial^2 \psi_{cm}}{\partial \alpha^2} - m^2 \psi_{cm} \right) = \mathrm{C}_{cm} \tag{17}$$

$$J_{c0} \zeta_{sm} - \left(\frac{\partial^2 \psi_{sm}}{\partial \alpha^2} - m^2 \psi_{sm} \right) = \mathrm{C}_{sm} \tag{18}$$

Decomposition itself can be executed analytically and the results may be evaluated in terms of numerical integration. In such way, one spatial variable can be separated to give a system of simultaneous partial differential equations.

In the analysis the series is assumed converging asymptotically as a number of terms tends to infinity. The resulting system of simultaneous partial differential equations can be solved by truncating the series up to a certain order (in this study the number of terms equals to 10) and by a finite difference approximation which accepts non-uniform grid spacing a great deal.

2.3 Grid Generation Method

The computational space is discretized by boundary-fitted curvilinear coordinate grid which is also called as structured grid.

Let *max*+2 points distribute on $r(0 \le r \le 1)$ for a line of radius 1 in length of the computational space. r_{max+1} is on the boundary and r_0 is in the centre. They are both allocated explicit. Discretization on the computational space may be made in the following non-uniform grid spacing, that is, the coordinate r_i for the n-th grid point is given by

$$r_i = r_{max+1} - l\left\{ \frac{\sinh[(max - i)\xi]}{\sinh \xi} + 1 \right\} \tag{19}$$

$$l = \frac{\sinh(\xi)}{\sinh(\xi) + \sinh(max \cdot \xi)} \tag{20}$$

Where ξ is a suitable positive constant. This results in substantially doubly-exponentially transformation on the physical space. In the limit $\xi \to 0$ it produces a uniform grid spacing in r.

ξ : grid generation parameter

2.4 Finite-Difference Approximations

Partial derivatives are approximated by using the mesh point.

For time, it is simulated by a forward difference scheme.

$$\frac{\partial F(r,t)}{\partial t} = \frac{F(r, t + \Delta t) - F(r,t)}{\Delta t} \tag{21}$$

For space, they are simulated by central difference scheme with errors of $o(h^2)$.

$$\begin{aligned} \frac{\partial F(r_n, t)}{\partial r} = & \left[\frac{h_{n-1}}{h_n(h_n + h_{n-1})} \right] F(r_{n+1}, t) \\ & + \left(\frac{h_n - h_{n-1}}{h_n h_{n-1}} \right) F(r_n, t) \\ & + \left[\frac{-h_n}{h_{n-1}(h_n + h_{n-1})} \right] F(r_{n-1}, t) \end{aligned} \tag{22}$$

$$\frac{\partial^2 F(r_n,t)}{\partial r^2} = \left[\frac{2}{h_n(h_n+h_{n-1})}\right] F(r_{n+1},t) + \left(\frac{-2}{h_n h_{n-1}}\right) F(r_n,t) + \left[\frac{2}{h_{n-1}(h_n+h_{n-1})}\right] F(r_{n-1},t) \quad (23)$$

h_i : mesh spacing

2.5 Numerical Scheme

As for partial differential equation, analytical solution cannot be obtained because of a non-linear reason except a special case. We can obtain two sets of simultaneous equations (one is for sine the other is for cosine.) by forming the separated equations (15)~(18). The band scheme is adopted to create the coefficient matrices.

The discretized simultaneous equations can be integrated semi-implicitly. Systems of simultaneous algebraic equations are solved with the triangular factorization method (LU decomposition).

2.6 Boundary Conditions

2.6.1 Auxiliary Conditions

Since the point $r \equiv e^{\alpha} = 0$ is by no means a singular point, as a necessary condition the following hold:

$$\frac{\partial \psi_{c0}(r_0,t)}{\partial r} = \frac{\partial \zeta_{c0}(r_0,t)}{\partial r} = 0 \quad (24)$$

$$\psi_{c0}(r_0 = 0, t) = \psi_{c0}(r_1, t) = 0 \quad (25)$$

$$\zeta_{c0}(r_0 = 0, t) = \zeta_{c0}(r_1, t) = 0 \quad (26)$$

2.6.2 Boundary Conditions

At the opening of the cavity, the velocity is assumed to contain only horizontal component. It can be expressed as

$$\frac{1}{\sqrt{J}}\frac{\partial \psi}{\partial \alpha} = 1, \qquad \frac{\partial \psi}{\partial \beta} = 0 \quad (10)$$

Substituting these expressions into the original governing equation (4) which can be written as

$$\frac{\partial^2 \psi}{\partial r^2} = \frac{1}{r^2}\left(-J\zeta - r\frac{\partial \psi}{\partial r}\right) \quad (22)$$

Use a finite number (the 2nd order) of terms of the Taylor series to approximate above function at the point $r = 1$. The following was obtained.

$$\zeta = \frac{r^2}{J}\frac{2}{h^2}\left[-\psi(-h) - h\frac{\sqrt{J}}{r}\right] - \frac{1}{\sqrt{J}} \quad (23)$$

This can be considered as the relation between vorticity and stream function at the opening of the cavity.

On the walls, as postulated by Navier [3], the slip velocity is assumed to be proportional to the wall shear.

$$u_{wall} = \sigma Kn\left(\frac{\partial u}{\partial y}\right)_{wall} \quad (24)$$

Where σ is an accommodation coefficient and in the current case $\sigma = 1$.

It also be expressed by vorticity ζ as

$$u_{wall} = -\frac{1}{\sqrt{J}}\frac{\partial \psi}{\partial \alpha} = Kn\left(\frac{\partial u}{\partial y}\right)_{wall} = -Kn\zeta \quad (25)$$

Summing up

$$\zeta = \begin{cases} \frac{r^2}{J}\frac{2}{h^2}\left[-\psi(-h) - h\frac{\sqrt{J}}{r}\right] - \frac{1}{\sqrt{J}} & \text{(26a) opening} \\ (-h)\frac{1}{Kn}\frac{r}{\sqrt{J}}\psi(-h) & \text{(26b) walls} \end{cases} \quad (26)$$

The Fourier coefficients (both sine and cosine) of ζ can be computed by the integral to (26a) and (26b).

2.7 Initial Conditions

The flow can be supposed stood still at $t = 0$ as an initial condition.

$$\psi_{cn} = 0\ (n = 0, 1, \cdots, N), \psi_{sk} = 0(\ k = 1,2, \cdots, N) \quad (27)$$

$$\zeta_{cn} = 0\ (n = 0, 1, \cdots, N),\ \zeta_{sk} = 0\ (\ k = 1,2, \cdots, N) \quad (28)$$

2.8 Convergence Criterion

2.8.1 Convergence Conditions

The convergence criterion of the solution is executed on the physical space.

The error rate of ε_max by the step as follows are defined as

$$\varepsilon_{\psi_{max}} = \frac{\max|\psi^{t+1}(r,\beta) - \psi^t(r,\beta)|}{|\psi^{t+1}(r^*,\beta^*)|} \le c_\varepsilon \quad (29)$$

$$\varepsilon_{\zeta_{max}} = \frac{\max|\zeta^{t+1}(r,\beta) - \zeta^t(r,\beta)|}{|\zeta^{t+1}(r^*,\beta^*)|} \le c_\varepsilon \quad (30)$$

$*$: superscript at the location where the maximum is given

2.8.2 Time Interval

This analysis requires a convergent solution with semi-implicit time integration scheme. To make the same order between left and right sides in the matrix operations in solving simultaneous equation, the following condition is used

$$\frac{\Delta t}{l^2 \cdot Re} \approx 1 \quad (31)$$

l : grid interval

Δt : time increment

3. Results and Discussion

3.1 Results

Table 1 Parameters

Height	1
Width	π
Grid No.	22
Grid Generation Parameter ξ	2×10^{-1}
Partition of Angle	$\pi/500$

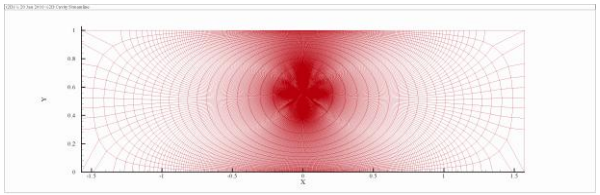

Fig. 2 The boundary-fitted coordinate at grid number=22

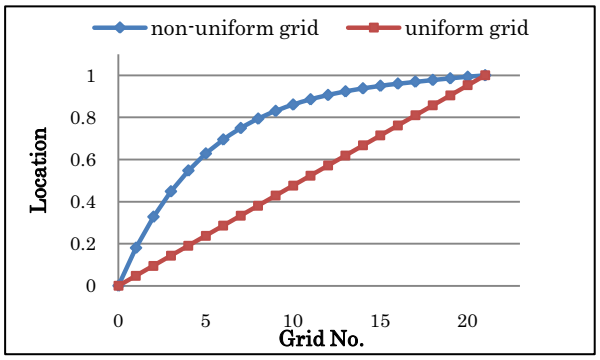

Fig. 3 The grid profile at grid number=22

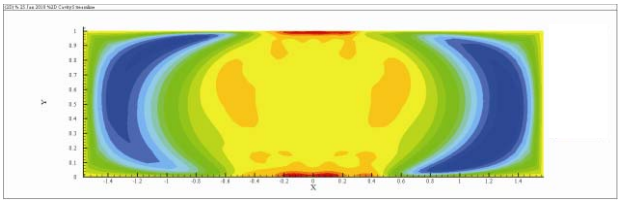

Fig. 4 Steady-state streamlines at Re=1, Kn=1×10^{-2}, Relative Error=3×10^{-4}

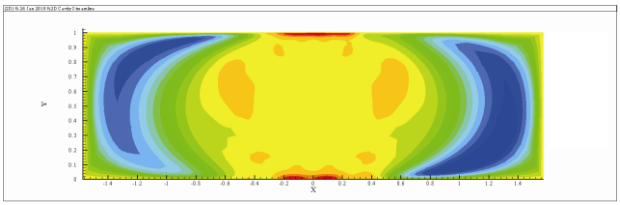

Fig. 5 Steady-state streamlines at Re=1, Kn=1×10^{-1}, Relative Error=3×10^{-4}

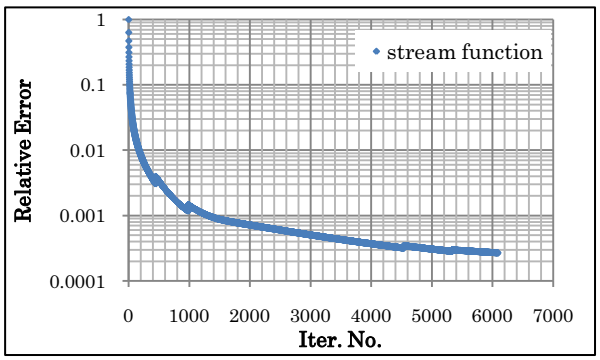

Fig. 6 Relative Error at Re=1, Kn=1×10^{-2}

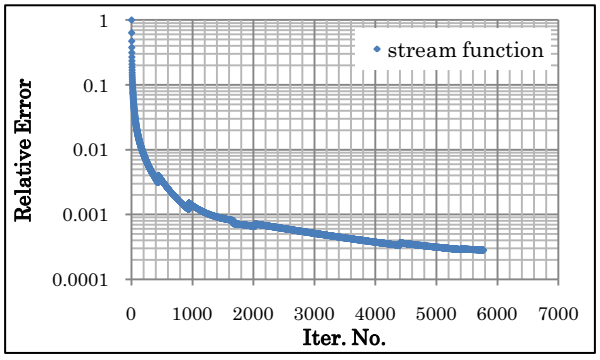

Fig. 7 Relative Error at Re=1, Kn=1×10^{-1}

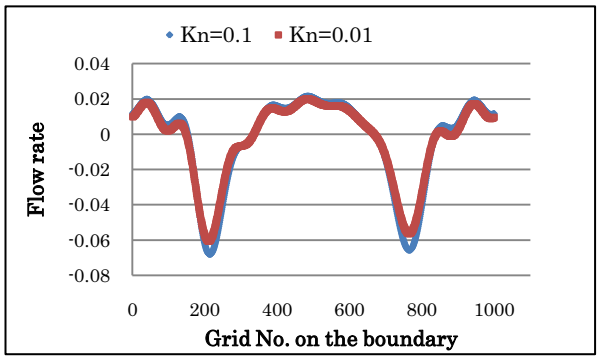

Fig. 8 Comparison of steady-state flow rate at two different Kn

3.2 Discussion

It is understood well that the speed of getting solution is fast enough with the method. This is the feature of the spectral finite difference scheme. However, because the convergence criterion is carried out on the physical space, not the computational space, it took too much time to transform between the two spaces for the criterion

As factors affecting the accuracy of the numerical solution, there are truncation error and discretization error. A Fourier series expanded by trigonometric functions $\{1, \cos nt, \sin nt\ (n = 1, 2, \cdots)\}$ is complete. Both sides are exactly equal to the infinite number of terms. Approximation to N_F finite number of terms causes truncation error. Because higher frequency decreases more sharp and rapidly It has been confirmed that the approximation will converge well when N_F tends to score. In this study, N_F equals to 10. Truncation error in discretization is based on the Taylor series expansion, the present study has the second order accuracy.

4. Conclusion

In this study a micro-scale rectangular two-dimensional cavity flow was numerically analyzed with a slip boundary condition, using a spectral finite difference scheme. Kn ranged from 0.1 to 0.001 under slip flow boundary conditions.

As the results, application of the said method to the slip boundary cavity flow is confirmed. Although the rarefied effect is important in this range, character of the continuum still remains. Therefore, N-S equations are still applicable methods in this case. The phenomenon was found that the flow rate in the boundary layer grows when Kn increasing. We can say that slip effect contributes to the net momentum exchange. These numerical models proved that Kn plays a major role in the slip flow.

5. Reference

1. **C. M. HoC. TaiY.** Micro-electro-mechanical systems (MEMS) and fluid flows. 30 : Ann. Rev. FLuid mech, 1998. 579.

2. **MOCHIMARUYoshihiro.** Effectiveness of a apectral Finite Difference Scheme to Natural Convection. 8th International Symposium on Computational Fluid Dynamics, 1999.

3. **WhiteM.Frank.** VISCOUS FLUID FLOW. p49 : McGRAW-HILL INTERNATIONAL EDITION.

APPLICABILITY OF JOHNSON APPROXIMATION IN AREA ADHESION THEORY

Student Number: 08M18217 Name: KouJen TIEN Supervisor: Kunio TAKAHASHI

面凝着理論における JOHNSON 近似の適用可能条件

田國仁

半無限弾性体が正弦波状の表面粗さを持つ剛体に凝着する際の理論は Rachmat らによって提案されている.この理論から凝着力や凝着幅等を計算するには数値計算が必要となる.しかし,表面粗さの振幅が十分に小さい場合には、解析解が得られる.これは Johnson 近似として知られている.凝着現象を利用した把持・脱離機構等のデバイスを設計するには,数値計算を必要としない Johnson 近似が有用である.しかし,Johnson 近似の適用可能条件についてはまだ詳しく検討されていない.そこで本研究では,Johnson 近似の適用可能条件について理論的に検討した.

1. Introduction

Recently, application of adhesion technology is spreading. The knowledge of adhesion phenomena between solid bodies is important in the design of grip-and-release devices such as removable tapes, bio-mimicking devices, etc… Especially, the effect of the surface roughness of the bodies on the adhesion phenomena of area contact is significant.

Johnson [1] has proposed a theory of area adhesion between a semi-infinite elastic body and a rigid body with a sinusoidal surface roughness. An analytic solution is obtained under the assumption that the height of the sinusoidal roughness is negligibly small. The assumption is called Johnson approximation in the present study.

Rachmat [2] has obtained an analytic solution without using Johnson approximation. However, the numerical computation is required to obtain the adhesion stress as a function of the surface roughness and the work of adhesion.

As the surface roughness decreases, Rachmat's theory approaches asymptotically to Johnson's theory. Rachmat's theory is more suitable for the precise design of the devices. However, Johnson's analytic solution is more convenient in the optimum design of the devices. The applicability of the Johnson approximation is significant, but its applicability is not clearly investigated so far.

In the present study, the applicability of the Johnson approximation is investigated and discussed.

2. Johnson's and Rachmat's theories

2.1 Model used in both theories

Figure 1 shows the schematic illustration of contact model between a semi- infinite elastic body with flat surface and a rigid body with single sinusoidal surface roughness. An external pressure is applied at the infinite position ($y=\infty$). The friction between the bodies is assumed to be negligible. The plain stress is assumed for the elastic body. The wavelength and the wave-height of the rigid body are λ and h_0 respectively.

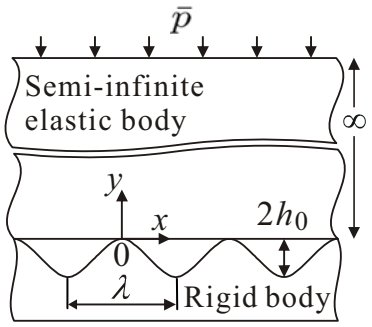

Fig.1. Model of adhesion contact between a semi-infinite elastic body and a rigid body having sinusoidal surface roughness.

2.2 Difference of Johnson's and Rachmat's theories

Equation (1) shows the total energy of Rachmat's theory, E_R and Eq. (2) shows the total energy of Johnson's theory, E_J respectively. The difference between E_R & E_J is in the fourth term that shows the term of the work of adhesion, $\Delta\gamma$ [3][4].

$$E_R = E^* h_0^2 \left(\pi \ln\left|\sin(\pi\tilde{a})\right| \bar{P}^{*2} - \pi \sin^2(\pi\tilde{a}) \bar{P}^* + (\frac{\pi}{4}) \sin^4(\pi\tilde{a}) - \frac{\Delta\gamma}{\lambda} \int_0^a \sqrt{1 + (2\pi\tilde{h}_o)^2 \sin^2(2\pi x/\lambda)}\, dx \right) - \frac{\pi^2}{2\lambda} \bar{P}^{*2} [y]_0^\infty \quad (1)$$

$$E_J = E^* h_0^2 \left(\pi \ln\left|\sin(\pi\tilde{a})\right| \bar{P}^{*2} - \pi \sin^2(\pi\tilde{a}) \bar{P}^* + (\frac{\pi}{4}) \sin^4(\pi\tilde{a}) - \frac{\Delta\gamma}{\lambda} a \right) - \frac{\pi^2}{2\lambda} \bar{P}^{*2} [y]_0^\infty \quad (2)$$

The equilibrium condition of the system is given by minimizing the total energy E_R and E_J. Then, the normalized external pressure of Johnson's approximation $\tilde{p}_J$ and the normalized external pressure of Rachmat's approximation $\tilde{p}_R$ are then obtained respectively as Eq. (3) & (4) [4].

$$\frac{\tilde{P}_R}{\tilde{h}_0} = \sin^2(\pi\tilde{a}) - \left(\frac{2\Delta\tilde{\gamma}}{(\pi\tilde{h}_0)^2}\tan(\pi\tilde{a})\right)^{1/2}\left(\sqrt{1+(2\pi\tilde{h}_o)^2\sin^2(2\pi\tilde{a})}\right)^{1/2} \quad (3)$$

$$\frac{\tilde{P}_J}{\tilde{h}_0} = \sin^2(\pi\tilde{a}) - \left(\frac{2\Delta\tilde{\gamma}}{(\pi\tilde{h}_0)^2}\tan(\pi\tilde{a})\right)^{1/2} \quad (4)$$

where,

$$\tilde{P}_R, \tilde{P}_J = \bar{p}/(E^*\pi\tilde{h}_0),\ \Delta\tilde{\gamma} = \Delta\gamma/(\lambda E^*),\ E^* = E/(1-\upsilon^2)$$
$$\tilde{a} = a/\lambda\ ,\ \tilde{h}_0 = h_0/\lambda \quad (5)$$

Area adhesion parameter Ψ is defined as Eq. (6).

$$\Psi = \frac{2\Delta\tilde{\gamma}}{(\pi\tilde{h}_0)^2} = \frac{2\Delta\gamma(1-\nu^2)}{\pi^2 h_0^2 E} \quad (6)$$

$\Delta\tilde{\gamma}$ is the normalized work of adhesion, E^* is the normalized elastic modulus, and $\tilde{h}_0$ is the normalized surface roughness.

3. Effect of Johnson approximation on adhesion contact between surface roughness of solid bodies

3.1 Effect of surface roughness on external pressure and equilibrium contact width

Equation (3) & (4) show relations of external pressure and equilibrium contact width, as plotted in Fig. 2 (a), (b) for Rachmat's and Johnson's approximation respectively, in case of $\tilde{h}_0 = 0.01$.

Figure 2 shows the adhesion Process from initial contact to perfect contact or separation. At initial contact, i.e. the two bodies are initially brought to contact without external pressure, the contact width increases from 0 to P_1, at which the energy is locally minimum. If we give a pressure between P_2 and P_3 in Fig.... 2, the contact width changes along the solid line. If we give a pressure larger than P_2, the contact will snap to the perfect contact. If we give a pressure less than P_3, the contact will be separated. Consequently, partial contact is realized between the solid lines P_2 and P_3.As shown in Fig.2 (a) and (b), the curve (P_2 - P_3) are similar to each other at $\tilde{h}_0 = 0.01$.

The relations between normalized total energy and equilibrium contact width for $\Psi = 0.1$ & $\tilde{h}_0 = 0.01$ are plotted in Fig. 3 (a), (b) for some external pressures. The total energy $\tilde{E}_R$ and $\tilde{E}_J$ are normalized as $\tilde{E}_R = E_R/E_T$, $\tilde{E}_J = E_J/E_T$ and $E_T = \lambda^2 E/(1-\upsilon^2)$.

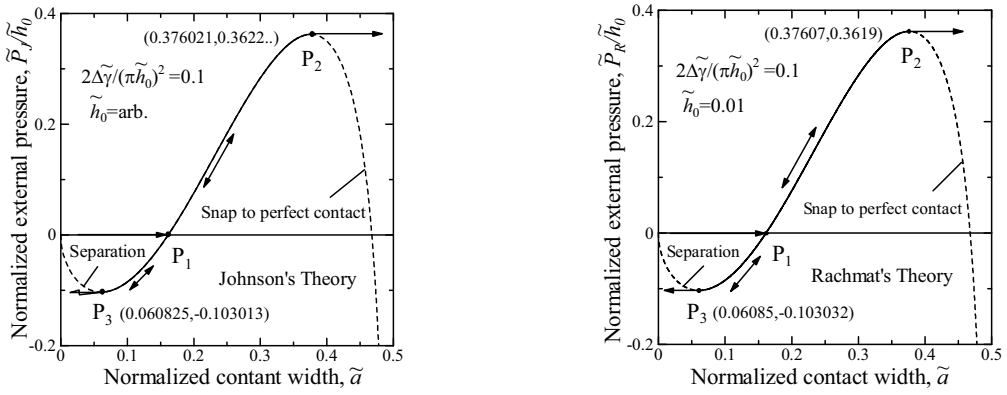

Fig.2. The adhesion Process from initial contact to perfect contact or separation for $\Psi = 0.1$. Plotted by Eq. (3) & (4) for an area adhesion parameter. (a) Johnson's approximation, (b) Rachmat's approximation

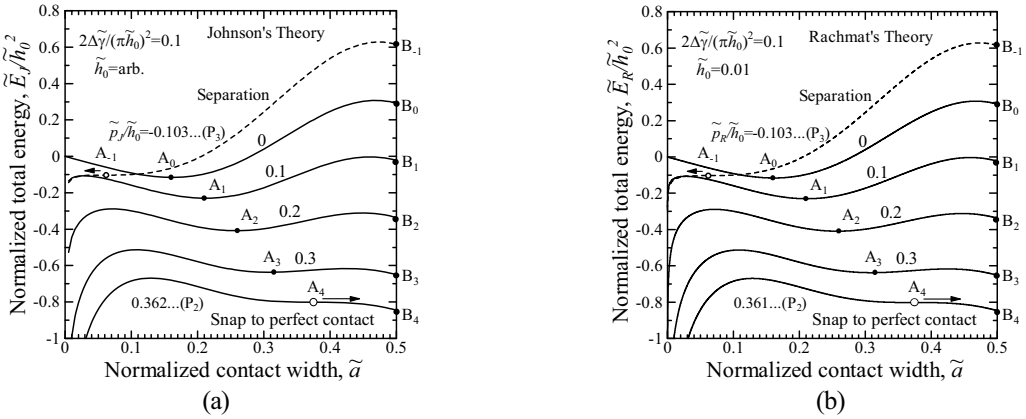

Fig.3. The relations of total energy and equilibrium contact width by varying external pressure with $\Psi = 0.1$ and $\tilde{h}_0 = 0.01$. (a) Johnson's approximation, (b) Rachmat's approximation.

3.2 Effect of surface roughness on area adhesion parameter and external pressure

The pressure of point P_2 and point P_3 in Fig. 2(a) (b) depends on Ψ. Fig. 4 plots the relation of normalized external pressure and equilibrium contact width by varying Ψ for (a) Johnson's approximation, (b) Rachmat's approximation at $\tilde{h}_0 = 0.01$ and (c) Rachmat's approximation at $\tilde{h}_0 = 0.05$. The solid lines in Fig. 4 are identical to the solid lines in Fig.2 (a) and (b) respectively.

With increasing the height of surface roughness, the range of partial contact decrease. Fig.5 plots the relation between the area adhesion parameter and the normalized external pressure at the critical points. At which the external pressure is maximum or minimum.

In Fig. 5, the dotted line shows Johnson's approximation and the solid line shows Rachmat's approximation. As the height of surface roughness is increased, the difference of Johnson's and Rachmat's approximations grow larger. Q_2 and Q_4 correspond to maximum and minimum for some parameters in Fig. 4 (a) respectively.

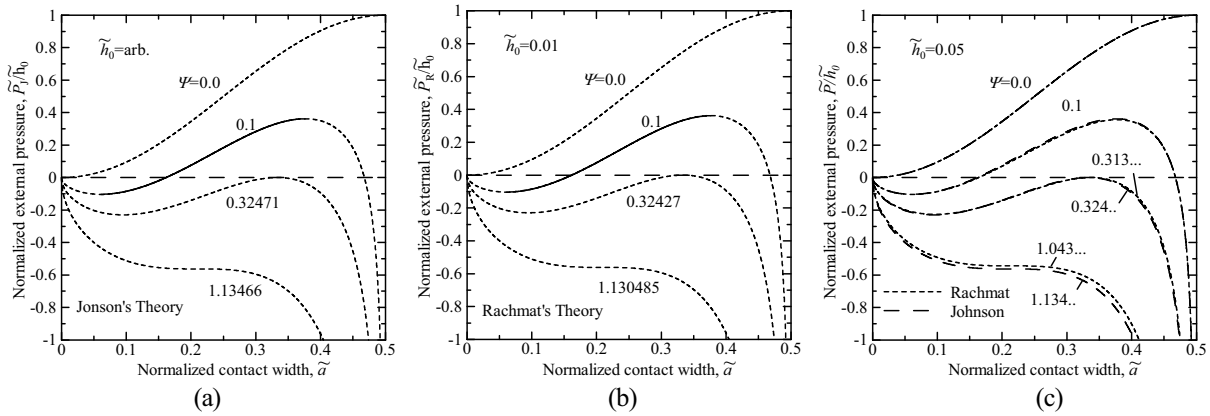

Fig.4. Plotted by Eq. (3) & (4) for specific area adhesion parameters. (a) Johnson's approximation, (b) Rachmat's approximation at $\tilde{h}_0 = 0.01$ and (c) Rachmat's approximation at $\tilde{h}_0 = 0.05$.

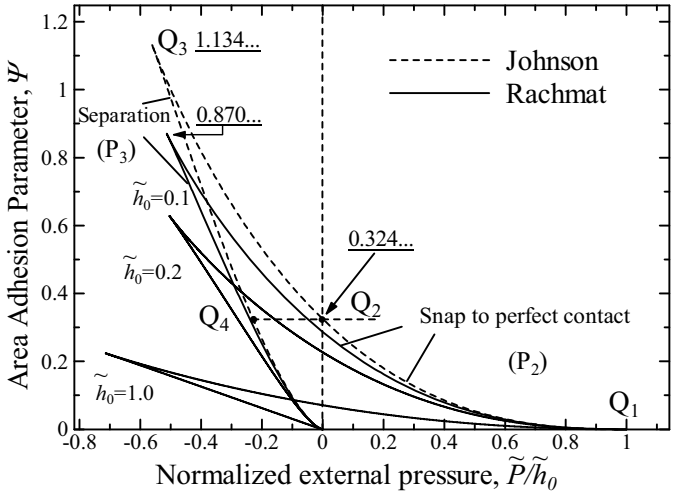

Fig.5. Relation between the area adhesion parameter and the normalized external pressure at critical points for Rachmat's & Johnson's theory.

3.3 Effect of surface roughness on separation stress

Figure 6 shows the relation between separation stress $\breve{\sigma}_{sep.}$ and the elastic constant $\breve{E}$, where

$$\breve{\sigma}_{sep.} = \sigma_{sep.} / (\Delta\gamma / \lambda) \tag{7}$$

$$\breve{E} = \left(\frac{E}{1-\nu^2}\right) \Big/ \left(\frac{\Delta\gamma}{\lambda}\right) \tag{8}$$

As shown in Fig. 6, both them are almost identical for $\tilde{h}_0 = 0.01$. And the differences between the both approximations grow larger as the height of surface roughness is increased.

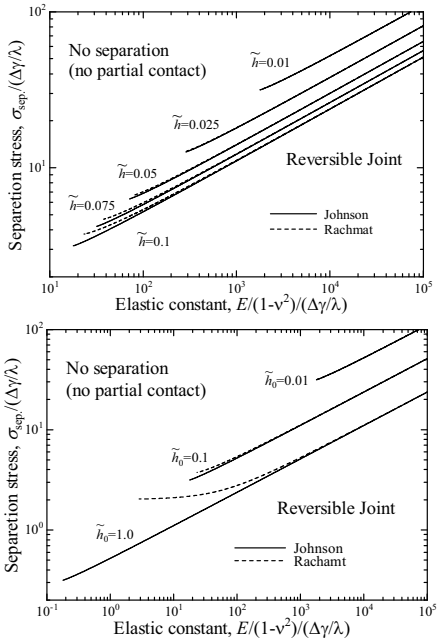

Fig.6. Relation between the elastic constant and the external pressure required to separate the interface, partially contacted for Johnson's and Rachmat's theory.

3.4 Applicability of Johnson approximation in area adhesion theory

From the results mentioned in the previous sections, the separation stress, surface roughness and adhesion parameter affect each other. In order to evaluate the applicability of Johnson approximation, we define the separation stress $\breve{\sigma}_R$ and $\breve{\sigma}_J$, the normalized contact width as $\tilde{a}_R$ and $\tilde{a}_J$ for Rachmat's and Johnson's approximations respectively. Then, the difference of normalized contact width and separation stress between Rachmat's and Johnson's approximation are defined as $(\breve{\sigma}_R - \breve{\sigma}_J)/\breve{\sigma}_J$ and $(\tilde{a}_R - \tilde{a}_J)/\tilde{a}_J$ respectively.

The relation between the difference of normalized contact width and the half height of surface roughness is shown in Fig. 7 (a), and the relation between the difference of separation stress and the half height of surface roughness is shown in Fig. 7 (b), for various value of area adhesion parameter.

The results shown in Fig. 7 are important since they are helpful for us to estimate the applicability of Johnson's and Rachmat's approximations.

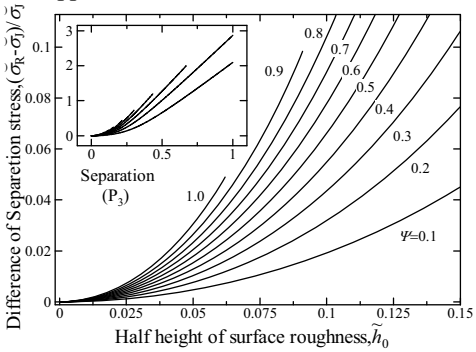

(a)

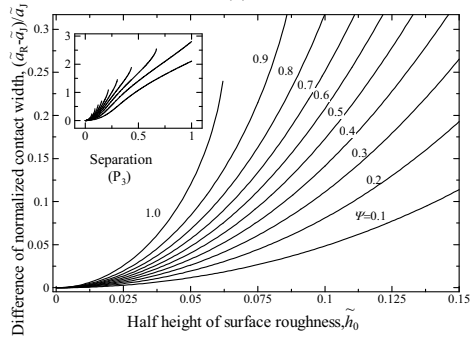

(b)

Fig.7. The relation between the half height of roughness and the difference of the separation stress and the difference of the normalized contact width by varying area adhesion parameter.

4. Conclusion

The applicability of Johnson approximation for area contact is studied by comparing Johnson's and Rachmat's theory. The difference of the contact width and the stress at the instance of separation in both theories.

Reference

[1] K.L.Johnson: The adhesion of two elastic bodies with slightly wavy surfaces, Int.J.Solids Structures, vol.32, (1995), pp.423-430

[2] R. R. A Sriwijaya, et. al., An analytical approach for the adhesion of a semi-infinite elastic body in contact with a sinusoidal rigid surface under zero external pressure, Journal of Adhesion Science and Technology, Vol. 21, No. 10, pp. 899-909, 2007

[3] 高橋 邦夫, ヘムタビー パソムポン, スリヴィジャヤ ラハマット, 雷 磊, ジャトミコ クスモ, 齋藤 滋規:弾性率変化による可逆接合の可能性, 溶接学会論文集, 第 26 巻, 4 号, p. 292–297, (2008)

[4] L.Lei: Effect of the surface roughness of a rigid body in contact with an elastic body upon the contact width, 溶接学会論文集, 第 27 巻, 2 号, (2009), pp. 196–199

A ROBUST IMAGE MATCHING METHOD TO LOCAL AFFINE TRANSFORM BY USING SCALE INVARIANT FEATURES

Student Number:08M18223 Name:Jiaping Li Supervisor: Yukihiko Yamasita

スケール不変特徴点を用いた画像の局所アフィン変換に頑健な対応点検索法

李 佳平

特徴点に基づくマッチング手法の利用と研究が，コンピュータビジョンの分野において急速に発展している．そこで本研究では Scale-Invariant Feature Transform(SIFT) を利用した局所アフィン変換に頑健な対応点検索法を提案する．

SIFT は，特徴点の検出とその点の特徴量の抽出を行う手法である．SIFT により検出される特徴点とその特徴量は，画像の回転・スケール変化に対して不変であるが，アフィン変換に対して不変ではない．本研究では，SIFT によって対応付けられた局所領域間のアフィン変換関係を利用し，対応点を再検索するアルゴリズムを提案する．そして，それを C 言語で実装し，その有効性を示す．

1 INTRODUCTION

Image matching is a fundamental technique in computer vision. It is used for object or scene recognition, 3D structure construction from multiple images, stereo correspondence, and motion tracking.

SIFT (Scale-Invariant Feature Transform)[1][2] is one of the best methods of image matching. SIFT extracts distinctive invariant features from images that can be used to perform reliable matching between different views of an object or a scene. The features are invariant to scaling and rotation, and are shown to enable robust matching up to a substantial range of affine distortion and change in 3D viewpoint. However, it is not fully affine invariant.

I propose a new search method, which is robust for local affine transformation to find corresponding points, even when images are transformed locally by affine transformations .

2 OVERVIEW OF SIFT

SIFT is a method to detect and extract local feature vectors that are reasonably invariant to changes in illumination, rotation, scaling, small changes in viewpoint, and noises in an image. We will explain the algorithm of SIFT.

2.1 Algorithm of SIFT

The process of SIFT consists of two stages, the detection of the key point and the generation of feature vector. Furthermore, they are divided into the following 4 steps. 1) Detection of key point candidates and their scale. 2) Selection and localization of the key points. 3) Calculation of their orientations. 4) Generation of their feature vectors. In 1), the key point candidates and their scales are detected by the DoG (Difference of Gaussian) process. In 2), from the candidates, the key points are chosen by their main curvature. Next, the sub-pixel-position is specified for each key point. In 3), the histogram is generated from gradient information on the key point. Its orientation is calculated from the histogram. The invariance to rotation is obtained by this operation. In 4), the area for describing features is rotated in the direction of the orientation determined previously. Afterwards, the feature vector is calculated by using gradients within the rotated area. The gradient at a point in the feature area is calculated and is quantized into 8 directions. The area is separated in 16 blocks and the histogram of the gradients is calculated in each block. Finally, the feature vector is normalized. The invariance of a feature vector for lighting and shading comes from this normalization.

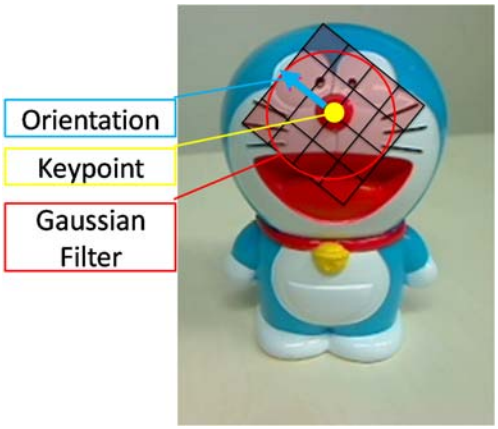

Figure 1: Orientation

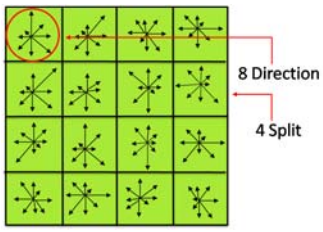

Figure 2: Feature vector

2.2 Matching

The matching is done by comparing the feature vectors. The pair of feature vectors of which distance is the smallest is extracted as matched points. The distance is evaluated by the following expressions.

$$d(v^{k_{I_1}}, v^{k_{I_2}}) = \sqrt{\sum_{i=1}^{128} (v_i^{k_{I_1}} - v_i^{k_{I_2}})^2} \tag{1}$$

To reduce the error rate, only the nearest point that satisfies the condition

$$d_1 < w d_2 \tag{2}$$

d_1 :The distance to the nearest point
d_2 :The distance to the second nearest point
w :Threshold
is extracted as a matched point.

3 Homogeneous coordinates

The homogeneous coordinates of (x,y) is usually written as (ξ_1,ξ_2,ξ_3) which satisfies:

$$x = \frac{\xi_1}{\xi_3}, y = \frac{\xi_2}{\xi_3}, \tag{3}$$

where at least one of ξ_1, ξ_2, ξ_3 is not 0.

Two tuples of homogeneous coordinates such as (ξ_1,ξ_2,ξ_3) and $(\lambda\xi_1,\lambda\xi_2,\lambda\xi_3)$ express the same point for any non-zero scalar λ.

4 Affine transform

An affine transformation in Euclidean space is one that preserves the collinearity relation between points (figure 3). It consists of linear transformations (rotation, scaling or shear) and a translation (shift). An affine transformation can be represented by a matrix using homogeneous coordinates.

$$\begin{pmatrix} 1 & 0 & t_x \\ 0 & 1 & t_y \\ 0 & 0 & 1 \end{pmatrix} \begin{pmatrix} a & b & 0 \\ c & d & 0 \\ 0 & 0 & 1 \end{pmatrix} = \begin{pmatrix} a & b & t_x \\ c & d & t_y \\ 0 & 0 & 1 \end{pmatrix} \tag{4}$$

The affine transformation matrix between the corresponding areas can be calculated by the three pairs of corresponding points as follows.

$$\begin{pmatrix} x'_1 & x'_2 & x'_3 \\ y'_1 & y'_2 & y'_3 \\ 1 & 1 & 1 \end{pmatrix} = \begin{pmatrix} a & b & t_x \\ c & d & t_y \\ 0 & 0 & 1 \end{pmatrix} \begin{pmatrix} x_1 & x_2 & x_3 \\ y_1 & y_2 & y_3 \\ 1 & 1 & 1 \end{pmatrix}. \tag{5}$$

Then, we have

$$\begin{pmatrix} a & b & t_x \\ c & d & t_y \\ 0 & 0 & 1 \end{pmatrix} = \begin{pmatrix} x'_1 & x'_2 & x'_3 \\ y'_1 & y'_2 & y'_3 \\ 1 & 1 & 1 \end{pmatrix} \begin{pmatrix} x_1 & x_2 & x_3 \\ y_1 & y_2 & y_3 \\ 1 & 1 & 1 \end{pmatrix}^{-1} \tag{6}$$

In general, the postural change of an object and the change of 3D viewpoint can be approximated by a local affine transformation.

Figure 3: Affine transformation

5 Proposed method

The affine transformation causes the distortion of the histogram in the feature vector.

The proposed method detects the affine transform matrix between the local areas in two images by using SIFT corresponding points. The local area is transformed inversely by the affine transform matrix to reduce the effect of the affine transformation. Then, the orientations and feature vectors of key points in the local area are rebuild. By using the new feature vectors, the corresponding points are searched.

5.1 Neighborhood detection

At least three corresponding points are necessary to calculate the affine transformation matrix between the local areas. I explain the neighborhood detection to search the corresponding points. At first, the algorithm detects the corresponding points in the neighborhood of the feature points which could not find it's corresponding point at the first matching. The number of detected corresponding points is be determined by a threshold to stop the detection. The result depends on this threshold.

Figure 4 shows two images to be matched. Figure 5 shows the corresponding points between the two images by the first matching. Figure 6 shows a result of search of corresponding points in this neighborhood. In Figure 5, we set the threshold 5.

Figure 4: Input image

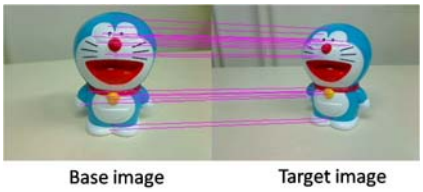

Figure 5: Corresponding points

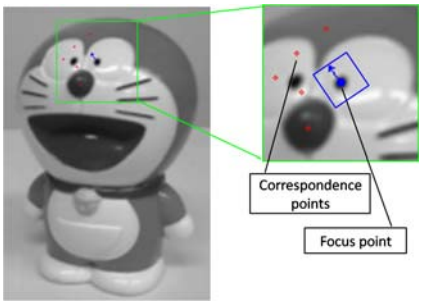

Figure 6: Search for corresponding points in the neighborhood

5.2 Affine transformation and feature rebuild

After the local affine transformations, the orientation and feature vector were recalculated. Figure 7 shows the result of the local affine transformation. The orientation and feature vector become similar to those of the base image.

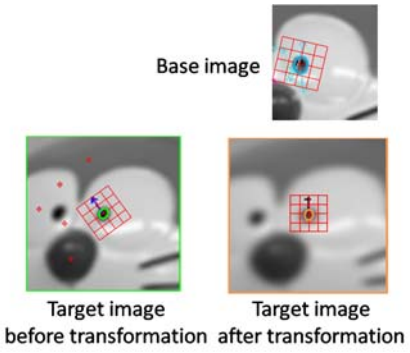

Figure 7: Affine transform

5.3 Algorithm

I make a program to evaluate the proposed method. It's process is as follows.

step1 : Obtain two sets of the feature points by the SIFT process.

step2 : Obtain the set of corresponding points (C1) between two images by matching process.

step3 : Obtain two sets of the feature points (F1,F2) whose points could not be matched at step2. Obtain more than 3 corresponding points in the neighborhood of the point in F2 by the neighborhood detection. Obtain the affine transform matrices calculated by all combinations of corresponding points. Obtain the new set of the feature points (F3) of the local area transformed inversely by the transform matrix.

step4 : Obtain the new corresponding points (C2) by matching from F1 and F3.

Figure.8 shows the flow chart of the program for the experiment.

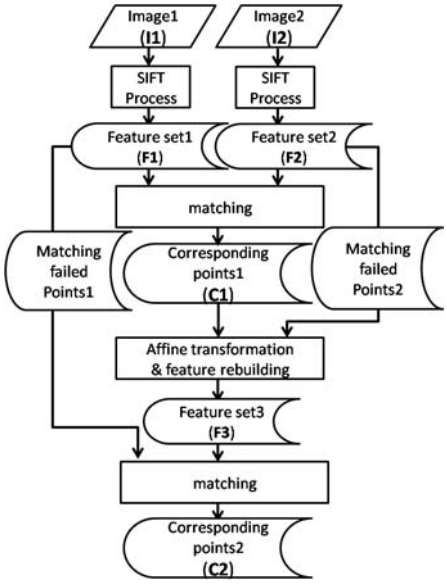

Figure 8: Flowchart of the proposed algorithm

6 Experiment

I applied the proposed method to several types of different camera viewpoint image sets such as planar objects, 3D objects, constructions. The number of matching points, run time and the number of incorrect matching are compared to those by the original SIFT. Several different thresholds of neighborhood detection are examined. The specs of computer

for experiment is shown in Table 1.

CPU：	Genuine Intel(R) CPU T2300 @1.66GHz
メモリ：	2G

Table 1: Experiment environment

6.1 Result of experiment

As an example of nice results, the result of the input image Figure 5 is show in Figure 9 and Table 2 with the thresholds for neighborhood detection. The pink lines show the corresponding points obtained at step 2. And the blue lines show the new corresponding points obtained at last. The number in the bracket in Table 2 shows the number of incorrect matching. We can increase correct corresponding points by the proposed algorithm.

threshold	corresponding points
3	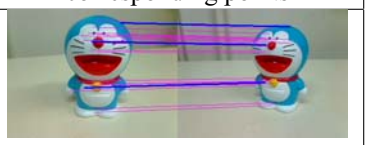
4	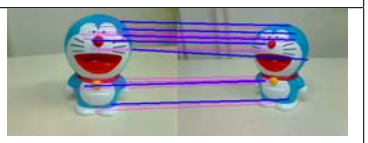
5	

Figure 9: Experiment result 1

threshold	w=0.6
SIFT	matching：18(0) run time：0.56s
3	matching：21(0) run time：1.17s
4	matching：25(0) run time：3.29s
5	matching：27(0) run time：6.94s

Table 2: Experiment result 1

A bad result because of the similarity of the local areas is shown in Figure 10 and Table 3.

6.2 Discussions

From the result, we know the run time will increase significantly according to the increase of threshold

threshold	corresponding points
SIFT	
3	
4	
5	

Figure 10: Experiment result 2

threshold	w=0.6
SIFT	matching：11(4) run time：1.92s
3	matching：11(4) run time：7.09s
4	matching：12(5) run time：15.87s
5	matching：13(6) run time：30.14s

Table 3: Experiment result 2

and the number of feature points. Some incorrect corresponding points are obtained because of the incorrect estimation of the affine transformation matrix.

7 Conclusions

I proposed a new search method to find the corresponding points that are robust for the local affine transformation by using SIFT algorithm. I showed its advantage by experiments where the number of correct corresponding points was increased.

For future tasks, we have to improve the algorithm to reduce the incorrect matching and the run time.

REFERENCES

[1] D. G. Lowe:*Object recognition from local scale-invariant features*, IEEE International Conference on Computer Vision (ICCV), pp.1150-1157(1999)

[2] Hironibu Fujiyoshi:*Extract feature vector by gradient base -SIFT and HOG-* , PRMU, pp.511-517(2007)

Geolocation of Emergency Network Radios in a Post Disaster Area

Student Number: 08M18230 Name: Mutsawashe GAHADZA Supervisor: Jun-ichi TAKADA

被災地での狭帯域緊急無線通信ネットワークによる地理位置情報に関する研究

ガハザ　ムツァワシェ

本研究では, 被災地において適用可能な防災無線端末の位置特定手法について検討を行った。TDOA（電波の到来時間差）及び AOA（電波の到来角）という二つの手法を用いて、シミュレーションを行った。その結果、GNU Radio-USRP というソフトウェア無線プラットフォームを利用した実装の観点から、干渉計の原理に基づいた AOA 手法の方が相応しいことが確認された。

1 Introduction

Geolocation of radio signal emitters is an old problem that has received a lot of attention from many researchers. [1] gives detailed overviews of localization techniques from a signal processing point of view. [2] concentrates on positioning algorithms. Indeed many methods to solve the geolocation problem exist in literature and practical applications are plenty in different scenarios. The choice of an appropriate method is a function of many factors which include implementation cost, and the type of radio signals to be localized. This work assumes that a natural disaster has occurred in a major city [8]. As a result many emergency network teams converge to try and carry out rescue operations. Unfortunately they begin to interfere with one another after setting up their radio communications networks. The task at hand is to design a wireless sensor network (WSN) that is capable of pinpointing the position of all radio signals within the area to an appropriate degree of precision. In oder to come up with a suitable solution, a number of assumptions based on a realistic scenario have to be borne in mind. As in any implementation centered solution, evaluation of all possible solutions in an analysis whose scope is the system as a whole is imperative. This thesis focuses on two geolocaton methods, namely the time difference of arrival (TDOA) method and the angle of arrival (AOA) method with a view to be able to select the most suitable geolocation method for a post disaster scenario.

2 The Problem Statement and Objectives

The diagram in Fig.1 shows the WSN that is supposed to determine the geographical coordinates of each of the emergency network radios within the scene. Before proceeding further it is necessary to come up with the assumed conditions for the disaster scenario as well as other factors to do with geolocation solution being sought.

- A preliminary survey done revealed the transmission frequency for emergency radios in Japan in the 100 MHz to 1 GHz range. Therefore this transmission frequency range shall be adopted for the purposes of this work.

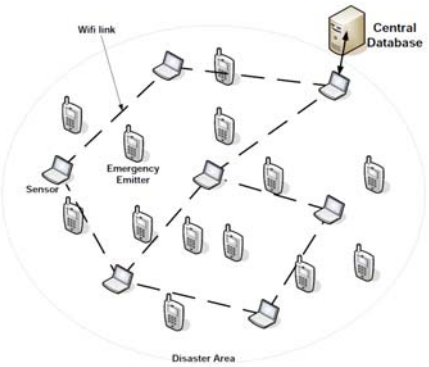

Figure 1: Disaster Struck Area

- The emergency radio signals are narrowband.
- The WSN to be designed for geolocation purposes shall have no communication with the emergency network emitters.
- The GNU Radio-USRP[9] software defined radio platform is the targeted implementation platform for the geolocation solution.
- The sensors shall be about 100m apart.

2.1 The Problem

Given the typical disaster scenario, with the GNU Radio-USRP software defined radio platform, what geolocation method would be most suitable to implement in order to get reasonable localization accuracy?

2.2 Objectives

The objectives of this work are as follows :

- To evaluate the suitability of the Time Difference of Arrival (TDOA) based geolocation method for implementation in a typical post disaster scenario.
- To evaluate the suitability of the phase interferometry based Angle of Arrival (AOA) measurement geolocation method for implementation in a typical post disaster scenario.

3 Localization Methods

One way of obtaining the location of a mobile station is what is known as mobile based localization. In this method the mobile station measures a given signal parameter from multiple transmitters and estimates its own postion. A good example is the global positioning system (GPS). A GPS receiver receives signals from four satellites with information about the satellite position and time at which the signal was transmitted. Knowing the time of arrival of the received signal, the receiver is able to calculate the time difference of arrival of the signals from the satellites. However for the purposes of this work, a geolocation method like the GPS can not be used. This is because the radio signal emitters to be localized are assumed to have no GPS receivers. This work seeks to passively locate these emitters. An opposite way of doing things is to let sensors in a network do measure the relevant signal parameters and then use these measurements to localize the emitter. This second method is called network based localization. For purposes of this work, network based localization is focused on as it is the one suitable for the scenario under consideration.

Several localization methods do exist. The received signal strength (RSS) method determines the distance of the emitter from the sensor by measuring the signal strength of the received signal. The accuracy of this method is severely reduced by fading fluctuations in a multipath environment and the uknown body effect to the transmitted power and the signal's directivity. It is also necessary to know the transmitted power and the pathloss model in order to estimate the distance traveled by the signal. For these reasons, and since no knowledge of the transmitted power is assumed in the scenario under consideration, the RSS method could not be adopted for geolocation. Another method is called the time of arrival (TOA) method in which the time the signal travels from the emitter to the sensor is used to estimate how far away it is from the sensor. For this method it is necessary to know the emitter timing. For this reason this method can not be employed for the disaster scenario being considered. Two methods that can potentially be used are known as the time difference of arrival (TDOA) and angle of arrival (AOA) methods.

4 TDOA geolocation method

One potential method that could be used is called the time difference of arrival (TDOA) method. In this method, the time difference of the arrival times at each pair of sensors is measured and the time differences are translated into range differences. Hyperbolic equations that describe these range differences and whose solution localizes the emitter are the determined. Fig.2 shows the loci of the hyperbolic functions and their intersection at the emitter. This method has the advantage over the TOA method since it does not require time synchronization with the emitter. However synchronization with among sensors is still necessary.

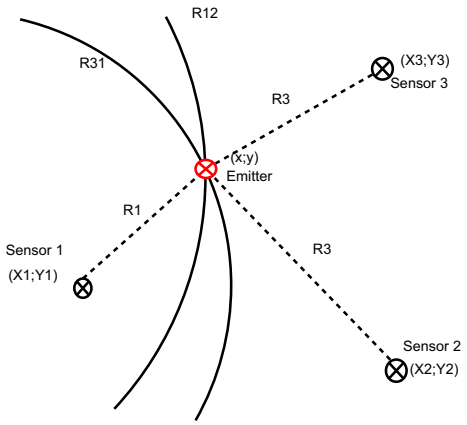

Figure 2: TDOA basic principles

Table 1: Geolocation Parameters TDOA Simulations

TDOA Estimation	- GCC (Weighting function=1) [3, 4] -SPECCOA (Cyclostationary) [3, 4]
SCD Estimation Algorithm	FAM (fft Accumulation Method)[6]
Positioning	Chan's Method [5]
Number of sensors	3
Sensor Coordinates	(0;0),(-1000;0),(1500;1500) m
Emitter coordinates	(500;500) m

4.1 TDOA Measurement

Measurement of the tdoas at the sensors can be done using two different classes of methods. One class of methods is called the generalized cross correlation (GCC) methods while the other is called cyclostationary methods [3, 4]. The advantage of the cyclostationary methods is that it becomes possible to seperate signals which might be transmitting at the same frequencies if they have different hidden periodicities within them. However the signal processing requirements are relatively more demanding.

4.2 TDOA Positioning

Positioning involves approaximating the solution to the non-linear equations obtained. Of the several methods in the literature, Chan's method [5] was found to be the most suitable in the scenario under consideration. It gives an explicit and non-iterative solution.

4.3 TDOA geolocation error simulation

Fig.3 shows the simulated error for an additive white gausian noise channel. The adopted simulation parameters are as in Table 1. In this simultation the sychronization error was neglected for both the gcc and cyclostationary tdoa measurement. Its aim was only to investigate the error due to tdoa estimation if we assume a given signal to noise ratio. The geolocation positioning error, ϵ_{rTDOA}, is given by the root mean square error value as in Eq.1

$$\epsilon_{rTDOA} = \sqrt{\frac{1}{N}\sum_{n=1}^{N}((\hat{x}_n - x_0)^2 + (\hat{y}_n - y_0)^2)} \quad (1)$$

where $(\hat{x}_n, \hat{y}_n)$ are the estimated (x, y) coordinates while (x_0, y_0) are the true values of the (x, y) coordinates.

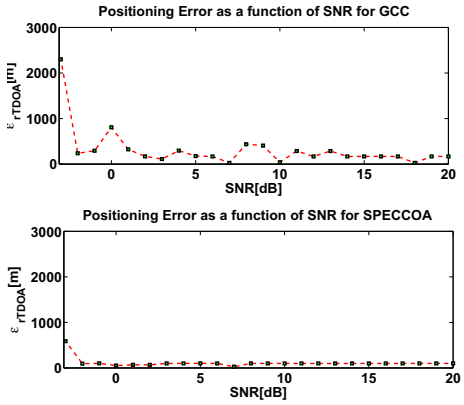

Figure 3: TDOA geolocation error

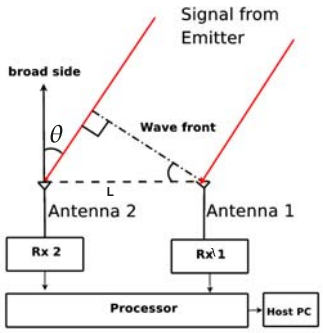

Figure 4: Interferometry basic principles

4.4 Synchronization of Sensors

Synchronization based on the Precision Time Protocol (PTP) IEEE1588 standard could be implemented as it is fairly cheap to do so. Use of software generated time stamps, as could be done in the GNU Radio software, implies a synchronization error of about 2.8μs [7]. Assuming the speed of light for the electromagnetic wave, this would imply an error of about 840m due to synchronization alone. Use of GPS synchronization for all the sensor nodes would also be too expensive for a WSN. Therefore TDOA geolocation method could not be implemented in this scenario.

5 AOA geolocaton method

In this method the angle of arrival of the signal at multiple sensors is estimated using phase interferometry. [10] discusses how to model the propagation environment for MIMO performance evaluation.

5.1 Geolocation based on AOA measurement using Phase Interferometry

In Fig.4 the phase difference of the signals at the two antennas is given by:

$$\phi = \frac{2\pi L \sin(\theta)}{\lambda} \tag{2}$$

where λ is the wavelength of the signal, L is the antenna separation distance and θ is the AOA to be determined.

Table 2: Simulation Parameters for AOA

Number of sensors	3
Sensor positions	(-100;0),(50,-50$\sqrt{3}$) (50;50$\sqrt{3}$)
Emitter position	(0;0)
Antenna elements per sensor	2
Fading Model	Clarke's Model for Reighlay fading with limited power spectrum
Antenna element Seperation	$\lambda/2$
Number of signals	64
Angular spreads	0, 3, 6, 9, 12
Number snapshots	1000
Number of trials	100 000

To avoid ambiguity in the measured phase set $L < \frac{\lambda}{2}$. This phase difference can be estimated by the cross correlation of the two signals at the two antenna elements as in Eq.3. The phase of the resultant cross correlated product is the phase difference between the two signals.

$$\phi = \text{angle}\frac{1}{T}\int_0^T \{x_1(t)x_2^*(t)dt\} \tag{3}$$

$x_1(t)$ and $x_2(t)$ are the two signals while * denotes the complex conjugate of the signal.

5.2 AOA Positioning

A simple positioning algorithm that takes the mean of the positions determined from measurements from all relevant pairs of sensors has been applied to this work.

5.3 Simulation of Phase interferometry based AOA Estimation Geolocation method

This simulation was done in order to investigate the effect of angular spread due to multipath on the accuracy of the AOA measurement, and hence the accuracy of the geolocation solution for the post disaster scenario given the capabilities of the target implementation hardware which is the GNU Radio - USRP [9] software radio platform. The simulation parameters are shown in table 2.

It is is important to know the effect of noise and angular spread of the signal in the multipath environment. The fading model assumes 64 signals which are subjected to Rayleigh fading with limited uniformly distributed angular spread. It is assumed that there is no direct line of sight between the sensors and the emitter, except for zero degree angular spread. The model assumes three sensors placed at sufficient height such that there are no scatterers around the sensors but there are plenty of scatterers around the emitter. For 1000 snapshots, 100 000 trials were repeatedly done averaged.

Fig.5 shows the geometrical model employed. Three USRP[9] sensors were placed equidistant from each other, at the circumference of a circle of radius 100m, with the emitter placed at the center of the circle. Each of the sensors has two omnidirectional antenna elements whose endfire direction is tangential to the circle at a given point. The AOA at a given sensor is

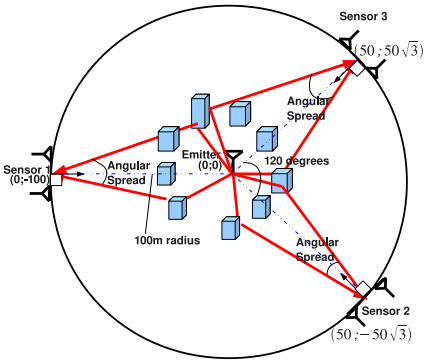

Figure 5: The assumed geometrical configuration of a three sensor network

taken as the angle between the direction of arrival of the signal and the broad side direction of the sensor. This means the AOA at each sensor must ideally be zero.

5.4 Results

Fig.6 and Fig.7 show the variation of the observed angle estimation error and the corresponding position estimation error as functions of the average signal to noise ratio and SNR. At high signal to noise ratio the error is dominated by the effect of angular spread. The AOA error is the standard deviation of the error, given by

$$\epsilon_\theta = \sqrt{\frac{1}{N}\sum_{n=1}^{N}(\hat{\theta}_n - \theta_0)^2} \qquad (4)$$

where $\hat{\theta}_n$ is the estimated AOA and θ_0 is the true value of the AOA. N is the number trials used. Similarly the positioning error, ϵ_r, is given by the root mean square error value as in Eq.5

$$\epsilon_r = \sqrt{\frac{1}{N}\sum_{n=1}^{N}((\hat{x}_n - x_0)^2 + (\hat{y}_n - y_0)^2)} \qquad (5)$$

where the symbols have the same meaning as in section 4.3. For the 100m radius considered the error caused by fading for the angular spreads simulated is less that 10m at relatively high SNR values. The high SNR values may be safely assumed for emergency radios since they have to communicate over relatively long distances.

6 Conclusions

An evaluation of the suitability of several geolocation methods in a post disaster area was conducted. Focus was put on TDOA and AOA with a view to implement them on the GNU Radio - USRP software defined radio platform. It was found out that TDOA could not be cost effectively be employed. Phase interferometry based AOA geolocation was investigated. The effect of angular spread and SNR on the error performance of the AOA measurement and the resultant geolocation error was investigated through simulation.

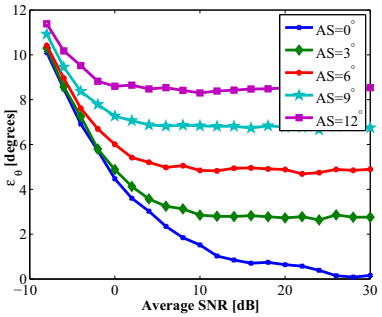

Figure 6: AOA error

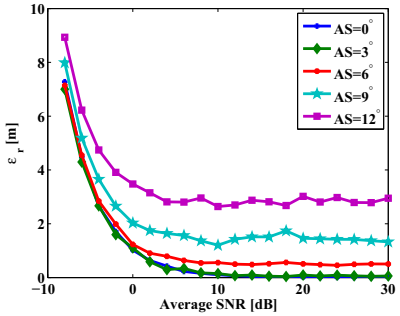

Figure 7: AOA geolocation based position error

References

[1] N. Patwari, J. Ash, S. Kyperountas, I. Hero, A.O., R. Moses, and N. Correal, "Locating the nodes: cooperative localization in wireless sensor networks," *Signal Processing Magazine, IEEE*, vol. 22, no. 4, pp. 54 – 69, july 2005.

[2] G. Mao, B. Fidan, and B. D. Anderson, "Wireless sensor network localization techniques," *Computer Networks*, vol. 51, no. 10, pp. 2529 – 2553, 2007.

[3] W. Gardner and C.-K. Chen, "Signal-selective time-difference-of-arrival estimation for passive location of man-made signal sources in highly corruptive environments. i. theory and method," *Signal Processing, IEEE Transactions on*, vol. 40, no. 5, pp. 1168 –1184, may 1992.

[4] C. K. Chen and W. Gardner, "Signal-selective time-difference of arrival estimation for passive location of man-made signal sources in highly corruptive environments. ii. algorithms and performance," *Signal Processing, IEEE Transactions on*, vol. 40, no. 5, pp. 1185 –1197, may 1992.

[5] Y. Chan and K. Ho, "A simple and efficient estimator for hyperbolic location," *Signal Processing, IEEE Transactions on*, vol. 42, no. 8, pp. 1905 –1915, aug 1994.

[6] R. Roberts, W. Brown, and J. Loomis, H.H., "Computationally efficient algorithms for cyclic spectral analysis," *Signal Processing Magazine, IEEE*, vol. 8, no. 2, pp. 38 –49, apr 1991.

[7] J. Kannisto, T. Vanhatupa, M. Hannikainen, and T. Hamalainen, "Software and hardware prototypes of the ieee 1588 precision time protocol on wireless lan," *Local and Metropolitan Area Networks. The 14th IEEE Workshop*, sept 2005.

[8] B. Fette and L. Puker, "'09 Challenge", [Online]. Available http://www.radiochallenge.org/09SampleProblem.html, [Accessed on 12 Feb. 2010].

[9] M. Ettus and J. Corgan, "Welcome to GNU Radio!", [Online]. Available http://gnuradio.org/redmine/wiki/gnuradio, [Accessed on 19 Feb. 2010].

[10] J. Takada, "Propagation Modeling for Performance Evaluation of MIMO Antennas," *Microwave Workshop and Exhibitions (MWE 2007), WS8-1*, nov 2007.